Multi-Parametric Quantification of White Matter Microstructure in the Human Brain

Multi-Parametric Quantification of White Matter Microstructure in the Human Brain

By

Sonya Bells, Ph.D.

A Thesis

Submitted to the School of Graduate Studies

in Partial Fulfilment of the Requirements

for the Degree

Doctor of Philosophy

Cardiff University

DOCTOR OF PHILOSOPHY (2012) Cardiff University

(Psychology) Cardiff, Wales

TITLE: Multi-Parametric Quantification of White Matter Microstructure in the Human Brain

AUTHOR: Sonya Bells, Ph.D.

SUPERVISORS: Prof Derek K. Jones, Dr. Mara Cercignani

NUMBER OF PAGES: xvi, 204

Declaration Form

The following declaration is required when submitting your PhD thesis under the University's regulations.

Declaration

This work has not previously been accepted in substance for any degree and is not concurrently submitted in candidature for any degree.

....

Candidate Date

Statement 1

This thesis is being submitted in partial fulfillment of the requirements for the degree of PhD.

....

Candidate Date

Statement 2

This thesis is the result of my own independent work/investigation, except where otherwise stated. Other sources are acknowledged by explicit references.

....

Candidate Date

Statement 3

I hereby give consent for my thesis, if accepted, to be available for photocopying and for inter-library loan, and for the title and summary to be made available to outside organisations.

....

Candidate Date

Statement 4: Previously approved bar on access

I hereby give consent for my thesis, if accepted, to be available for photocopying and for inter-library loans after expiry of a bar on access previously approved by the Graduate Development Committee.

....

Candidate Date

Acknowledgements

Many people deserve acknowledgement for their contributions to the work presented in this thesis.

I wish to express gratitude to my supervisor, Derek Jones. Derek's expertise has contributed to many aspects throughout this work. I would also like to thank second supervisor Mara Cercignani for her insight and expertise in qMT that helped me along the way. Furthermore, I wish to thank the School of Psychology for their financial support.

This project would not have been possible without the support of many people. Especially I want to thank Luke Dustan who was involved in acquiring the behavioural tasks used in Chapter 6 (Reproducibility in Tract-based Statistics). Furthermore, I would like to thank John Evans with helping with acquiring some of the MRI data and Spiro Stathakis with his technical assistance throughout my thesis and time at CUBRIC.

Special recognition must be given to my friends that have helped me along the way and with whom I have had many inspiring discussions on the interpretation of this study and other MR issues. Most of all I would like to thank my family. It is their gift of encouragement, guidance and humour that I will cherish in my continued pursuit of all career and life goals. There are still many I could thank in this space. The people I have met during this process have all added pieces to this project, however small. Their contributions are all worthy of recognition and respect, and I acknowledge them all. Thank you.

Table of Contents

List of Figures

List of Tables

List of Abbreviations

Abbreviation	Description
ADC	Apparent Diffusion Coefficient
CC	Cross-correlation
Ci	Confidence Interval
CSF	Cerebral Spinal Fluid
CSD	Constrained Spherical Deconvolution
CHARMED	Combined Hindered and Restricted Water Diffusion
CRT	Choice Reaction Time
CST	Cortico-spinal Tract
CWPE	Continuous Wave Pulse Equivalent
DAM	Double Angle Method
DTI	Diffusion tensor imaging
DWI	Diffusion weighted imaging
EPI	Echo planar imaging
FOD	Fibre Orientation Distribution
FA	Fractional Anisotropy
FID	Free Induction Decay
fMRI	Functional Magnetic Resonance Imaging
FOV	Field of View (cm^2)
FSE	Fast Spin Echo
FWHM	Full width half max
IR	Inversion Recovery
IQ	Intelligence Quotient
mcDESPOT	Multi-Component Driven Equilibrium Single Pulse Observation of T_1 and T_2
MD	Mean Diffusivity
MEG	Megnetoencephalogrphy
MMPF	Macromolecular Proton Fraction

MR	Mental Rotation
MT	Magnetisation transfer
MTR	Magnetisation transfer ratio
MPG	Motion Probing Gradient
MRI	Magnetic resonance imaging
MWF	Myelin Water Fraction
NEX	Number of Excitations
PDF	Probability Density Function
PFG	Pulsed Field Gradient
RF	Radiofrequency
RD	Radial Diffusivity
ROI	Region of Interest
sCC	Splenium of the Corpus Callosum
SNR	Signal to noise ratio
SPGR	Spoiled Gradient Echo
bSSFP	Balanced-Steady-State Free Precession
TBSS	Tract-based Statistics
TFCE	Threshold-Free Cluster Enhancement
UNC	Uncinate Fasciculus
VBA	Voxel-Based Analysis
WM	White Matter

List of Symbols

Symbol	Description	Units
α	RF excitation flip angle	degrees
Δ	Offset Frequency	Hz
ω_0	Larmor frequency	Hz
λ	Eigenvalue	–
ϕ	Magnetization phase	radians
γ	Gyromagnetic ratio (46.6 MHz/T for ^1H)	MHz/T
θ_{SAT}	Saturation Pulse	
B_0	Main magnetic field strength	T
K^{trans}	Volume transfer constant	–
M_{xy}	Transverse magnetization (perpendicular to B_0)	–
M_z	Longitudinal magnetization (parallel to B_0)	–
M_0	Equilibrium longitudinal magnetization	–
M_{dir}	Direct Effect	–
R_1	Relaxation rate (=$1/T_1$)	ms^{-1}
R	Magnetisation exchange between two pools	–
T	Tesla (=10,000 gauss)	–
TE	Time from the excitation pulse to the center of the echo signal	ms
TR	RF excitation repetition time	ms
T_1	Spin-lattice relaxation time	ms
T_2	Spin-spin relaxation time	ms
T_2^*	Effective spin-spin relaxation time (from field inhomogeneities)	ms

Summary

To date the majority of MRI studies of white matter (WM) microstructure have used diffusion tensor MRI (DT-MRI), comparing groups on a voxel-by-voxel basis. There are limitations to this approach. Firstly, the analysis approach treats each voxel independently, ignoring the fact that adjacent voxels may come from the same tract (or may come from completely separate tracts). Secondly, DT-MRI is sensitive to both interesting properties of WM (e.g., myelination, axon density), and less interesting properties (e.g., intra-voxel orientational dispersion). In contrast, other imaging approaches, based on different contrast mechanisms, can provide increased specificity and therefore sensitivity to differences in one particular attribute of tissue microstructure (e.g., myelin content or axonal density). Both quantitative magnetization transfer (qMT) imaging and multicomponent relaxometry provide proxy estimates of myelin content while the combined hindered and restricted model of diffusion (CHARMED) provides a proxy estimate of axon density.

We present a novel imaging method called *tractometry*, which permits simultaneous quantitative assessment of these different microstructural attributes along specific pathways. Crucially, the metrics were only weakly correlated, suggesting that *tractometry* provides *complementary* WM microstructural information to DT-MRI. In developing the *tractometry* pipeline, we also performed a detailed examination of the qMT pipeline, identifying and reducing sources of variance to provide optimized results.

We also identify a number of issues with the current state-of-the art, including the stability of *tract based spatial statistics* (TBSS). We show that conducting a structure-function correlation TBSS study may lead to vastly different conclusions, based simply on the participants recruited into the study. We also address microstructural asymmetry, including the degree of partial-volume effects (PVEs) from free water, which impact on WM metrics. The observed spatial heterogeneity of PVEs can potentially confound interpretation in studies where contralateral hemispheres are used as internal controls, and could either exacerbate or possibly negate tissue differences.

Chapter 1

Introduction

Most of us do not think about how powerful or complex our brains really are. Not until the Renaissance when Andreas Vesalius dissected the human brain it was considered a vital organ, whereby he gives a detailed description of its complexity and its possible mechanical function (Catani and Thiebaut de Schotten 2012). This idea propelled brain research to what it is today.

The brain is composed of two distinct tissue types: white and grey matter. White matter constitutes the physical "wiring" of the brain and connects the grey matter. A schematic of depicting a myelinated axon is shown in Figure 1.1. White matter

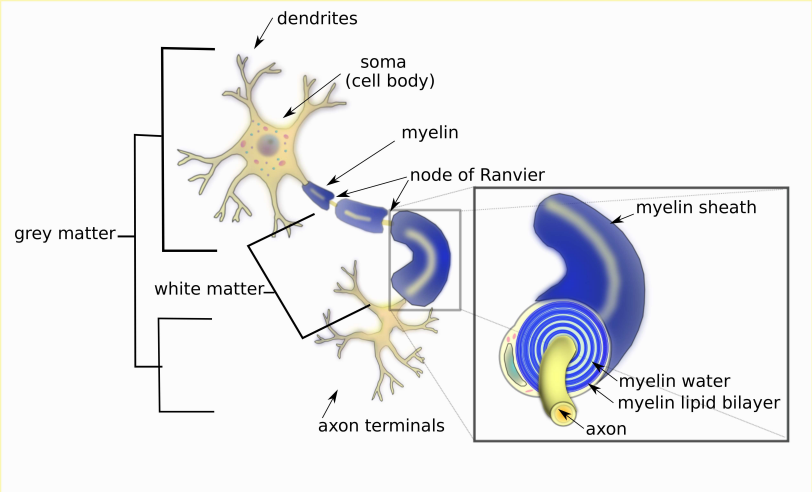

Figure 1.1: A schematic of a myelinated axon including the soma, dendrites, axon, myelin and axon terminals.

controls and support the communication between grey matter areas. Each axon is approximately 100 mm long and part of a whole wiring system extending to a total

length of 3×10^5 km (Nagarajan and Stevens 2008). For such a vast network the conduction velocity of an action potential is important for normal brain function and is regulated by myelin. The structural characteristics of myelin such as its thickness and the number of spaces along the axon (known as nodes of Ranvier) reduces the conduction leak and the cost of conducting an action potential vital for neuronal communication.

For many years, studies of learning, memory and psychiatric disorders were focused on the neuron and the chemical action of the synapse, with the white matter largely considered a passive component. However, the role of white matter in facilitating efficient information transfer between different brain regions is beginning to be increasingly recognised. Since the white matter conveys information between distinct brain regions along specific pathways, and the information transfer is modulated by the axon and myelin properties of those pathways, a deeper understanding of the white matter necessitates study of these distinct sub-components. In this thesis, an optimized pipeline for the non-invasive study of these aspects of white matter is developed, probing specific markers of white matter along specific pathways.

1.1 Motivation

Recent MRI advances in fast imaging methods and gradient technology enabled the development of quantitative techniques to quantify aspects of tissue microstructure in white matter. Diffusion weighted MRI probes the translational movement of water molecules at the micron scale. The anisotropy of the apparent diffusivity provides a window into microstructural organization of tissue. Importantly, however, the anisotropy is modulated by a host of factors including, but not limited to, the axon density, axon diameter, membrane permeability, myelination and architectural paradigm (the layout of the axons within the voxel). Thus, while diffusion MRI can

be a sensitive marker of white matter microstructure, it is not very specific. Development of these more specific white matter indices has potential to elucidate the role of individual differences in subcomponents of white matter on the brain function, and to better understand the impact of white matter microstuctural alteration in disease. Furthermore, by adopting advanced models of diffusion that (contrary to DT-MRI) recognise that water diffuses in different sub-components of tissue (e.g. intra- and extra-axonal spaces), can provide markers that are more specific to axonal properties. Development of these more specific white matter indices has the potential to elucidate the role of individual differences in subcomponents of white matter on brain function, and to better understand the impact of white matter microstructural alteration in disease. Furthermore, to determine their interdependence may shed light on whether changes in myelin alters neuronal cognitive function or vice versa.

1.2 Outline

This thesis combines a number of quantitative neuroimaging techniques in a novel and unique way. In particular, quantitative microstructural measures derived from quantitative magnetization transfer (qMT) imaging, multi-component relaxometry and advanced models of diffusion are combined and used to characterize white matter along specific anatomical pathways.

This thesis is organized as follows:

Chapter 2: Neuroimaging This chapter presents an overview of diffusion weighted MRI, quantitative magnetization transfer imaging and multi-component relaxometry, together with a brief summary of clinical and neuroscience applications. Some limitations and advantages of each method are discussed.

Chapter 3: Measurement uncertainties in qMT-derived parameters Magnetisation transfer imaging derives putative quantification of myelin content within each voxel. However, noise originating from different sources introduces variance in the inputs to the fitting, and thus uncertainty in the myelin estimate. This chapter uses a bootstrapping approach to examine the impact of the number of pre-processing steps in the qMT pipeline on the precision of derived parameters, aiming to finding the optimal pipeline for qMT.

Chapter 4: Tract-specific Measurements A novel method for tract specific microstructure measurements is introduced. This method, called *tractometry*, derives multiple quantitative indices of tissue microstructure (including those from diffusion MRI, qMT and multi-component relaxometry) along specific white matter pathways.

Chapter 5: Exploring the Asymmetry in MRI measurements Structural MR measurements provide us with the opportunity to explore the asymmetry within white matter structure. This chapter evaluates the asymmetry in white matter along specific tracts and within the whole white matter skeleton.

Chapter 6: Reproducibility in Tract-based Statistics Tract-based statistics (TBSS) provides estimates on the correlation between diffusion measurements and behaviour. However, to date, there have been no investigations into the reliability of this approach. This chapter uses a bootstrapping approach to evaluate the reliability of the method when assessing asymmetry in microstructure and microstructure-task performance correlations.

Chapter 2

Neuroimaging

Over the past twenty years MRI has become one of the most powerful non-invasive tools to study the human body. While MRI has found applications throughout the body, its remarkable contrast within the brain is where this imaging method has arguably the greatest impact. It now has become one of the main tools used by clinical neurology to diagnose many neuropathologies such as demyelinating diseases, stroke and tumours (Ge et al. 2001; Harris et al. 2004; Schonberg et al. 2006).

Throughout the early years many of the technical developments in MRI were driven by clinical need, where sequences such as diffusion-weighted imaging was used in cases such as acute ischaemia due to its unique brain contrast (Le Bihan and Breton 1985; Moseley et al. 1990). However, more recently, cognitive neuroscience has also been a driving force. Since the early nineties when brain activity was first detected using MRI, cognitive scientists have been using functional MRI (fMRI) to study brain function (Ogawa et al. 1992; Kwong et al. 1992). Diffusion-weighted imaging (DWI), can potentially study the brain's connections needed for brain function by acquiring information on the orientation of white matter tracts non-invasively (Le Bihan and Breton 1985; Basser et al. 1994a; Conturo et al. 1999). The ability to infer the amount of myelin throughout the brain from methods such as magnetisation transfer (MT) (Wolff and Balaban 1989; Wolff et al. 1991) and multicomponent relaxometry (Whittall and MacKay 1989; MacKay et al. 1994; Whittall et al. 1997) and other techniques that allow us to measure the diameter of the axon (Assaf et al. 2004)

potentially allows us to study the impact of white matter microstructure on cognition (Fields 2008).

While these different structural imaging techniques (DWI, restricted diffusion, MT and multicomponent relaxometry) provide complementary information about the architecture of white matter, they have never been implemented together to provide a more descriptive picture of white matter trajectory and microstructure. This thesis combines all these techniques in a novel way to potentially give us a better understanding of white matter microstructure, and the correlation between different white matter imaging indices.

2.1 Structural Neuroimaging Methods

In this section the structural techniques used within this thesis are described in more detail, starting with a brief description of the basics of magnetic resonance imaging (MRI) and then onto diffusion-weighted, restricted diffusion, magnetisation transfer and multi-component relaxometry imaging.

Basic MR

The popularity of MRI over other modalities is attributed to its sensitivity to a range of microenvironmental and chemical properties, such as relaxation times (T_1, T_2 and T_2^*). There are three main hardware components in a MRI: a main magnetic field (B_0), a magnetic field gradient system and a radio-frequency system (B_1). To be able to produce an image from these hardware components a sample must possess angular momentum. All subatomic particles (i.e. protons, neutrons and electrons) have a discrete amount of spin of either $\pm 1/2$, referring to the direction of rotation, thus nuclei with a even number of subatomic particles do not produce an overall angular momentum. Therefore, for there to be a net angular momentum nuclei must have

an odd number of protons or neutrons, such as ^{31}P, ^{1}H and ^{13}C, each possessing a magnetic dipole moment. Due to the prevalence of water in the human body hydrogen (^{1}H) is the most common nucleus studied in MRI. The signal from hydrogen within the body includes contributions from protons in water and non-aqueous protons such as lipids, proteins and nucleic acids.

In the absence of a magnetic field the spins in a sample are randomly distributed producing no net magnetic moment (no dominant spin direction). However, when an external magnetic field (B_0) is applied it will cause a torque on the spins causing them to align parallel or anti-parallel to the applied field. Due to a lower energy state more spins will align parallel to the field creating a net magnetic moment or magnetisation along the longitudinal axis. The net magnetisation vector (NMV) precesses, with a gyroscopic motion, about the direction of the main static field with an angular frequency that is directly proportional to the strength of the magnetic field known as the Larmor frequency. The NMV can be tipped away from its equilibrium position by exchanging energy with the RF system at the Larmor frequency - the process known as resonance. As the system relaxes back to equilibrium it emits RF that can be detected by the receive coil. Protons whose Larmor frequencies are within the range of frequencies (known as bandwidth) of the pulse will undergo relaxation, while the rest of the sample will provide zero signal. To acquire signal from only a small section or slice of the sample instead of the whole volume a spatial encoding magnetic field gradient is used to excite the sample, causing the Larmor frequency within the sample to vary with position.

There are two main relaxation mechanisms: the transfer of energy from the spin system to the lattice (spin-lattice or T_1 relaxation) and the loss of phase coherence in the transverse plane (spin-spin or T_2 relaxation). Spin-lattice or T_1 relaxation describes the process in which spins transfer energy from an RF pulse to its surrounding lattice to restore equilibrium, which in turn depends on the mobility of the lattice.

The rate at which this relaxation occurs (time it takes for the magnetisation to return to alignment with the longidutinal axis) is described by T_1 times. Spin-Spin or T_2 relaxation describes the process where spins lose coherence over time due to spin-spin interactions, resulting in a signal decay which in turn is described by T_2 times.

One of the most common MR sequences is the Carr-Purcell spin echo (SE) sequence (Hahn 1950; Carr and Purcell 1954). Spins are rotated into the transverse plane by a RF excitation pulse with a flip angle (FA) of 90° and after a certain time it uses a 180° pulse to refocus the spins to generate what is known as a spin echo signal. Initially after the 90° excitation pulse the longitudinal magnetisation is rotated into the transverse plane and the transverse magnetisation begins to decay, which in turn depends on the T_2 of the substance and the loss of phase coherence due to B_0 inhomoegeneties. After some time ($TE/2$) a 180° refocusing pulse is used to rotate the magnetisaiton in the x-plane causing the transverse magnetisation to regain coherence resulting in a spin echo. The amount of time between the initial excitation pulse and the detection of the spin-echo is known as the echo delay time (TE). The magnitude of the signal not only depends on how well the transverse magnetisation decays but also the recovery of longitudinal magnetisation. The amount of recovery or magnitude of signal depends on the rate of recovery or T_1 relaxation and the time allowed for the recovery to occur before another pulse is sent known as repetition time (TR). Importantly, the programmable sequence parameters TR and TE influence the effect T_1 and T_2 relaxation times of a substance have on the signal intensity. Thus, one can acquire different contrasts (T_1-weighted, T_2-weighted and proton-density (PD) weighted) by selecting different TEs and TRs (i.e. short TE (10-20 ms) and short TR (300-600 ms) will produce a T_1-weighted image).

Different tissues contain very different molecular structures, for example in cartilage the molecular structure is rigid and has very little motional energy at the Larmor frequency creating a long T_1 relaxation time and rapid de-phasing, short T_2 times. On

the other hand, tissue with small or unrestricted molecules will be more mobile creating long T_1 and T_2 times as in cerebrospinal fluid (CSF). Precise characterization of T_1 and T_2 within heterogenous structures such as the brain allows for greater tissue discrimination, segmentation, classification and sensitivity to pathological disorders as shown by Damadian in (1971). Variation in relaxation times has already been shown in Parkinson's disease (Baudrexel et al. 2010), multiple sclerosis (Ramani et al. 2002; Ge et al. 2001), Alzheimer's disease (Pitkänen et al. 1996), tumour characterisation (Tozer et al. 2011) and muscle disease (Sinclair et al. 2010). Initially T_1-weighted, T_2-weighted and proton density were used to observe brain abnormalities due to their sensitivity, however they are not specific on which white matter structure is creating the differences in measured signal.

Pulse Sequences

Many of SE pulse sequences used today are based on Carr and Purcell SE sequence such as the fast spin echo and echo planar imaging (EPI). Others modify the sequence as in the Carr-Purcell-Meiboom-Gill (CPMG) spin echo experiment where a train of spin echos is applied and is commonly used in T_2 imaging. Another common pulse sequence is the gradient echo sequence. It differs from the SE by having a smaller excitation pulse ($< 90°$) and no 180° refocusing pulse. Instead of a 180° RF pulse it applies a bipolar readout gradient to produce an echo. This is achieved by dephasing the spins with a negatively pulsed gradient before they are rephased by an opposite gradient with opposite polarity to generate the echo. The magnitude of the signal depends on the size of the longitudinal magnetization and the flip angle (FA) used. The lower the FA the smaller the amount of magnetisation tipped into the transverse plane, thus speeding up the recovery time of the longitudinal magnetisation allowing for shorter TR/TE and more importantly scan time. Thus, GE sequences tend to be faster than SE sequences leading to new contrasts between tissues and increased

signal magnitude in a shorter amount of time. Furthermore, when longitudinal magnetisation and transverse magnetisation are kept constant within GE sequences these sequences are known at steady-state sequences.

Steady-state refers to the equilibrium condition that comes about when the magnetisation experiences regularly spaced and rapid trains of radio frequency (RF) pulses conditional on $TR < T_1$, whereby the magnetisation does not fully recover between pulses. The ability for magnetisation to be in steady state depends on tissue parameters, such as T_1 and T_2, and sequence parameters, such as TR and flip angle (FA). Most importantly its dependence on the phase between the magnetisation and the axis of the RF pulses gives pulse programmers the flexibility to manipulate the transverse magnetisation different ways such as spoiled gradient recalled echo (SPGR) and balanced-steady-state free precession (bSSFP).

MR Inhomogeneity

Quantitative imaging is full of challenges especially as the main magnetic field increases. The two major issues are radio frequency (B_1) and static field (B_0) inhomogeneities that cause artefacts that lead to a decrease in the accuracy of these quantitative values (Volz et al. 2010). B_1 inhomogeneity causes variation in the flip angle (FA) and the sensitivity of the receive coil across the field-of-view causing variation within the signal across an image volume. B_0 inhomogeneity is a result of field discontinuities not caused by the applied linear gradients, resulting in spins being encoded in the wrong position leading to image distortion. Field discontinuities can be found at tissue borders with very different magnetic susceptibility, such as air and bone. To increase the accuracy of quantitative values B_0 and B_1 field maps are used to correct field inhomogeneities throughout the acquired images.

There have been several proposed B_1 mapping methods over the years. All aim to quantify the RF excitation angle compared to the nominal or desired angle. A few

of the more popular magnitude based methods are briefly described here. First, the most common method is the double angle method (DAM) where the actual angles are calculated from signal ratios of two different nominal excitation angles (where one is twice the RF amplitude of the other) (Stollberger and Wach 1996; Cunningham et al. 2006). For a spin-echo pulse sequence the ratio of the two images can provide a scaling factor (α_{corr}) to correct the nominal amplitude (α_1) ($\alpha_{corr} = 1/\alpha_1 \arccos(S_1/(2S_2))$) when the two images are acquired with identical TE, TR and refocusing pulse. Second, based on the gradient echo (GE) sequence at large excitation angles the signal is linearly-fitted at the zero crossing (or the signal null) corresponding to the excitation angle of 180° (Dowell and Tofts 2007). Thirdly, the actual flip angle imaging (AFI) method is based on fast low angle shot (FLASH) imaging, where the flip angle is held constant and the ratio of images with two different repetition times are taken (Yarnykh 2007). Phase based methods are less common and are based on the use of composite RF pulses to create B1-dependent phase offsets in the image (Morrell 2008) or a Bloch-Siegert shift to create a B_1 dependent signal phase (Sacolick et al. 2010).

On the other hand there is one B_0 method that is used more than any other and is based on phase differences (Jezzard and Balaban 1995). A spin-echo or a gradient-echo is used to measure the phase difference between two different images acquired at different echo times to create a map to correct for B_0 inhomogeneity.

Summary

Within this thesis I will focus on white matter structural imaging. The sequences used to quantify white matter structure are quantitative T_1, T_2, magnetisation transfer and restricted-diffusion. Multi-component quantitative T_2 methods probe different T_2 relaxation times that different brain structures have, where relaxation times between 10-50 ms are thought to be from water trapped between the myelin bilayers. The

myelin water fraction (MWF) is the ratio of water trapped within the myelin bi-layers (short T_2) to the total water present in the voxel. Magnetisation transfer imaging provides an estimate of the macromolecular proton fraction (MMPF), which is a measure of the number of trapped protons in the macromolecular pool, such as myelin, relative to the total number of protons present. In contrast to these two techniques, diffusion-weighted imaging, provides us with unspecific information on white matter structure since its sensitive to differences in myelination, axonal density, axonal diameter or orientation of fiber bundles. On the other hand, diffusion-weighted images can give detailed images on the orientation of the fibre tracts. If one acquires diffusion images at multiple-diffusion times more specific measures, such as axon diameter, can be estimated. The specifics of these techniques are outlined in the sections that follow.

2.1.1 Diffusion-Weighted Imaging

Diffusion-weighted imaging (DWI) obtains image contrast from the self-diffusion of water molecules. Self-diffusion involves translational movement of molecules via thermally driven random motion and was first characterised by the botanist Robert Brown in 1828. Within living tissue apparent-diffusion of water molecules changes due to various boundaries such as cellular structure. However, it is impossible to determine or predict the motion of a single water molecule in a sample. Moreover, in the limit of a large number of water molecules Albert Einstein proved that the squared displacement averaged over all the molecules in the sample is proportional to diffusion time τ_D (Einstein 1905):

$$< r^2 >= 6D\tau_D \tag{2.1}$$

Spin diffusion measurements began about half a century after Einstein's discovery when both Hahn (1950) and Carr and Purcell (1954) demonstrated that self-diffusion can be measured using nuclear magnetic resonance (NMR). In 1965 Stejskal and Tanner introduced the pulsed field gradient (PFG) spin echo method which allowed one to measure diffusion in liquids (Stejskal and Tanner 1965). Within the PFG sequence the initial gradient pulse is applied following a 90° excitation pulse labeling a spin according to its spatial location (i.e. its z-coordinate when a Z gradient, g, is applied). Any type of motion after this pulse causes molecules to acquire phase shifts $\Phi(z_1)$ of their transverse magnetisation M_{xy}. Then a 180° pulse is applied reversing or refocusing M_{xy} and the second gradient pulse after a diffusion time, τ_D, alters the phase by $-\Phi(z_2)$. If the spins were stationary the phase increments caused by the two gradients pulses cancel giving no net phase change. On the other hand the phase accrual for mobile spins are not perfectly rewound by the second gradient, resulting in a phase shift. If the spins moved incoherently a distribution of phases is created (loss of phase coherence), leading to signal attenuation measured by:

$$S(TE) = S(0) \cdot \exp\left[-bD\right] \tag{2.2}$$

The two unknowns in this equation are S_0, the echo amplitude without diffusion encoded-gradients and the diffusion coefficient, D. b is a independent experimental variable determined by pulse sequence parameters. The b-value for trapeziodal diffusion-encoding gradients pulses applied in the x direction of duration (δ) and amplitude (g), separated in time by Δ yields:

$$b_{xx} = (\gamma g)^2 \left[\left(\Delta - \frac{\delta}{3}\right)\delta^2 + \frac{\epsilon^3}{30} - \frac{\epsilon^3}{6}\delta\right] \tag{2.3}$$

where G is the strength of the gradient pulse applied before and after the 180 radio frequency pulse and ε is the rise and fall times for the diffusion gradients. Acquiring

data for more than one b-value allows one to solve for the diffusion coefficient when the echo time (TE) is the same for each b-value.

The application of spin diffusion measurements in MRI by Le Bihan and Breton in 1985 created a new contrast technique coined 'diffusion-weighted' imaging. For many MRI experiments diffusion times are in the order of 50-100 ms making the average displaced distance measured to be around 10-15 μm. Even at such small distances water molecules are hindered by cell membranes, inclusions, fibres and/or macromolecules reducing their overall displacement. Consequently, the diffusion coefficient appears to be reduced when measured providing us with the term 'apparent diffusion coefficient' (ADC). For tissue the average ADC has been measured to be 0.7×10^{-3} mm^2s^{-1} significantly smaller than the diffusion of free water 3×10^{-3} mm^2s^{-1} (Le Bihan et al. 1986). This novel contrast started to be used clinically in early 1990s for certain pathological states or injuries, such as ischemia and tumours (Moseley et al. 1990; Le Bihan et al. 1988). Shortly after the introduction of DWI, Moseley noticed that signal attenuation was dependant on the orientation of the diffusion-sensitising gradient (Moseley et al. 1990). Applying gradients along the three orthogonal axis permits the orientational dependence of the ADC to be evaluated. For instance, if the diffusion weighted intensities are the same in all three directions the diffusion is said to be isotropic. On the other hand if at least one of these directions has higher intensity than the other two the tissue is described as anisotropic. As a result, a substantial amount of information about tissue structure can be interpreted from only these three diffusion-encoded images. However, in highly organised tissues, such as white matter, sampling the ADC along only three directions is insufficient to completely describe the diffusion profile.

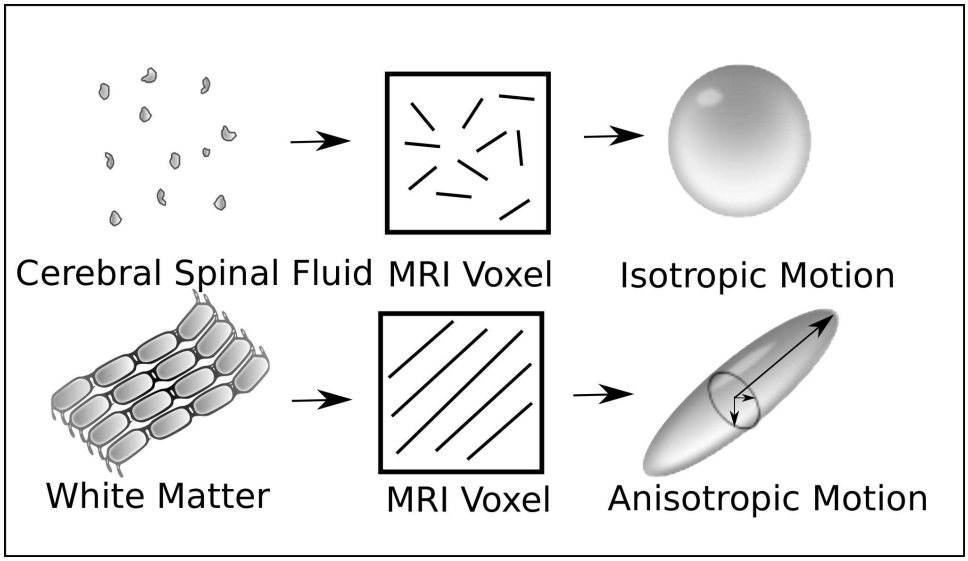

Figure 2.1: Schematic of the diffusion weighted imaging within grey and white matter.

Diffusion Tensor

In 1994 Basser et al. introduced diffusion tensor imaging (DTI) a three-dimensional technique that characterised a tissue's physical properties, microstructure and architectural organisation, unlike any other imaging modality that came before it. This technique makes it practical to acquire knowledge of white matter fibre orientation and microstructure from a series of diffusion-weighted images in which the gradients are applied in different directions. The diffusion profile is represented by a symmetric matrix, which represents the diffusion tensor:

$$D = \begin{pmatrix} D_{xx} & D_{xy} & D_{xz} \\ D_{xy} & D_{yy} & D_{yz} \\ D_{xz} & D_{yz} & D_{zz} \end{pmatrix} \tag{2.4}$$

The three diagonal terms of the diffusion tensor describe the molecular mobility along the x, y and z axes. In contrast, the three off-diagonal terms describe the degree of correlation between the diffusion along the primary axes (x,y,z). The signal measured

during a diffusion tensor sequence is a modification to equation 2.2 to incorporate the tensor and is given by:

$$S = S_0 \cdot \exp\left[-bg^T Dg\right] \tag{2.5}$$

where g is a vector for the motion probing gradients (MPG) and the superscript T indicates the transpose of a vector. Since the tensor is symmetric (i.e. $D_{xy} = D_{yx}$) there are only six unique elements of the diffusion tensor (D), thus only six independent diffusion-encoding gradient directions are required. The matrix D is diagonalized to provide eigenvectors, e_i, and non-zero eigenvalues, λ_i $(i = 1, 2, 3)$, that correspond to the main diffusion directions and diffusivities. The diffusion tensor is often represented by an ellipsoid, whereby the principal axes is given by the eigenvectors and the lengths are represented by the diffusion distance for a given time which is proportional to the square root of the diffusivity (eigenvalues). Eigenvectors and eigenvalues can be seen in the following matrix factorisation (Basser et al. 1994b)

$$D = \begin{pmatrix} D_{xx} & D_{xy} & D_{xz} \\ D_{xy} & D_{yy} & D_{yz} \\ D_{xz} & D_{yz} & D_{zz} \end{pmatrix} = \begin{bmatrix} e_1 & e_2 & e_3 \end{bmatrix}^T \begin{pmatrix} \lambda_1 & 0 & 0 \\ 0 & \lambda_2 & 0 \\ 0 & 0 & \lambda_3 \end{pmatrix} \begin{bmatrix} e_1 & e_2 & e_3 \end{bmatrix} \tag{2.6}$$

Measuring the signal at different gradient directions can provide different points on the ellipsoid surface giving its size, shape and orientation (Figure 2.2). The mean-squared displacement of molecules (average ellipsoid size) is described by the mean diffusivity, which depends on the amount of barriers in the sample. Rotationally invariant scalar indices can be calculated, such as the trace, to provide an overall amount of diffusivity within a voxel (Papadakis et al. 1999):

$$Tr(\underline{D}) = \lambda_1 + \lambda_2 + \lambda_3 \tag{2.7}$$

The most commonly used index is fractional anisotropy (FA), which measures the fraction of D that can be assigned to anisotropic diffusion and varies between 0 (isotropic diffusion) and 1 (for infinite anisotropy (i.e., with $\lambda_1 \gg \lambda_2 = \lambda_3$)) (Basser and Pierpaoli 1996). FA can be calculated using the following equation:

$$FA = \frac{\sqrt{3[(\lambda_1 - <\lambda>)^2 + (\lambda_2 - <\lambda>)^2 + (\lambda_3 - <\lambda>)^2]}}{\sqrt{2(\lambda_1^2 + \lambda_2^2 + \lambda_3^2)}} \tag{2.8}$$

where $<\lambda>$ is the mean of the three eigenvalues λ_i. A principal eigenvector map is weighted by FA to provide a colour-coded map dependent on orientation where the x, y and z vector components are represented by the colours red, green and blue, respectively (Pajevic and Pierpaoli 1999) (Figure 2.2 A). These maps have been shown to be highly sensitive to subtle disease processes not normally seen with other MRI contrast sequences (Moseley 2002). The quality of diffusion data is dependent on the choice of diffusion gradient directions and orientation of the sample (Basser and Pierpaoli 1996; Skare et al. 2000). Large diffusion gradient can lead to an over-estimate of diffusion anisotropy due to a reduction of the signal to noise ratio (SNR) (Pierpaoli and Basser 1996). Furthermore, only using six diffusion-encoded gradient directions increases the sensitivity of the resulting diffusion map to noise and increasing the number of measurements improves noise performance and precision (Papadakis et al. 1999). For n number of motion probing directions the diffusion tensor is now solved by linear equations:

$$\begin{bmatrix} g_{x1}^2 & g_{y1}^2 & g_{z1}^2 & 2g_{x1}g_{y1} & 2g_{y1}g_{z1} & 2g_{z1}g_{x1} \\ \vdots & \vdots & \vdots & \vdots & \vdots & \vdots \\ g_{xi}^2 & g_{yi}^2 & g_{zi}^2 & 2g_{xi}g_{yi} & 2g_{yi}z_{zi} & 2g_{zi}g_{xi} \\ \vdots & \vdots & \vdots & \vdots & \vdots & \vdots \\ g_{xn}^2 & g_{yn}^2 & g_{zn}^2 & 2g_{xn}g_{yn} & 2g_{yn}g_{zn} & 2g_{zn}g_{xn} \end{bmatrix} \begin{bmatrix} D_{xx} \\ D_{yy} \\ D_{zz} \\ D_{xy} \\ D_{yz} \\ D_{zx} \end{bmatrix} = \begin{bmatrix} -\frac{1}{b}\ln\frac{S_1}{S_0} \\ \vdots \\ -\frac{1}{b}\ln\frac{S_i}{S_0} \\ \vdots \\ -\frac{1}{b}\ln\frac{S_n}{S_0} \end{bmatrix} \tag{2.9}$$

where $g_i = (x_i, y_i, z_i)^T$ is the MPG vector, S_0 is the signal intensity without MPGs and S_i is signal intensity for each MPG vector $(i = 1, \ldots, n)$ (Masutani et al. 2003). Tensor imaging measures anisotropy per voxel providing directional information used in tractography or fibre tracking in fibrous tissues, such as white matter and muscle (Basser and Pierpaoli 1996; Basser and Jones 2002). Tensor information is processed using two main fibre tracking algorithms: deterministic streamline (Mori et al. 1999; Conturo et al. 1999; Jones et al. 1999; Mori et al. 1999; Basser et al. 2000) and probabilistic tractography (Parker et al. 2003; Parker et al. 2003; Poupon et al. 2000).

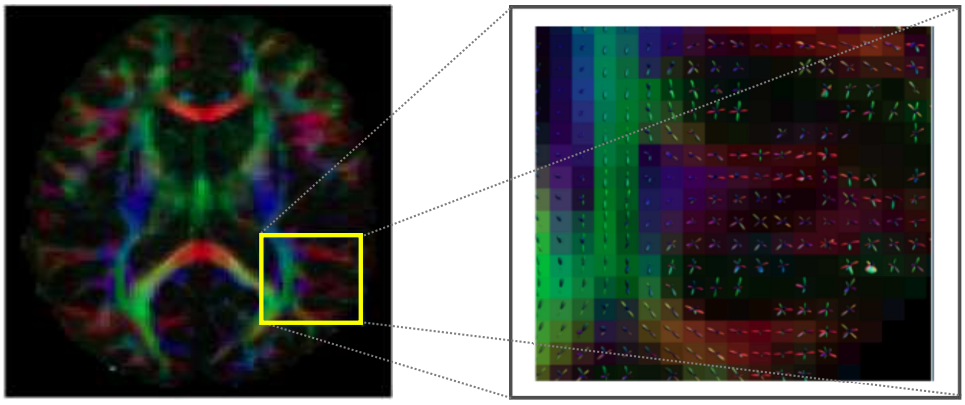

Figure 2.2: A) Example of colour encoded fibre orientation maps. B) Constrained spherical deconvolution (CSD) overlaid onto a region of interest drawn on the colour encoded fibre orientation map.

Deterministic algorithms rely on line propagation techniques to reconstruct white matter pathways by the following procedure: identification of a suitable starting position (the seed point), propagated along the estimated fibre orientation and then terminated when appropriate termination criteria are met (Mori and van Zijl 2002). Reliable reconstruction of specific pathways is dependent on suitable placement of seedpoints and waypoints to constrain the tracking, which - in turn - depends on the end user's knowledge of neuroanatomy (Catani et al. 2002; Catani and Thiebaut de Schotten 2008). For white matter tracts that run in close proximity to each other

regions, of interests are needed with Boolean logic for reconstruction: AND, OR and NOT gates (e.g. NOT-gates are used to stop tracking going past a ROI) (Conturo et al. 1999). Deterministic tractography is still one of the most popular white matter tracking algorithms even with two major limitations. First, the deterministic algorithm only provides a single estimate of trajectory for each supplied seed point, thus ignoring branching fasiculi. Secondly, there is no indication of the confidence that can be assigned to the reconstructed trajectory. Noise present in the system introduces uncertainty in the estimate of fibre orientations (i.e. e_1) (Basser and Pajevic 2000; Jones 2003) potentially leading to errors within a pathway (Lazar and Alexander 2003; Tournier et al. 2002; Lori et al. 2002; Jones 2003).

Probabilistic algorithms make an effort to overcome these limitations by providing a probability distribution for a trajectory, instead of a single fit. Starting from a seed point the most likely direction for the next step is chosen from a distribution of orientations, the white matter track is propagated this way where each step is selected at random from a local probability density function (PDF) of fibre orientations. This procedure results in a number of potential pathways through a specified seedpoint where each voxel is assigned a value for the percent of pathways that pass that voxel originating from the seedpoint. Thus, areas of the brain that contain higher densities of resulting tracks have a higher probability to be connected to the seedpoint (Behrens et al. 2003; Parker et al. 2003). In contrast, there are cases where a lower probability is unexpectedly assigned, such as when a tract branches off to multiple destinations reducing the proportion of tracks reaching any one of the destinations. The probability density function (PDF) and the estimation of uncertainty of the diffusion tensor (Parker et al. 2003; Tournier et al. 2003) are estimated either using bootstrap methods (Jones 2008b; Jones and Pierpaoli 2005; Jones 2003; Lazar and Alexander 2005), Bayesian inference methods (Behrens et al. 2003) or Monte Carlo methods (Parker et al. 2003). One should note that streamline probabilistic tracking

is no more accurate than deterministic tracking, therefore they are affected by the same limitations. The probabilistic technique only expresses the 'precision' a pathway can be reconstructed from the given data and model algorithm. Hence, the results do not determine the 'connectivity' of white matter pathways (Jones 2010).

Factors that Affect Diffusion Tensor Measurements

Diffusion-weighted imaging is inherently sensitive to motion of water molecules on the order of 5-15 μm, thus other motions such as subject motion, breathing motion and even cardiac pulsation will lead to significant signal phase shifts leading to a decrease in image quality (Le Bihan et al. 1988; Chenevert and Pipe 1991; Le Bihan and Turner 1991; Wirestam et al. 1996; Skare and Andersson 2001; Jones and Pierpaoli 2005; Nunes et al. 2005). There are also machine-dependent errors, such as eddy currents, gradient nonlinearity, B_0 and B_1 inhomogeneities that can effects image quality (Alexander et al. 2001).

In the 1990s the focus on improved data quality was to optimise the pulse sequence. To reduce motion sensitivity a rapid image technique single-shot echo planar imaging (EPI) was introduced. However, single-shot data acquisitions suffer from artefacts caused by B_0 susceptibility changes at air/tissue interfaces and geometric distortions produced by eddy currents. Many approaches have been applied to reduce B_0 artefacts such as shielded gradients, postprocessing, or more advanced pulse sequences (Provenzale and Sorensen 1999; Janke et al. 2004; Kennedy and Zhong 2004). To reduce the artefacts within EPI a shorter echo train length and smaller echo spacing have been introduced. Two such methods are parallel imaging and segmented k-space sampling. Parallel imaging was developed in the late 1990s (Pruessmann et al. 1999) and has been a popular method to reduce EPI distortions and B_0 inhomogeneities. Another effect of large diffusion gradients is eddy currents, which depending on their magnitude and direction lead, to either translation, shearing or scaling (Haselgrove

and Moore 1996) The fast switching of the diffusion gradients can also induce a Lorentz force on the gradient coil causing mechanical motion or vibration of the coil (Boujraf et al. 2001). To reduce the effects of eddy currents bipolar gradients have been used (Alexander et al. 1997; Reese et al. 2003). With the help of increased gradient hardware quality and eddy-current compensation schemes in modern scanners these distortions are less problematic.

An effect on data quality that is implicit to *in vivo* is cardiac pulsation, which leads to nonlinear motion and local deformations corrupting the final diffusion signal (Enzmann and Pelc 1992; Poncelet et al. 1992; Turner et al. 1990; Jiang et al. 2002; Skare and Andersson 2001). Motion of the order of 0.5 mm has been seen during the cardiac cycle (Enzmann and Pelc 1992; Poncelet et al. 1992) leading to signal dropouts and residual misalignments and, in turn, errors in diffusion estimates. To avoid these artefacts cardiac gating is used, where the acquisition is triggered to the cardiac cycle. Unfortunately, the effective pulse repetition time for this acquisition is dependent on the heart rate of the participant leading to longer scan times. Another common confound in *in vivo* experiments is partial volume effects due to cerebrospinal fluid contamination. Fortunately, it mainly occurs in voxels around the ventricles and the perimeters of the brain parenchyma (Alexander et al. 2001; Papadakis et al. 2002). CSF-contamination leads to elevated ADC and decreased FA values, subsequently affecting the delineation of tracts close to ventricles since these voxels are not assigned as WM and will be ignored during tracking algorithms. A number of models have been introduced to separate the diffusion properties of the brain tissue from the surrounding free water (Alexander et al. 2001; Behrens et al. 2003; Papadakis et al. 2002; Pasternak et al. 2009). The method by Pasternak (2009) is used within this thesis since it does not require additional data-sets with different b-values (Pierpaoli and Jones 2004) or suffer from reduced SNR as in the fluid-attenuated inversion recovery technique (Papadakis et al. 2002). Pasternak's

'Free Water Elimination' (FWE) models two compartments, tissue and CSF, from the diffusion signal by imposing a bi-tensor model with additional biological and physical constraints, such as local smoothness constraints on the tissue compartment (Pasternak et al. 2009).

There are a number of factors that affect the diffusion signal that are of interest ranging from microscopic axons and myelin sheaths, to large structures like fibre bundles. If there are a number of heterogenously orientated fibres the diffusion signal within the voxel will appear isotropic when modeled by DTI, thus masking the small differences within microscopic factors. Knowing such effects it is difficult to interpret a change in diffusion anisotropy and conclude which factor actually accounts for the change (Wheeler-Kingshott and Cercignani 2009). There are a number of possible explanations for a decrease in FA for example: a decrease in principal diffusivity, an increase in the diffusivity perpendicular to the main axis (radial diffusivity) and a change in both principal and perpendicular diffusivity. Even though it was first thought that diffusion anisotropy was due to structures such as myelin, it has been found through histological staining that anisotropic diffusion can appear in immature mammals even before myelin exists (Wimberger et al. 1995).

A set of studies were conducted to determine the origin of anisotropy in white matter and found that intact cell membranes were the main determinant of anisotropy, although myelination did modulate anisotropy (Beaulieu and Allen 1994a; Beaulieu and Allen 1994b; Beaulieu and Allen 1996; Farrell et al. 2010). Over the years there has been a number of studies trying to interpret such changes within diffusion anisotropy and used histological measurements to try to interpret diffusion measurements (Beaulieu and Allen 1994b; Wimberger et al. 1995). Correlations between histological myelin measurements and diffusion experiments have been shown to be correlated especially within disease models (Peled et al. 1999; Klawiter et al. 2011). Furthermore, it has been shown that axonal loss did not cause a decrease in principal

diffusivity (Song et al. 2002; Herrera et al. 2008). Therefore, caution should be taken when interpreting changes in regions of heterogeneous fibre orientations using diffusion tensor models, especially as a proxy marker of WM integrity.

New Diffusion Models Beyond the Tensor

Most diffusion MRI studies still use the tensor model due to its simplicity even though it has been shown numerous times that it is inadequate in regions of heterogeneous orientations, like 'crossing fibres' (Tuch et al. 2002; Alexander et al. 2002; Tuch et al. 2003; Wedeen et al. 2005; Tournier et al. 2004; Anderson 2005). The amount of heterogeneous orientations within the brain has been found to be more common than initially thought (a third of all WM voxels) leading to high amount of orientational inaccuracies when modeling the diffusion signal by a diffusion tensor (Behrens et al. 2007). There are a number of factors that can cause heterogeneous orientations such as curving, fanning, kissing and crossing to name a few (Figure 2.3). Measures of anisotropy, FA and axial and radial diffusivities, are very sensitive to intra-voxel orientational dispersion (Alexander et al. 2001; Beaulieu 2002; Wheeler-Kingshott and Cercignani 2009), furthermore orientational issues in tensor based tractography lead to either false-positive or false-negative connections (Alexander et al. 2001; Behrens et al. 2007). Due to these limitations and issues of diffusion tensor methodology there has been a number of new higher order models that attempt to model the underlying tissue more accurately. A few of these models are: diffusion spectrum imaging (DSI) (Wedeen et al. 2005), Q-ball imaging (QBI) (Tuch 2004), combined hindered and restricted model of diffusion (CHARMED), diffusion kurtosis imaging (DKI)(**?**), (Assaf et al. 2004), spherical deconvolution (SD) (Tournier et al. 2004; Anderson 2005) and combining SD and residual bootstraps to acquire a probability tracking algorithm (Jeurissen et al. 2011). CHARMED and SD were used within this thesis and will be briefly described in the next two sections.

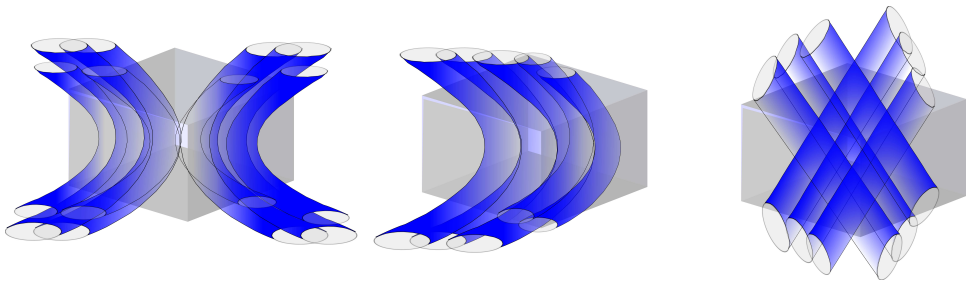

Figure 2.3: Schematic of possible complex fibre orientations within a MRI voxel. A) Kissing fibres B) Curving/bending fibres C) Crossing fibres.

Combined Hindered and Restricted Diffusion

This novel technique extends diffusion imaging by separating its signal into two components: hindered and restricted water diffusion - known as the combined hindered and restricted water diffusion (CHARMED) model (Assaf et al. 2004). The CHARMED model assumes there are two different diffusion environments that contributed to the net signal decay: hindered diffusion in the extra-axonal volume (including extra- and intra-cellular spaces) and restricted diffusion in the intra-axonal volume (Figure 2.4). The hindered diffusion compartment is characterised with a single diffusion tensor (Gaussian diffusion), while the restricted compartment is characterised using a model of restricted diffusion within cylinders (non-Gaussian diffusion).

The restriction of water molecules in a system is dependent on the diffusion time in a MR experiment. If the diffusion times are very short most molecules will move freely without reaching any boundaries. As the diffusion times increases a threshold is reached where the diffusion distance equals the characteristic size of a boundary (i.e. axon diameter). The physical process that dominates the signal decay at such high b-values is restricted diffusion, while at low b-values hindered diffusion is more significant. The volume fraction of the restricted diffusion provides an estimate of the axon density within a voxel. Restricted diffusion and axon density has the possibility to be sensitive to a wide range of WM pathologies involving axon changes. Application

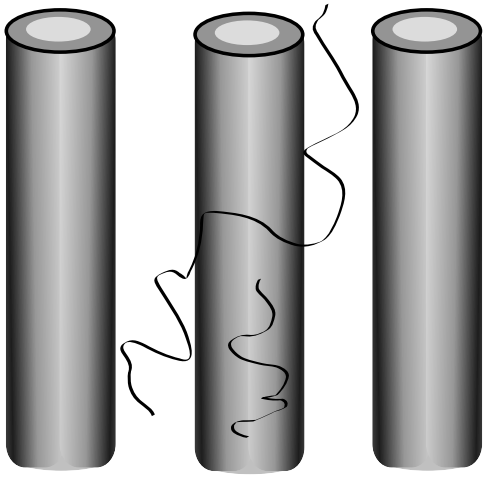

Figure 2.4: Schematic of the CHARMED diffusion model showing the two modes of diffusion in white matter: hindered outside the cylinders and restricted within the cylinders (Assaf et al. 2004).

of this approach has not been widely used since it requires more than one 3D diffusion acquisition with different b-value shells to be able to characterise both the hindered and restricted compartments.

Spherical Deconvolution

Spherical deconvolution goes beyond the diffusion tensor model by assuming the diffusion weighted signal is a linear combination of various fibre populations present within a voxel (Tournier et al. 2004). This method increases the number of potential fibre populations to infinity allowing the summation to be an integral over the distribution of fibre orientation when assuming a particular convolution kernel (Tournier et al. 2004; Anderson 2005). This technique assumes that each fibre population generates a diffusion weighted profile, where the measured diffusion signal profile is defined by spherical convolution of response function with fibre orientation distribution (FOD). Thus, the FOD can be estimated by applying spherical deconvolution of the response function to the measured diffusion signal. The first few applications of spherical deconvolution showed that it was susceptible to noise leading to a constrained spherical deconvolution model (Tournier et al. 2007). Within the constrained model negative

values are minimised within the reconstructed FOD, since these values were biologically impossible. Results from spherical deconvolution using constrained spherical deconvolution can be seen in Figure 2.2 B.

There have been many different spherical deconvolution methods that differ from the original implementation by Tournier et al. (2004) where different convolution kernels are assumed, such as a diffusion tensor model (Anderson 2005; Dell'Acqua et al. 2007; Dell'acqua et al. 2010; Kaden et al. 2007; Kaden et al. 2008).

2.1.2 Magnetisation Transfer

Magnetisation transfer (MT) imaging is a magnetic resonance (MR) method that harnesses information on the relative density of macromolecules within the brain. This technique was first demonstrated using continuous-wave saturation by Wolff and Balaban (1989) using an animal spectrometer. MT can provide quantifiable information on macromolecular components such as: protein, lipids and cellular membranes, which are invisible to conventional longitudinal T_1 and transverse T_2 scans due to their very short T_2 decay times ($\sim 10\mu s$, broad frequency line widths > 10 kHz) (Wolff et al. 1991; Wolff and Balaban 1989; Portnoy and Stanisz 2007; Samson et al. 2006). Furthermore, MT has been demonstrated to be a valid biomarker for white matter (WM) pathologies such as; inflammation, demyelination (loss of myelin), and axonal loss (Stanisz et al. 2004; Stanisz et al. 1999; Sled and Pike 2001).

Most MT acquisitions apply an off-resonance radiofrequency (RF) pulse that selectively saturates the macromolecular magnetisation. Off-resonance pulses causes water protons to transfer magnetisation from the saturated macromolecules to free water protons, through cross-relaxation or chemical exchange resulting in a decrease in the measurable free pool's signal. (Kucharczyk et al. 1994; Ceckler et al. 1991) (Figure 2.5). Until recently most magnetisation transfer effects were reported in terms

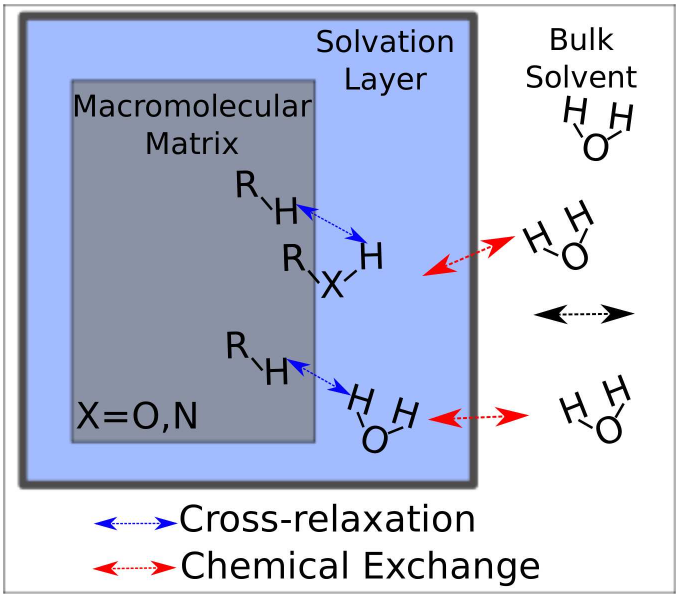

Figure 2.5: Schematic of the molecular model for magnetisation transfer. Magnetisation transfer can be from either chemical exchange between the bulk solvent and the solvation layer or cross-relaxation between the macromolecular matrix and hydroxyl or amine groups (X = O,N) which in turn exchanges rapidly with the bulk solvent. (Liepinsh and Otting 1996; Ceckler et al. 2001)

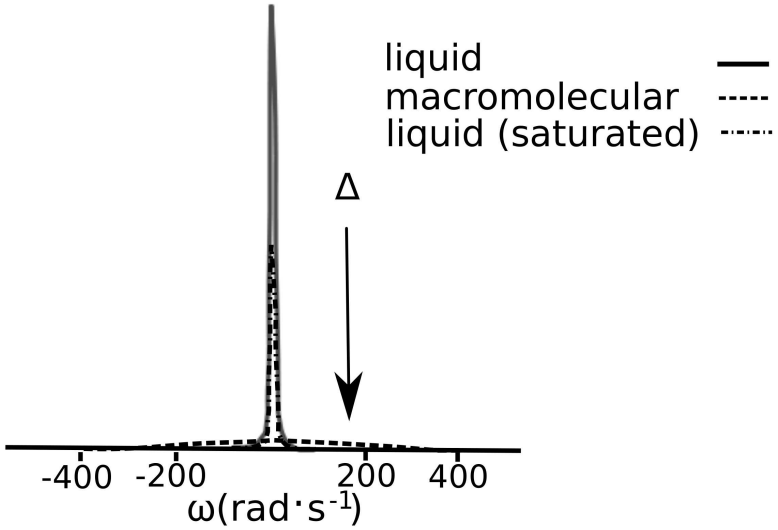

Figure 2.6: Representation of absorption lineshapes for the two pools.

of a MT ratio (MTR). MTR is calculated from only two images with and without the saturating pulse and are maps of the percent signal loss caused by the MT saturation pulse (Dousset et al. 1992). This ratio, however, is influenced by a complex combination of biological (including T_1 making it difficult to separate the effects of reduced macromolecular density or increased water) and experimental parameters (making it difficult to examine particular pathological syndromes between different labs)(Dousset et al. 1995; Does et al. 1998; Dousset et al. 1995; Deloire-Grassin et al. 2000; Gareau et al. 2000). Different pathologies are characterised by either an increase in water content arising from edema or inflammation or a decrease in nonaqueous tissue caused by demyelination and/or axonal loss, thus making it impossible to pinpoint which pathological processes are accountable for the decrease in MTR. As a result a number of groups have introduced quantitative MT (qMT) approaches using a range of different frequency offsets (Δ) modelling both experimental and biological parameters (Sled and Pike 2000b; Ramani et al. 2002). Providing a more informative picture, such as the macromolecular proton fraction (includes myelin) also known as a MMPF-map. Even though the MMPF-map does not provide an independent measure of myelin there is increasing evidence that changes from demyelinating diseases are reflected in a decrease in the value of MMPF (Sled and Pike 2001; Tozer et al. 2005; Davies et al. 2004; Levesque et al. 2005).

Two-pool Model

The most widely adopted quantitative magnetisation transfer (qMT) model for the human brain is the two-pool model; pool A (free water) consisting of mobile spins and pool B (macromolecular-bound) consisting of restricted or immobile spins. Different chemical environments and distinct spectroscopic line shapes characterise protons from each pool. Protons within the free pool have long T_2 times and are represented by a sharp lineshape, whereas the macromolecular pool is represented by a broad

absorption lineshape due to its short T_2 times (Figure 2.6). Having such a broad absorption lineshape means that the macromolecular pool to be more sensitive to off-resonance irradiation.

Pool B is selectively saturated by applying a radio-frequency (RF) pulse several kilohertz off-resonance from the Larmor frequency leading to magnetisation transfer between Pool A and B and an attenuation in the MR signal (Wolff and Balaban 1989) (Figure 2.7). The amount of attenuation is a function of RF parameters (amplitude(B), duration (τ), shape (e.g. Gaussian), duty cycle, frequency offset), the concentration of macromolecules and the exchange rate between the two pools. Importantly, other unwanted factors have been shown to affect attenuation are: water content, non-myelin macromolecules (as in neuroinflammation) and field inhomogeneities if not corrected for (Stanisz et al. 2004; Stanisz et al. 1999; Sled and Pike 2001).

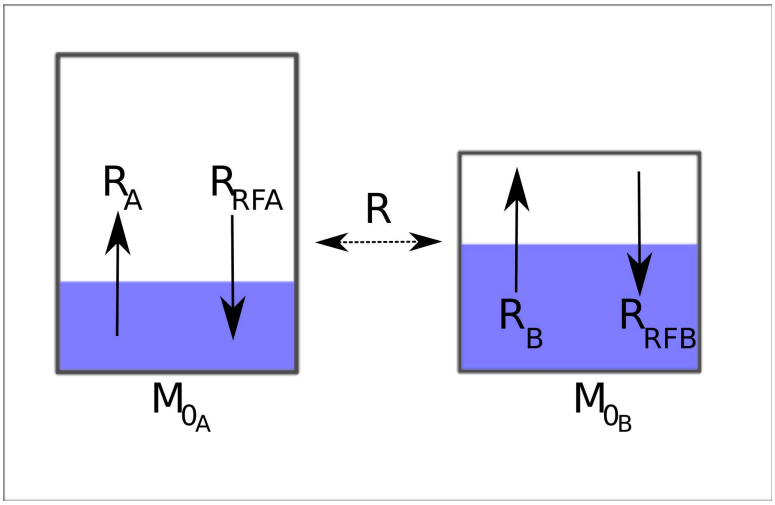

Figure 2.7: Two-pool model of magnetisation transfer where the shaded areas represent saturated spins (Henkelman et al. 1993).

Within the two-pool model a number of biological properties are modeled including the magnetisation exchange between the two pools (R), longitudinal (T_1) and transverse (T_2) relaxation times of free water and macromolecular protons and relative

number of macromolecular protons. Figure 2.7 shows the corresponding relaxation rate for longitudinal magnetisation for each pool, R_A and R_B, their loss of longitudinal magnetisation due to RF irradiation $R_{RFA,B}$ and the total number of spins $M_0^{A,B}$. Selectively modifying the magnetisation state of pool B using off-resonance RF pulses the relaxation properties and the exchange rate of pool B can be inferred by observing the change in pool A.

Henkelman et al. (1993) were among the first researchers to characterise the magnetisation transfer phenomenon mathematically using a non-Bloch behaviour and non-Lorentzian lineshapes for the bound pool. Using a continuous-wave (CW) MT experiment consisting of a single long ($> 5s$) with constant amplitude RF pulse the magnetisation is determined by solving modified Bloch equations by assuming the system is in steady-state(Henkelman et al. 1993). It was shown within CW MT experiments the signals in the brain attenuate differently: white matter (49%), grey matter (39%) and cerebral spinal fluid (CSF) (4%) (Henkelman et al. 1993).

Modeling Continuous-Wave MT Sequences

At the start of a continuous-wave experiment the magnetisation of pool A and B are at equilibrium. However, soon after the start of the experiment an off-resonance RF pulse selectively saturates pool B causing its magnetisation to be disturbed. The system then relaxes back to its equilibrium state through magnetisation transfer between pool B and A via chemical exchange and cross-relaxation (dipolar coupling) (Forsen and Hoffman 1963) (Figure 2.5).

In steady state conditions pools A and B are described by pseudo-first-order rate constants RM_0^A (exchange between B to A) and RM_0^B (exchange between A to B).

This chemical exchange can be modeled by adding it to the Bloch equations (Henkelman et al. 1993):

$$\frac{dM_z^A}{dt} = R_a(M_o^A - M_z^A) - RM_o^B M_z^A + RM_o^A M_z^B + \omega_1 M_y^A \tag{2.10}$$

$$\frac{dM_z^B}{dt} = R_B(M_o^B - M_z^B) - RM_o^A M_z^B + RM_o^B M_z^A + \omega_1 M_y^B \tag{2.11}$$

$$\frac{dM_x^{A,B}}{dt} = -\frac{M_x^{A,B}}{T_{2A,B}} - 2\pi\Delta M_y^{A,B} \tag{2.12}$$

$$\frac{dM_y^{A,B}}{dt} = -\frac{M_y^{A,B}}{T_{2A,B}} - 2\pi\Delta M_x^{A,B} - \omega_1 M_z^{A,B} \tag{2.13}$$

where the magnetisation for pools A and B are separated into x, y and z spatial components ($M_{x,y,z}^{A,B}$) and M_0^A and M_0^B the magnetisation of each pool at equilibrium. The angular frequency of precession induced by the off-resonance RF pulse is $\omega_1 = \gamma B_1$ and Δ is the off-resonance frequency of the RF pulse.

The Bloch equations for the macromolecular or semisolid pool is replaced by a single longitudinal component to better describe the behaviour of the macromolecular protons, where rate of saturation for the magnetisation is: (Morrison and Henkelman 1995):

$$R_{RFB} = \omega_1^2 g(2\pi\Delta T_2^B) \tag{2.14}$$

where g is the absorption lineshape of spins in the macromolecular pool and is a function of the macromolecular pool's transverse relaxation time T_2^b and Δ. The

macromolecular lineshape, g, in biological tissues is represented by a super-Lorentzian (Morrison and Henkelman 1995; Sled and Pike 2001):

$$R_{RFB}(\omega_1, \Delta) = \omega_1^2 \sqrt{2\pi} \left[T_2^B \int_0^1 \frac{1}{3u^2 - 1} \exp -2 \left(\frac{2\pi \Delta T_2^B}{3u^2 - 1} \right)^2 du \right] \tag{2.15}$$

Solving the above differential equations for the steady state condition the left hand sides of equations 2.10, 2.11, 2.12 and 2.13 are simply set to zero. This solution allows for the longitudinal magnetisation of the free pool, M_z^A, to be solved,

$$M_z^A = \frac{R_B \left[\frac{RM_0^B}{R_A} \right] + R_{RFB} + R + R_B}{\left[\frac{RM_0^B}{R_A} \right] (R_B + R_{RFB}) + \left(1 + \left(\frac{\omega_1}{2\pi\Delta} \right)^2 \left[\frac{1}{R_A T_{2A}} \right] \right) (R_B + R_{RFB} + R)} \tag{2.16}$$

where R_{RFB} is the rate of loss of macromolecular longitudinal magnetisation due to off-resonance irradiation of amplitude ω_1 and offset frequency Δ.

An experimental representation of the CW experiment when either magnetisation transfer occurs or not can be seen in Figure 2.8. Within this plot the upper curve, dashed line, demonstrates the relative magnetisation measured when no exchange between water proton spins occurs. Note at offset frequency values below 10kHz there is saturation of water, known as direct effect (M_{dir}). If it were possible to selectively saturate the macromolecular pool directly, then without exchange, the dotted line would be observed. The macromolecules broad lineshape is demonstrated by the fact they can be saturated out to 35 kHz. The sigmoidal solid line is the saturation of the liquid pool exchanging with the macromolecular pool. The shaded region is the magnetisation transfer (M_{MT}) between the two pools.

Equation 2.16 is a solution for the CW technique, however this technique is impractical for experiments using conventional scanners due to long scan times and high specific absorption (SAR) values. Instead, pulsed RF sequences consisting of multiple short-shaped Gaussian off-resonance pulses are used. Within the pulsed RF sequence

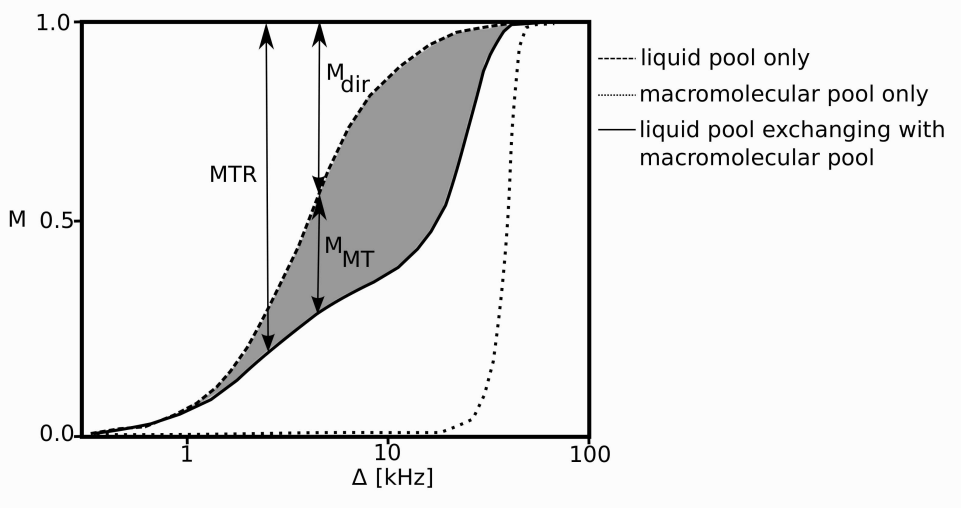

Figure 2.8: A schematic of longitudinal magnetization of the liquid and macromolecular pool. The dashed line represents saturation due to the direct effect (M_{dir}), the dotted line saturation for the macromolecular pool only and the solid line is the saturation of the liquid pool exchanging with the macromolecular pool. The shaded region is the saturation from magnetisation transfer (Henkelman et al. 2001).

the assumptions in equation 2.16 are violated since the system is no longer in steady-state since the T_1 relaxation times of both pools are longer than the time-varying RF pulses amplitudes (Pool A $\sim 700 - 1200$ ms and Pool B $\sim 300 - 600$ms at 1.5 T).

Modeling Pulsed MT Sequences

Unlike in the steady-state condition where all four time derivatives are equal to zero the pulsed MT experiment requires the Bloch equations 2.10, 2.11, 2.12 and 2.13 to be solved in the time domain, due to their short RF pulses and time-varying pulse amplitudes (Graham and Henkelman 1997). The following differential matrix equation represents the pulsed MT sequence (Sled and Pike 2000b):

$$\frac{d\mathbf{M}(t)}{dt} = \Lambda(t)\mathbf{M}(t) + \beta M_0 \tag{2.17}$$

where $\mathbf{M}$ is a four dimensional magnetisation vector $(M_X^A, M_Y^A, M_Z^A, M_Z^B)$ and M_0 is the equilibrium value of each magnetisation component. The matrices Λ and β are

made up of the coefficients from Henkelman's equations 2.10, 2.11, 2.12 and 2.13. As noted before for pulse MT experiment Λ is time-varying, thus no general solution exists.

Several studies have been presented as a simplification of the solution for the time varying modified Bloch equations. Sled and Pike (2000b) proposed a model that approximates the effect of a MT pulse on the free pool by rapid saturation of longitudinal magnetisation and on the macromolecular pool by a rectangular pulse with the same average power. Later, Ramani et al. (2002) proposed a simpler model in which they introduced a "continuous wave power equivalent" (CWPE) for the short pulsed MT sequences. In the same year, Yarnykh (2002) introduced a MT technique where the direct saturation on the liquid pool is neglected and the RF pulse is approximated by equal-power rectangular pulses. Ramani's model will be described in the section that follows since it is the model used throughout this thesis.

Ramani's Approximation

Ramani's approximation for the pulsed MT sequence by means of a CW equivalent average power approximates the amplitude $\omega_1(t)$ by a constant, CWPE. The constant for the saturation pulse amplitude ω_{1CWPE} is defined as (Ramani et al. 2002):

$$\omega_{1CWPE} = \gamma B_{1CWPE} = \sqrt{\frac{\int_0^\tau \omega_1^2(t)dt}{TR}} \tag{2.18}$$

where TR is the repetition time for the pulsed SPGR MT sequence and the integral on the right-hand side is evaluated for the power deposited by the RF pulse for both CW and pulsed MT per TR (for a 3D acquisition). Equation 2.18 can be simplified to be equal to the mean square saturating field averaged over a time TR' (P_{SAT}) (Ramani et al. 2002):

$$\omega_{1CWPE} = \gamma\sqrt{P_{SAT}} \tag{2.19}$$

where γ is the gyromagnetic ratio of the proton. The mean square saturating field (P_{SAT}) is a function of the shape, duration (τ_{SAT}) and maximum amplitude (B_{SAT}) of the applied RF pulse:

$$P_{SAT} = p_2 B_{SAT}^2 \frac{\tau_{SAT}}{TR'} \tag{2.20}$$

where p_2 is the ratio of the mean amplitude of the saturation pulse squared over a rectangular pulse of the same height. The applied saturating RF pulse results in an excitation flip angle θ_{SAT} that is used during MR acquisition and is a function of its shape, duration (τ_{SAT}) and maximum amplitude (B_{SAT}):

$$\theta_{SAT} = \frac{180}{\pi} \gamma p_1 B_{1SAT} \tau_{SAT} \tag{2.21}$$

where p_1 it the ratio of the mean amplitude of saturation pulse to that of a rectangular pulse of the same amplitude. Knowing the values of θ_{SAT} allows B_{SAT} to be calculated from equation 2.21. Furthermore, substituting equation 2.20 into equation 2.19 allows one to calculate ω_{1CWPE}.

Instead of normalizing Henkelman's equation 2.16 (divide by M_0^A) as done by other groups (Henkelman et al. 1993; Portnoy and Stanisz 2007) Ramani keeps M_0^a on both sides of the equation to maintain dimensionality. This allows the MT-weighted signal from the liquid pool, $S(\omega_1, \Delta)$, to be measured (Ramani et al. 2002):

$$\begin{aligned} S(\omega_1, \Delta) &= gM_Z^A \\ &= gM_o^A \cdot \frac{\left(R_B\left[\frac{RM_0^B f}{R_A}\right] + R_{RFB}(\omega,\Delta) + R_B + RM_o^A\right)}{\left[\frac{RM_0^B f}{R_A}\right](R_B + R_{RFB}(\omega,\Delta)) + \left(1+\left(\frac{\omega_1}{2\pi\Delta}\right)^2\left[\frac{1}{R_A T_{2A}}\right]\right)(R_B + R_{RFB}(\omega,\Delta) + RM_0^A)} \end{aligned} \tag{2.22}$$

where g is a scaling factor (function of scanner dependent parameters, such as the gain of the RF amplifier) and the macromolecular proton fraction (MMPF) defined as:

$$MMPF = \frac{M_o^B}{M_o^B + M_o^A} \tag{2.23}$$

where M_0^a and M_0^b are fully relaxed magnetisation values of the free water and macromolecular pools, respectively. Solving the non-linear equation 2.22 requires at least six independent measurements of ω_1 and Δ since there are six qMT parameters to solve for: $RM_0^A, \frac{MMPF}{R_A(1-MMPF)}, R_B, \frac{1}{R_A T_2^A}, T_2^B, gM_0^A$ (Ramani et al. 2002). Furthermore, MMPF can be solved by measuring R_A separately and calculating using the equation below (Henkelman et al. 1993):

$$R_A = R_{Aobs} - \frac{RM_0^A f(R_B - R_{Aobs})}{R_B - R_{Aobs} + RM_0^A} \tag{2.24}$$

qMT parameters such as MMPF have been shown to be sensitive to the loss of myelin, thus making MMPF a unique measure for WM characterisation (Sled and Pike 2001; Odrobina et al. 2005). However, there are limitations to the accuracy of Ramani's approximation of the MT-weighted signal. Ramani's model is only valid when the decrease in T_1-weighting is negligible since it does not model the effects of excitation pulses and TR. Furthermore, Ramani's model assumes the MT pulse is applied continuously making the duty cycle a factor in the accuracy of its fitted parameters. However, it has been shown that if the duty cycle is at least 50% it will not affect the accuracy of the fit (typical for many *in vivo* experiments) (Cercignani and Barker 2008).

2.1.3 Multicomponent Reloxometry

Multicomponent relaxometry of T_2 is a method that obtains contrast by probing the inhomogenous environment of a sample. If a sample was homogeneous and can be defined as a single compartment the T_2 relaxation would be monoexponential. However, we know the brain is heterogeneous and different measurable T_2 times correspond to unique water environments due to their distinct T_2s. Within the central nervous system there are four distinct water environments: the jelly-roll like structure

of myelin provides a perfect environment for the magnetisation exchange between the trapped water with its lipoproteins (short T_2 time), the cerebral spinal fluid (CSF) which is similar to pure water, intracellular and extracellular water. The last two water environments are often indistinguishable by the majority of T_2 MRI techniques and thus are grouped into one water peak. The remaining three T_2 components give rise to water peaks within a healthy individual of: 10-50 ms for the myelin bilayers, 70-90 ms for the cytoplasm (includes intra and extracellular) and $>$ 2s for the CSF (MacKay et al. 1994; MacKay et al. 2006).

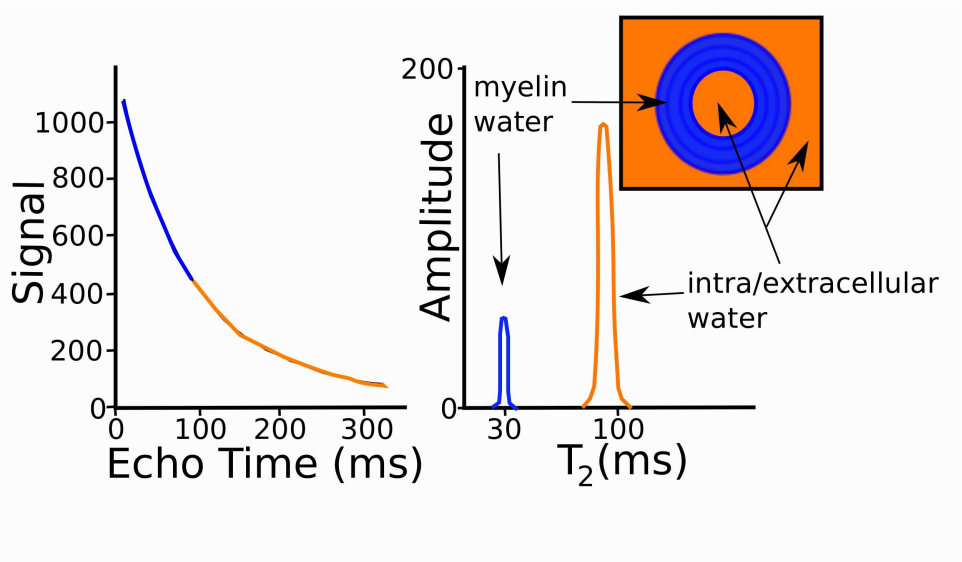

Figure 2.9: Representation of a multi-echo T_2 sequence with two separate water peaks: myelin and intra/extracellular water.

The first multicomponent T_2 experiment used a two-echo Carr-Purcell-Meiboom-Gill (CPMG) pulse sequence to separate T_2 times and amplitudes into the two compartments (Armspach et al. 1991). The year following the introduction of CMPG, a single-slice multi-echo pulse sequence known as the 'Poon-Henkelman' sequence was introduced to include additional crusher gradients with alternating polarity on either side of the refocusing pulse to suppress the B_1 inhomogeneity and signal from outside the slice (Poon and Henkelman 1992). Shortly afterwards, the CPMG sequence was

further expanded to 32-echos leading to a better characterisation of the T_2 decay and the quantification of multiple water environments within a sample or tissue (Whittall et al. 1997). This allowed for three parameters to be estimated from T_2 distributions: area fraction, geometric mean T_2 time and geometric T_2 width ratio. The water fractions are calculated by integrating the peaks between T_2min and T_2max and dividing it by the total area of the T_2 distribution (Figure 2.9). In the WM, the average MWF is around 11.3% (the highest being in the corpus callosum at 13%). However, note that the MWF is above zero within GM at around 3.1% (Whittall et al. 1997).

There are a number issues and limitations with the CPMG pulse sequence. The main disadvantage is that it can only acquire data from a single slice due to magnetization transfer effects from off-resonance excitations in adjacent slices. Also, at higher fields it has been hypothesised that B_1 increases the peak water width within the GM when compared to WM due to the higher concentration of iron (Oh et al. 2006).

Since the initial implementation of CPMG a number of developments and alternative sequences have been introduced. A ten minute spiral acquisition that includes a T_2-prep, 12 non-linearly spaced echoes, RF cycling scheme for 16 slices was introduced and shown to have no MT effects or T_1 recovery artefacts (Oh et al. 2006). In the same year a three dimensional Poon-Henkelman sequence was introduced which included an additional phase-encoding gradient in G_z for each echo, a 90° slab-selective pulse and non-alternating-descending z-axis crusher gradient pulse (Mädler and MacKay 2006). Another method requiring prior assumptions of the number of compartments and their T_2 times is the linear combination of TEs which dissociated myelin water from the total water (Jones et al. 2004; Vidarsson et al. 2005). The three-echo linear combination technique with echo times and weights chosen to maximise intracellular (IE) water and cerebrospinal fluid (CSF) was initially introduced for six slices with a five minute scan time (Jones et al. 2004; Vidarsson et al. 2005), which was then

later applied to the whole brain taking a total of fifteen minutes of scan time (Bells et al. 2007). More recently, using different methodology Deoni *et al.* (2008, 2008) combined spoiled gradient recalled echo (SPGR) and fully-balanced steady-state free precession (bSSFP) acquisitions to acquire full brain coverage with high resolution in under ten minutes. T_1 and T_2 water fractions for both myelin and intracellular water are determined in this technique known as multi-component driven equilibrium single pulse observation of T_1 and T_2 (mcDESPOT). This technique has the advantage over conventional 2D quantitative T_2 techniques due to its higher signal to noise efficiency, shorter acquisition times and a larger contribution of short T_2 species to the measured signal since both TE and TR are held constant (Deoni et al. 2003). The quantitative T_2 technique used throughout this thesis is mcDESPOT and will be described in the sections below.

DESPOT

Before the introduction of mcDESPOT quantitative measures of T_1 (driven-equilibrium single-pulse observation of T_1 - DESPOT1) and T_2 (DESPOT2) were introduced. DESPOT1 was introduced to overcome the shortcomings of conventional T_1 sequences, inversion-recovery (IR) and saturation-recovery (SR), with either their low SNR or resolution and long scan times. DESPOT1 is a variable flip angle (FA) method using spoiled gradient echo (SPGR) sequence that was originally introduced in 1974 (Christensen et al. 1974) in NMR and later explored by other researchers (Homer and Beevers 1985; Wang et al. 1987; Fram et al. 1987; Homer and Roberts 1990; Homer and Roberts 1987; Deoni et al. 2003) to estimate T_1 with the same accuracy as IR and SR methods. DESPOT2 was a T_2 sequence proposed to use the highly efficient imaging method of steady-sate free precession (SSFP) which was originally introduced in 1958 (Carr 1958).

DESPOT1 acquires multiple spoiled-GRE images at various flip angles altering the amount of T_1 weighting allowing T_1 to be fit for every voxel. This technique uses spoiling to influence the residual magnetisation so it does not contribute to the total signal, thus establishing a spoiled steady state and a relatively pure T_1 image. The total signal from each of the different flip angles will produce a signal curve that depends on T_1, which can easily be linearized to determine the T_1 (Wang et al. 1987; Deoni et al. 2003). DESPOT1 determines T_1 contrast simply by acquiring a set of two SPGR images with varying flip angles (α) at a constant TR and measuring the SPGR signal (S_{SPGR}). Plotting $S_{SPGR}/\sin\alpha$ against $SI_{SPGR}/\tan\alpha$ for the linear equation allows for the calculation of T_1(Deoni et al. 2003):

$$\frac{S_{SPGR}}{\sin(\alpha)} = E_1\frac{S_{SPGR}}{\tan\alpha} + M_0(1 - E_1) \tag{2.25}$$

where M_0 is a factor proportional to the equilibrium longitudinal magnetization and $E_1 = \exp -\frac{TR}{T_1}$. A T_1 map is determined from calculating the slope of the estimated line for each voxel:

$$T_1 = -\frac{TR}{\ln slope} \tag{2.26}$$

DESPOT2 acquires multiple fully balanced steady-state free precession (bSSFP) images at various flip angles at a constant TR (TR $\leq T_2 \leq T_1$), thus altering the amount of T_2 and T_1 weighting. By acquiring both spoiled-GRE in DESPOT1 and bSSFP images at several flip angles T_1 and T_2 can be estimated. The DESPOT2 sequence makes use of both longitudinal and transverse magnetisation being in a steady-state. The only source of phase accumulation after each TR is from residual transverse magnetisation. Thus, the signal (S_{SSFP}) for each of the different flip angles (α) will produce a signal curve that depends on both T_1 and T_2 relaxation times of the tissue as well as TR and M_0. DESPOT2 determines T_2 from a series of images with very short TR (less than 10 ms) and alternating the flip angle (α) by linearizing S_{SSFP}

within every voxel (Deoni et al. 2003). Plotting $S_{SSFP}/\sin\alpha$ against $S_{SSFP}/\tan\alpha$ for the linear equation below allows us to calculate T_2 when T_1 is already known:

$$\frac{S_{SSFP}}{\sin\alpha} = \frac{E_1 - E_2}{1 - E_1E_2}\frac{S_{SSFP}}{\tan\alpha} + \frac{M_0(1 - E_1)}{1 - E_1E_2} \tag{2.27}$$

where $E_2 = \exp -TR/T_2$. The T2 can be determined from the slope $((E_1 - E_2)/(1 - E_1E_2))$ and intercept $(M_0(1 - E_1)/(1 - E_1E_2))$

$$T_2 = -\frac{TR}{\ln\frac{slope - E_1}{slope \times E_1 - 1}} \tag{2.28}$$

The ability to linearize the signal equations of SPGR and SSFP sequences allows T_1 and T_2 to be rapidly acquired since only two flip angles are required. Furthermore, the flip angles are optimised to increase the accuracy and precession of T_1 and T_2 as described in (Deoni et al. 2004).

Challenges

The flexibility of steady-state sequences to harness different tissue properties also causes challenges if one is not cautious during quantification. It has been shown that variable flip angle bSSFP acquisitions are sensitive to MT effects (Crooijmans et al. 2011; Weber et al. 2009; Gloor et al. 2008). Other important biological confounds in the measurement of bSSFP include water diffusion (Bieri and Scheffler 2007) and exchange between different T_2 pools (Deoni et al. 2008). The last confound is exploited in the technique multi-component DESPOT (mcDESPOT) and is discussed in more detail in the next section.

Steady-state sequences are affected by a number of systematic variations listed here. Firstly, flip angle, which can arise from either B_1 inhomogeneity or slice profile errors (Deoni et al. 2005). Secondly, B_0 inhomogeneity (Deoni 2009) which produces the artefact know as 'banding' and is a result of the transverse magnetisation acquiring

a net phase shift (Deoni et al. 2004) in areas of discontinuous magnetic susceptibility, such as the sinuses.

To reduce B_1 inhomogeneities one can use an optimised RF pulse and a 3D acquisition (Deoni et al. 2003). To further reduce B_1 inhomogeneities affecting quantitative values a B_1 field map is required. In DESPOT1 a B_1 field map is acquired by combining SPGR images with an inversion-recovery(IR)-SPGR image to calibrate the flip angle (Wang et al. 2006; Deoni 2007).

A number of solutions have been introduced to reduce the banding artefact within bSSFP acquisitions such as: minimise TR (Deoni et al. 2005), combine images with altered RF phases by shifting the bands (Vasanawala et al. 2000) or/and RF pulse phase-cycling SSFP images (Deoni et al. 2004). Combining phase-cycling with a calibrated phase-precession map (B_0 map) for bSSFP images and calculating the B_1 maps reduces the artefacts within the DESPOT technique (Deoni 2009), allowing for a better characterisation of the confound within the bSSFP model caused by multiple T_2 pools as applied in mcDESPOT.

mcDESPOT

Combining high resolution DESPOT1 (SPGR) and DESPOT2 (bSSFP) 3D sequences while incorporating B_0 and B_1 maps allows for rapid whole brain images with reduced inhomogeneity and partial volume effects. Within the brain there are two or more separable exchanging species that can be seen using these two SPGR and bSSFP techniques (Deoni et al. 2007; Deoni et al. 2008). The two-component system is used to describe the mcDESPOT signal which is a linear summation of the signal from each of the species when TE and TR are much less than T_2 (Deoni et al. 2008). In this section a brief introduction of the two-component SPGR and bSSFP signal model will be provided, for a more detailed explanations see (Deoni et al. 2007). Assuming a two-compartment tissue model in chemical equilibrium the 'steady-state'

sequences can be separated into two exchanging species: fast (F) and slow (S) (Deoni et al. 2007). The SPGR magnetisation (M^{SS}_{SPGR}) is separated into the two exchanging species as described by:

$$M^{SS}_{SPGR} = \frac{\rho(I - e^{A_{SPGR}TR})\sin\alpha}{1 - e^{A_{SPGR}TR}\cos\alpha} \tag{2.29}$$

where α is the flip angle, I is a 2x2 identity matrix, ρ is a vector representing the equilibrium longitudinal magnetisation for the fast (f_F) and slow (f_S) species volume fractions,

$$\rho = \begin{bmatrix} f_S \\ f_F \end{bmatrix} \tag{2.30}$$

and A represents the matrix of the exchange rates between the two species, K_{FS} and K_{SF}, and their T_1 values,

$$A_{SPGR} = \begin{bmatrix} -\frac{1}{T_{1,F}} - K_{FS} & K_{SF} \\ K_{FS} & -\frac{1}{T_{1,S}} - K_{SF} \end{bmatrix} \tag{2.31}$$

The exchange rates are the reciprocals of the mean residence times τ_F and τ_S. In the steady-state condition the exchange rates and volume factions for each pool can be coupled, $f_F K_{FS} = f_S K_{SF}$. Extending the SPGR result to include the bSSFP magnetisation (M^{SS}_{bSSFP}):

$$M^{SS}_{bSSFP} = \frac{(e^{A_{bSSFP}TR} - I)A^{-1}_{bSSFP}C}{I - e^{A_{bSSFP}TR}R(\alpha)} \tag{2.32}$$

where α is the flip angle, I is a 6x6 identity matrix, $R(\alpha)$ is a rotation matrix representing the RF pulse (Deoni et al. 2007) and M^{SS}_{bSSFP} is a vector containing the x,y and z magnetization of the fast (F) and slow (S) species:

$$M^{SS}_{bSSFP} = [M^{SS}_{x,F} M^{SS}_{x,S} M^{SS}_{y,F} M^{SS}_{y,S} M^{SS}_{z,F} M^{SS}_{z,S}]^T \tag{2.33}$$

and C is a vector that relates the equilibrium longitudinal magnetisation and volume fractions for each species:

$$C = \rho \begin{bmatrix} 0 & 0 & 0 & 0 & \frac{f_F}{T_{1,F}} & \frac{f_S}{T_{1,S}} \end{bmatrix} \tag{2.34}$$

Furthermore, since bSSFP includes both T_1 and T_2 the A_{bSSFP} is a matrix that expands upon A_{SPGR} to include T_2 and off-resonance:

$$A_{bSSFP} = \begin{bmatrix} -\frac{1}{T_{2,F}} - K_{FS} & K_{SF} & \Delta\omega_F & 0 & 0 & 0 \\ K_{FS} & -\frac{1}{T_{2,S}} - K_{SF} & 0 & \Delta\omega_S & 0 & 0 \\ -\Delta\omega_F & 0 & -\frac{1}{T_{2,F}} - K_{FS} & K_{SF} & 0 & 0 \\ 0 & -\Delta\omega_S & K_{FS} & -\frac{1}{T_{2,S}} - K_{SF} & 0 & 0 \\ 0 & 0 & 0 & 0 & -\frac{1}{T_{1,F}} - K_{FS} & K_{SF} \\ 0 & 0 & 0 & 0 & K_{FS} & -\frac{1}{T_{1,S}} - K_{SF} \end{bmatrix} \tag{2.35}$$

The measured magnetisation from the bSSFP sequence is the total transverse magnetisation, represented by the summation of the components $M^{SS}_{x,F} + M^{SS}_{x,S} + iM^{SS}_{y,F} + iM^{SS}_{y,S}$ (Deoni et al. 2008). Within this mcDESPOT model the fast- and slow-relaxing species represent myelin and intra- and extracellular water compartments, respectively. The commonly used MWF is represented by f_F, where in this case it is independent of exchange between myelin water and IE water because the exchange been the two is modeled by mcDESPOT. The myelin residence time is τ_F, which may be linked to myelin thickness (Kolind and Deoni 2011). For healthy controls myelin water fraction from mcDESPOT range from 4% to 25% in WM and are $< 10\%$ in GM structures (Deoni et al. 2008).

Summary

Within the last decade white matter microstructural imaging using MRI has come a long way. Diffusion MRI is sensitive to microstructural changes, but not specific to either myelin or axon diameter changes. However, DTI provides us with estimates of diffusion anisotropy and fibre orientation. On the other hand, both magnetisation

transfer imaging, myelin water imaging and restricted diffusion imaging provides us with more specific estimates of myelin and axon diameter. The comparison of all three white matter microstructural techniques are discussed in detail in Chapter 4.

Chapter 3

Measurement uncertainties in qMT-derived parameters

3.1 Introduction

Magnetisation transfer (MT) imaging is a magnetic resonance (MR) imaging technique that uniquely provides a measure of the relative density of macromolecules within tissue by harnessing information on the exchange between water protons and macromolecules such as protein, lipids and cellular membranes, which are invisible to conventional MR scans owing to their very short T_2 decay times ($\sim$10 μs)(Wolff and Balaban 1989). MT models typically split the brain into two different compartments by grouping spins into a free or liquid pool consisting of water protons with a long T_2 (T_2 >10 ms) and a restricted or semisolid (macromolecular) pool consisting of protons within lipids with very short T_2s (T_2 <100 us).

Routinely quantitative MT (qMT) experiments achieve their contrast by applying a series of off-resonance radio-frequency (RF) pulses (of amplitude (ω_1) and offset frequencies (Δ $\sim$1000 Hz away from the water peak)) that selectively saturates the macromolecular pool. The resulting decrease in the signal measured from the free pool is attributed to the transfer of magnetization from saturated macromolecules to free water protons occurring through cross-relaxation or chemical exchange (Ceckler et al. 1991; Kucharczyk et al. 1994). The rapid exchange of magnetization between the two pools causes the free-water signal to attenuate after the off-resonance pulse

is applied. The amount of attenuation depends on both experimental parameters, such as RF pulse parameters (amplitude (B), duration (τ), shape (e.g. Gaussian), duty cycle, frequency offset), and biological parameters, such as the concentration of macromolecules in the sample, exchange rate between the two pools and longitudinal and transverse relaxation times of each pool.

The macromolecular proton fraction (MMPF), is a measure which aims to influence out experimental factors and provide a quantitative measure of the number of trapped protons in the macromolecular pool (such as myelin), relative to the total number of protons present (Ramani et al. 2002). Importantly, the MMPF has been shown to related to myelin lipid content measured using the Luxol fast blue stain within both postmortem fixed tissue (Schmierer et al. 2007) and fresh tissue (Schmierer et al. 2008). Not only does MMPF provide a unique contrast, but it also has been demonstrated to be a valid biomaker for pathological white matter (WM) syndromes, such as; inflammation, demyelination and axonal loss (Stanisz et al. 1999; Pike et al. 2000; Siger-Zajdel and Selmaj 2001; Sled and Pike 2001; Stanisz et al. 2004; Schmierer et al. 2007).

With the expanding use of qMT parameters, such as MMPF, it is critical to characterize their associated uncertainties, and to find the experimental factors that contribute the most to these uncertainties, so that the precision of qMT parameters can be maximized.

This study uses a bootstrapping approach to examine the impact of a number of pre-processing steps in the qMT pipeline on the precision of derived parameters, aiming to finding the optimal pipeline for qMT.

The precision and accuracy of the fitted parameter estimates within qMT models rely partly on the choice of sampling points: ω_1 and Δ. A recent study explored optimal MT configurations of sample points using Cramer-Rao lower-bound optimization

to minimize the variance with respect to the sample points (Cercignani and Alexander 2006). Here, we used the optimized sampling scheme derived from Cercignani and Alexander's study. However, in addition to the sampling scheme, there are other factors that affect the precision and accuracy of the qMT parameters. For example, radio-frequency non-uniformity (B_1) and static field inhomogeneity (B_0) (Barker et al. 1998; Stanisz et al. 1999; Sled and Pike 2001; Lewis and Fox 2004; Stanisz et al. 2004) if uncorrected can potentially change the estimates of qMT results between 5-20% (5% for MMPF, 20% for T_2^B)(Sled and Pike 2000a). The static magnetic field (B_0) and the RF magnetic field (B_1) inhomogeneites can be estimated by separate pulse sequences and used to correct systematic errors caused by both inhomogeneities (Sled and Pike 2000a; Ropele et al. 2005).

A qMT protocol therefore requires acquisition of a number of separate images including a number of MT points (i.e., different offset frequencies and amplitudes), a quantitative T_1 map, a B_1-map and a static field inhomogeneity map. All these steps contribute to the variation within the qMT model fits, and it is therefore desirable to fully explore the impact of varying attributes of the protocol, such as the methods used for B_0/B_1 correction, and qMT pulse sequences. Such an analysis will allow us to determine the best analysis pipeline that produces the smallest uncertainly in the measurements.

To fully characterize the variance in the qMT parameters, it is necessary to account for possible interactions between various sources of noise, such as physiological noise, scanner instability and susceptibility variations. However, deriving a complete analytical model that includes all of these variations is extremely challenging, and requires prior assumptions regarding the statistical distributions of the various sources of noise.

In this work, we adopt a different approach to quantify the uncertainties within the qMT pipeline and use wild bootstrapping (O'Gorman and Jones 2006; Zhu et al. 2008) as it does not require assumptions about noise distributions, and obtains such information from the data themselves. Bootstrapping is a nonparametric statistical method, which implicitly accounts for all sources of noise (including physiological and instrumental noise) and has previously been shown to be a powerful method for characterizing uncertainty in human imaging data, such as those from diffusion tensor imaging (DTI) (Pajevic and Basser 2003). The advantage of a model-based resampling technique, such as wild bootstrapping, over more conventional bootstrapping methods, is that there is no need to repeat the acquisition to determine uncertainties (Zhu et al. 2008).

Here, an optimized wild bootstrap method was used on *in vivo* human brain data to: (1) estimate regional distributions of qMT uncertainties in brain tissue, and (2) to assess the combined effects of different factors on the uncertainties within qMT estimates, identifying largest sources of variance, and therefore pointing towards an optimal qMT pipeline. The factors explored along the qMT-processing pipeline that may influence the uncertainty within qMT parameters were:

1. The B_1 inhomogeneity mapping / correction method

2. The B_0 inhomogeneity mapping / correction method

3. The choice of T_1 mapping method

4. Two different qMT slab profiles (axial or sagittal acquisition) to match either the 3D SPGR FA-T_1 pipeline (axial) or the mcDESPOT pipeline (sagittal).

3.2 Material and Methods

3.2.1 Participants

Three healthy right-handed participants (age= 24.3 ± 0.6, female = 2) were included in this study. Informed consent was obtained prior to scanning and the study was performed with ethics approval from the ethics review board at our institution.

3.2.2 Imaging acquisition

Quantitative Magnetization Transfer MRI (qMT)

Two different types of qMT protocols were used:

1. An optimized 3D MT-weighted fast spoiled gradient recalled-echo (SPGR) sequence (Cercignani et al. 2005) with the following parameters: axially orientated, TR/TE = 25.826/2.18 ms; Gaussian MT pulses, duration τ = 14.6 ms; Gaussian MT pulses duration = 14.7 ms ;FOV = 240 mm; acquisition matrix = 96x96x76; BW=±15.63Hz; FA = 5.

2. An optimized 3D MT-weighted fast spoiled gradient recalled-echo (SPGR) sequence (Cercignani et al. 2005) with the following parameters: sagittally orientated, TR/TE = 26.65/1.86 ms; Gaussian MT pulses, duration τ = 14.6 ms; FOV = 220 mm; acquisition matrix = 128x96x64; BW=±31.25 Hz; FA = 5.

For both qMT sequences the following off-resonance irradiation frequencies (Δ) and their corresponding saturation pulse amplitude (θ_{SAT}) for the 11 MT weighted images were optimized using Cramer-Rao lower bound optimization (Cercignani and Alexander 2006) are: Δ = [1000.0 Hz, 1000.0 Hz, 12062.0 Hz, 47185.0 Hz, 56363.0

Hz, 2751.0 Hz, 1000.0 Hz, 1000.0 Hz, 2768.0 Hz, 2791 Hz, 2887.0 Hz] and their corresponding θ_{SAT} = [332.0°, 333.0°, 628.0°, 628.0°, 332.0°, 628.0°, 628.0°, 628.0°, 628.0°, 628.0°, 628.0°].

Multi-component driven-equilibrium single-pulse observation (mcDESPOT)

The mcDESPOT protocol consists of a combination of sagittally oriented SPGR, balanced steady state free precession (bSSFP) and inversion-recovery prepared SPGR (IR-SPGR) sequences (Deoni et al. 2008; Deoni et al. 2008). All three were acquired with a FOV of 220 mm; 1.7 mm anterior-posterior x 1.7 mm left-right x 1.7 mm superior-inferior, with frequency encoding in the superior-inferior direction for a total mcDESPOT scan time of approximately 8 minutes. Additional sequence specific parameters were:

- SPGR: TE/TR = 2.1/4.7 ms; BW = ±25 kHz; flip angle (α) = [3°, 4°, 5°, 6°, 7°, 9°, 13°, 18°].
- bSSFP: TE/TR = 1.6/3.2 ms; BW = ±62.5; α = [10.6°, 14.1°, 18.5°, 23.8°, 29.1°, 35.3°, 45°, 60°] for both phase-cycling acquisitions of 0° and 180°.
- IR-SPGR: TE/TE = ms; BW = ±25; α = 5°; inversion time = 450 ms.

Additional Scans

In addition to the four main protocols, field maps and T_1 maps were also acquired. For B_1 maps, two fast-spin echo sequences with two different angles (N, 2N) were collected (TE = 1.6ms, TR = 3.2 ms, matrix = 128x128, FOV =300x300x500mm^3, scan time =1min each) for each flip angles, i.e. 90°, and 45° to enable the 'double angle' method (Cunningham et al. 2006) to be used. For B_0 maps two 3dgrass with different TE's were acquired (TE = 9ms and 7ms,respectively, TR= 20ms,matrix=128x128,FOV= 220x220x3mm^3)(Jezzard and Balaban 1995). For T1 maps three 3D SPGRs (TR =

6.9 ms, TE = 1.1 ms, matrix = 96x96, FOV = 240x240x 250 mm^3) were acquired with three different excitation flip angles (θ = 15°, 5°, 3°).

3.2.3 mcDESPOT Data Pre-Processing

SPGR and bSSFP images for each participant were linearly coregistered using an affine (12 degrees of freedom) technique based on mutual information to the first image in the sequence to correct for interscan and intrascan motion (Jenkinson and Smith 2001). SPGR and IR-SPGR images were used for DESPOT1 with High-speed Incorporation (DESPOT1-HIFI) of RF Field Inhomogeneities processing as described in (Deoni et al. 2006; Deoni 2007), resulting in B_1 field and T_1 maps. Furthermore, the B_1 field and T_1 maps were used in the calculation of B_0 field and T_2 maps using two phase-cycled bSSFP data using the DESPOT2 with full modeling (DESPOT2-FM) algorithm (Deoni et al. 2004).

3.2.4 qMT Data Pre-Processing

All eleven MT-weighted SPGR volumes for each participant were linearly coregistered to the MT-volume with the most contrast using an affine (12 degrees of freedom) technique based on mutual information to correct for interscan motion (Jenkinson and Smith 2001). The 11 MT-weighted SPGR images and T_{1obs} map were then modeled by Ramani's two pool pulsed MT approximation (Ramani et al. 2002). This model requires three additional maps/sequences:

1. A static field (B_0) map to correct for inhomogeneities within the static field.
2. An amplitude of radio-frequency (B_1) map to measure inhomogeneities within the radio-frequency pulses.

3. A map of the longitudinal relaxation rate, T_{1obs}, (derived from either the DESPOT or 3D SPGR 3 flip angle pipeline) - to provide an estimate of the longitudinal relaxation rate for the liquid pool (R_1^A) using the approximation proposed by Henkelman et al. (1993), to determine the macromolecular proton fraction, MMPF.

These three maps were all linearly co-registered using an affine (12 degrees of freedom) technique to the same MT-volume used in the previous registrations.

From a nonlinear least-squares fit of the model according to (Ramani et al. 2002), a total of six maps are produced: R_1^B, RM_0^A, gM_0^A, $MMPF/R_1^A(1-MMPF)$,$1/R_1^AT_2^A$ and T_2^B, where R_1^A and R_1^B are the reciprocals of the T_1 of the A and B pools, respectively, T_2^A and T_2^B are the transverse relaxation times of each pool, M_0^A the initial magnetization of the A pool and g the scanner gain.

3.2.5 Evaluating qMT fits

Initially, residuals (ε) between the observed signal and the signal predicted from the model fit were computed for each MT point within each protocol/pipeline, and the average residual deviation (RD) was evaluated according to:

$$\sigma = 100\% \sqrt{\sum_{i=1}^{N} \frac{(Fit_i - Data_i)^2}{N}} \tag{3.1}$$

Where N is the number of MT points (11 in this case).

3.2.6 Assessment of uncertainties within qMT

Uncertainties were derived using a wild bootstrap technique. For each of 1000 iterations the residuals, ϵ, were uniquely and randomly multiplied by either (+/-1)

Table 3.1: A list of the different pipelines used for bootstrap analysis. Each of the following pipelines were carried out for both the axial and sagittal acqusitions, thus the total number of different pipelines added to be 36 for each participant (axial = P1-19,sagittal = P19-P36). For each of the three maps used in MT modelling: T_1, B_0 and B_1, two different acquisitions were performed. T_1 maps: mcDESPOT technique and 3D SPGR 3 FA technique. B_1 maps: mcDESPOT technique and double angle method (DAM). B_0 maps: mcDESPOT analysis and gradient-echo (GRE) technique.

Protocol	T_1		B_0		B_1	
	mcDESPOT	SPGR 3-FA	mcDESPOT	DAM	mcDESPOT	GRE
P1/P19						
P2/P20						
P3/P21						
P4/P22						
P5/P23						
P6/P24						
P7/P25						
P8/P26						
P9/P27						
P10/P28						
P11/P29						
P12/P30						
P13/P31						
P14/P32						
P15/P33						
P16/P34						
P17/P35						
P18/P36						

and added to the original dataset to produce a resampled dataset represented in Figure (3.1) (Zhu et al. 2008). Bootstrap analysis was carried out using various combinations of field maps (B_0 and B_1), T_1 maps and qMT acquisitions (See Table 3.1). 1000 bootstrap iterations were performed for each of the 36 pipelines presented in Table 3.1 for all three participants, resulting in a total of 108,000 model fits for each volume (more if one includes every voxel). The total processing time would be approximately 4,503 days on a single procession, however on CUBRIC's cluster it was shorted to approximately 90 days (50 nodes with a total of 200 processing cores).

Prior to further analysis, all quantitative maps from the different pipelines were non-linearly registered to MNI space using a synthetic T_1-weighted image, calculated from the T_1-map resulting from the DESPOT pipeline using in house software (Deoni et al. 2006), as the source image. The registration used the approach of Rueckert et al. (1999) as implemented in FNIRT - a part of the FSL software package (Andersson et al. 2007a; Andersson et al. 2007b).

Following registration to MNI space, each T_1 map was segmented using the approach described by Ashburner and Friston (Ashburner and Friston 2000) to produce a white matter mask. The results of the bootstrap analysis were then used to compute standard errors and 95% confidence intervals (estimated from the 2.5^{th} and 97.5^{th} quantiles) for MMPF, T_1^B and RM_0^B within all pipelines.

To assist in visualization of the similarity / heterogeneity of results, the WM masked standard error maps for a given slice location were collapsed into a single vector, and a cross-correlation (CC) was performed. Each resulting CC-matrix was then re-ordered using the Fiedler vector of the normalized Laplacian formed from this CC-matrix (Barnard et al. 1993). This step was performed to assist in finding similarities (adjacent entries in the re-ordered CC-matrix) and dissimilarities (entries

that are far apart in the re-ordered CC-matrix) within uncertainties within the qMT pipelines.

3.2.7 Analysis of variance

The effect of different MT protocols on uncertainty was assessed using a two-way analysis of variance (ANOVA) to test which aspects of the MT protocol (36 levels) do/do not significantly affect uncertainties within the qMT parameters across three MNI slices (39,42 and 53) (significance level was set to $p < 0.05$). If the protocol was evaluated as a significant factor and the interaction between the protocol and slice was determined to be insignificant, a multi-comparisons (Turkey-Kramer, $p < 0.05$) test was used to determine which pairs were significantly different, and which were not.

3.3 Results

The results of the study are divided into two parts. The first section presents and describes the residuals within qMT measures across the participants, while the second section presents and describes the uncertainty of qMT parameters using a wild bootstrap analysis.

3.3.1 Evaluating qMT fits

Figure 3.2 shows the mean residuals across all pipelines: (A) qMT protocol axially oriented (B) qMT protocol sagittally oriented. Across all protocols MT-weighted volumes seven and eight consistently have large residuals (Figure 3.2 (A) and (B)). Results from $P8^{Ax}$ as an example, demonstrate that the residuals from volumes: one, two, seven and eight are more likely to be negative (Figure 1(C)). Interestingly, these

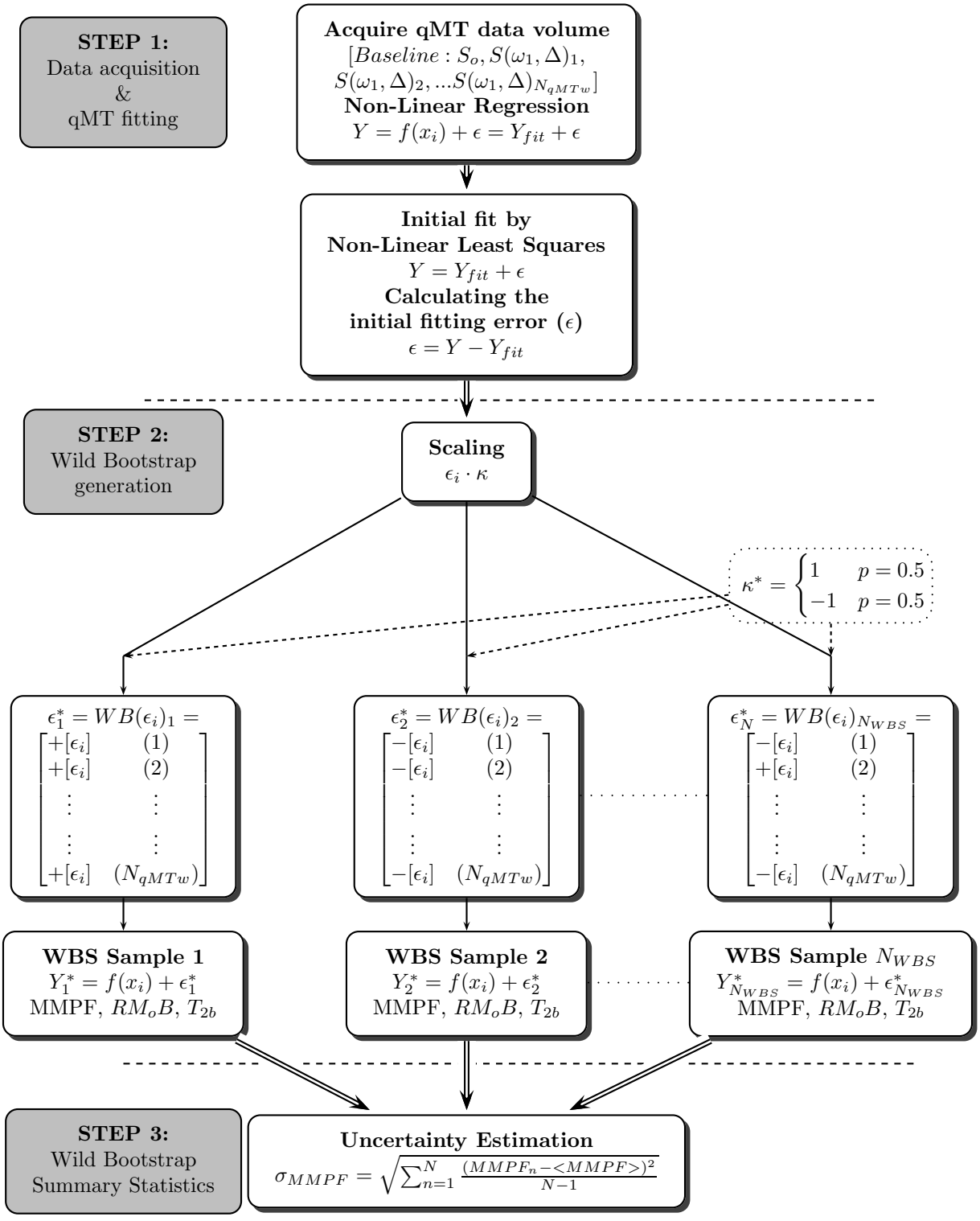

Figure 3.1: The wild bootstrap pipeline for qMT analysis. This figure illustrates the order of the different steps need to get to the desired result for the determination of uncertainty in qMT estimates. (Zhu et al. 2008)

Table 3.2: Summary of fitted MT Parameters for all 36 protocols: macromolecular proton fraction (MMPF), the semisolid pool fraction, RM_0^B, and the transverse relaxation time for the semisolid pool T_2^B and the average residual deviation (σ) for a given slice (MNI slice 42). Upper and lower limits of the 95% confidence interval from wild-bootstrap analysis are shown in parentheses. (P1-18 = axial acquistion, P19-P36 = sagital acquisiton)

Protocol	MMPF	RM_O^B (s^{-1})	T_2^B (μs)	σ(%)
P1	0.13 (0.067-0.21)	1.72 (0.86-3.22)	8.77 (5.89-11.93)	0.60
P2	0.11 (0.058-0.17)	1.78 (0.86-3.36)	8.78(5.89-11.96)	0.63
P3	0.13 (0.070-0.22)	1.76 (0.86-3.32)	8.75 (5.88-11.87)	0.60
P4	0.11 (0.058-0.17)	1.79 (0.86-3.36)	8.78 (5.89-11.95)	0.62
P5	0.16 (0.074-0.29)	2.03 (1.07-3.71)	8.72 (5.87-11.81)	0.57
P6	0.13 (0.071-0.20)	2.03 (1.07-3.72)	8.73 (5.87-11.84)	0.59
P7	0.16 (0.074-0.29)	2.03 (1.07-3.70)	8.71 (5.88-11.81)	0.56
P8	0.13 (0.071-0.20)	2.03 (1.07-3.68)	8.73 (5.88-11.82)	0.59
P9	0.083 (0.047-0.13)	1.79 (0.86-3.49)	8.76 (5.89-11.86)	0.61
P10	0.097 (0.054-0.15)	2.03 (1.06-3.73)	8.73 (5.88-11.85)	0.62
P11	0.13 (0.069-0.22)	1.77 (0.87-3.30)	8.75 (5.88-11.85)	0.59
P12	0.11 (0.058-0.17)	1.79 (0.87-3.37)	8.77 (5.89-11.93)	0.62
P13	0.083 (0.047-0.13)	1.79 (0.85-3.50)	8.78 (5.89-11.90)	0.63
P14	0.083 (0.047-0.13)	1.80 (0.85-3.53)	8.78 (5.89-11.90)	0.62
P15	0.16 (0.074-0.29)	2.04 (1.08-3.70)	8.72 (5.88-11.79)	0.56
P16	0.13(0.071-0.20)	2.04 (1.08-3.72)	8.71 (5.87-11.81)	0.58
P17	0.098(0.054-0.16)	2.08 (1.07-3.94)	8.82 (5.90-12.01)	0.61
P18	0.097 (0.054-0.15)	2.02 (1.05-3.74)	8.73 (5.87-11.88)	0.61
P19	0.12 (0.062-0.20)	1.91 (0.95-3.45)	8.51 (5.84-11.30)	0.82
P20	0.13 (0.061-0.21)	1.92 (0.95-3.48)	8.53 (5.84-11.35)	0.86
P21	0.14 (0.074-0.22)	1.91 (0.95-3.48)	8.51 (5.84-11.30)	0.80
P22	0.11 (0.061-0.17)	1.92 (1.16-3.74)	8.51 (5.84-11.34)	0.86
P23	0.16 (0.080-0.28)	2.18 (1.15-3.74)	8.49 (5.84-11.29)	0.73
P24	0.13 (0.074-0.20)	2.18 (1.16-3.74)	8.49 (5.83-11.32)	0.77
P25	0.16 (0.080-0.29)	2.19 (1.16-3.75)	8.47 (5.84-11.30)	0.73
P26	0.13 (0.074-0.20)	1.93 (0.95-3.58)	8.51 (5.83-11.30)	0.77
P27	0.085 (0.049-0.13)	2.18 (1.15-3.73)	8.50 (5.83-11.32)	0.84
P28	0.098 (0.058-0.15)	1.92 (0.95-3.48)	8.49 (5.82-11.30)	0.81
P29	0.14 (0.074-0.22)	1.93 (0.95-3.48)	8.51 (5.85-11.29)	0.79
P30	0.12 (0.061-0.19)	1.92 (0.94-3.58)	8.51 (5.84-11.33)	0.84
P31	0.085 (0.049-0.13)	1.92 (0.95-3.56)	8.50 (5.83-11.33)	0.87
P32	0.085 (0.049-0.13)	1.92 (0.95-3.56)	8.51 (5.83-11.33)	0.87
P33	0.16 (0.080-0.28)	2.19 (1.16-3.74)	8.49 (5.84-11.28)	0.73
P34	0.13 (0.074-0.20)	2.19 (1.16-3.72)	8.50 (5.84-11.29)	0.76
P35	0.099 (0.058-0.15)	2.17 (1.14-3.73)	8.49 (5.82-11.31)	0.88
P36	0.098 (0.058-0.15)	2.17 (1.15-3.72)	8.45 (5.82-11.31)	0.82

MT-weighted volumes all have the lowest offset frequency (Δ) of the eleven MT points, at 1000 Hz. High residuals in low off-set frequencies ($\sim$ 1000 Hz) were also seen by Portnoy and Stanisz (2007). MT-weighted volume five (with the highest off-set frequency 56,363 Hz) appears to be consistently overestimated across all pipelines. The residuals within the MT-weighted volumes six, nine, ten and eleven appear more heterogeneous (both positive and negative values throughout the image). All these MT-weighted volumes have an offset frequency around 2700 Hz. Agreement between the fitted curves and the measured data is good, with average residual deviations per slice, σ, across all axial protocols of 0.60% and across all sagittal acquisitions 0.81% (See Table 3.2 for details). These results suggest that the fitted MT parameters from the sagittal acquired MT-weighted data (P19-P36^{Sag}) produced higher residuals on average compared to the axially acquired MT-weighted data (P1-P18^{Ax}) ($T(18) = 27.63$ $p<0.001$, multiple comparison were corrected by using Bonferoni). It should be noted that the average SNR within the axially acquired MT-weighted data is 147.7 $\pm$ 27.2 and the sagittally acquired MT-weighted data is 135.4 $\pm$ 35.5, which is approximately 8% lower than the axial acquisition, and may well explain this difference in the residuals.

3.3.2 Assessment of uncertainties within qMT

The MT parameters derived from fits to the measured data are summarized in Table 3.2. Specifically, macromolecular proton fraction, MMPF, the semisolid pool fraction, RM_0^B, and the transverse relaxation times for the semisolid pool T_2^B, are shown. Uncertainties in the fitted parameters across the wild bootstraps are expressed in terms of 95% confidence intervals (showing the upper and lower limits since the interval was not always symmetric).

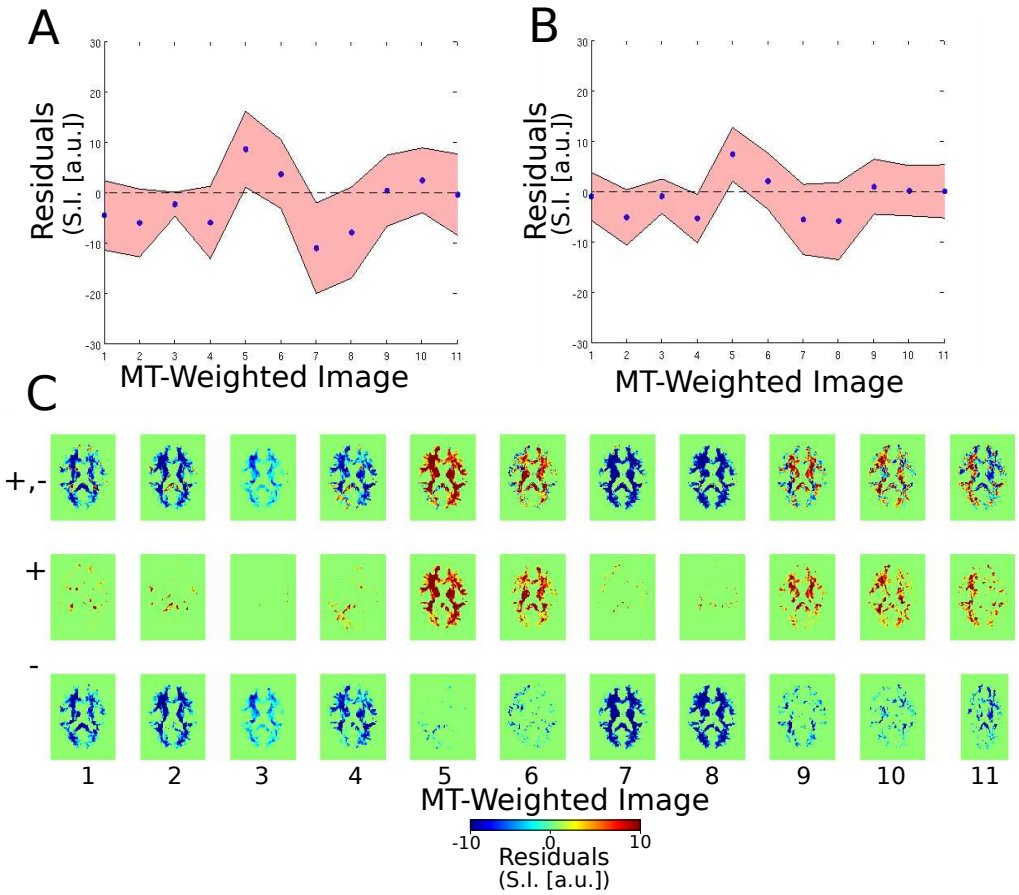

Figure 3.2: For a given slice, the mean residuals for all MT-weighted images within a WM mask (N=11). (A) Average residuals of the signal intensity for all qMT pipelines of the axially orientated acquisition where the standard deviation is represented by the shaded red area (B) Average residuals of the signal intensity for all qMT pipelines of the sagittaly orientated acquisition where the standard deviation is represented by the shaded red area (C) Residual results from data acquired with P8 are displayed as an example. Row 1 includes both positive and negative residuals, Row 2 positive residuals only and Row 3 negative residuals only.

Fitted parameters from all the protocols agree within stated uncertainties. The protocols tested for a given slice have similar estimated values of MMPF, RM_0^B, and T_2^B and uncertainty as indicated by the width of the 95% confidence interval. Measurement uncertainties in *in vivo* qMT data can be visualized in Figure 3.3, which shows example results from P16^{Ax} for one participant. Across all three slices the uncertainties within the ventricles is high indicating the lowest precision across the brain. For both MMPF and T_2^B the uncertainties within the ventricles are quite high demonstrating that for both these parameters, the MT model does not accurately model the signal in the ventricles or voxels that are mainly represented by free water. Importantly, large variation can be seen throughout a few WM regions within the uncertainty map of MMPF and RM_0^B especially in areas surrounding the ventricles, suggesting partial volume contamination from CSF and that the model is unable to account for this extra source of variance in the MMPF and RM_0^B parameters . It is of note, however, that for T_2^B this is not the case and uncertainties throughout the WM and GM are fairly homogeneous.

Overall, measurement uncertainties for MT parameters: RM_0^B, MMPF and T_2^B across all protocols and participants are shown in Figures 3.4-3.6, respectively. Results from $\langle\sigma(RM_0^B)\rangle$ show that the uncertainties across protocols are similar. It is of note, however, that the uncertainties within (RM_0^B) in the area of the genu of the corpus callosum (where macromolecular content is expected to be high) are slightly higher within all protocols especially the axially oriented acquisitions (P1-18^{Ax}). Uncertainty within $MMPF$ demonstrates a higher variability across protocols, where certain protocols stand out (P5^{Ax}, P7^{Ax}, P15^{Ax}, P23^{Sag}, P25^{Sag} and P33^{Sag}) as having high uncertainty within this parameter. These three protocols for both axial and sagittal acquisitions are unique in that they combine the 3 FA SPGR T_1 map with the mcDESPOT B_0 map. Within these protocols many of the voxels throughout the white matter mask have high uncertainties for $\langle\sigma(MMPF)\rangle$. Again, like the $\langle\sigma(RM_0^B)\rangle$ pa-

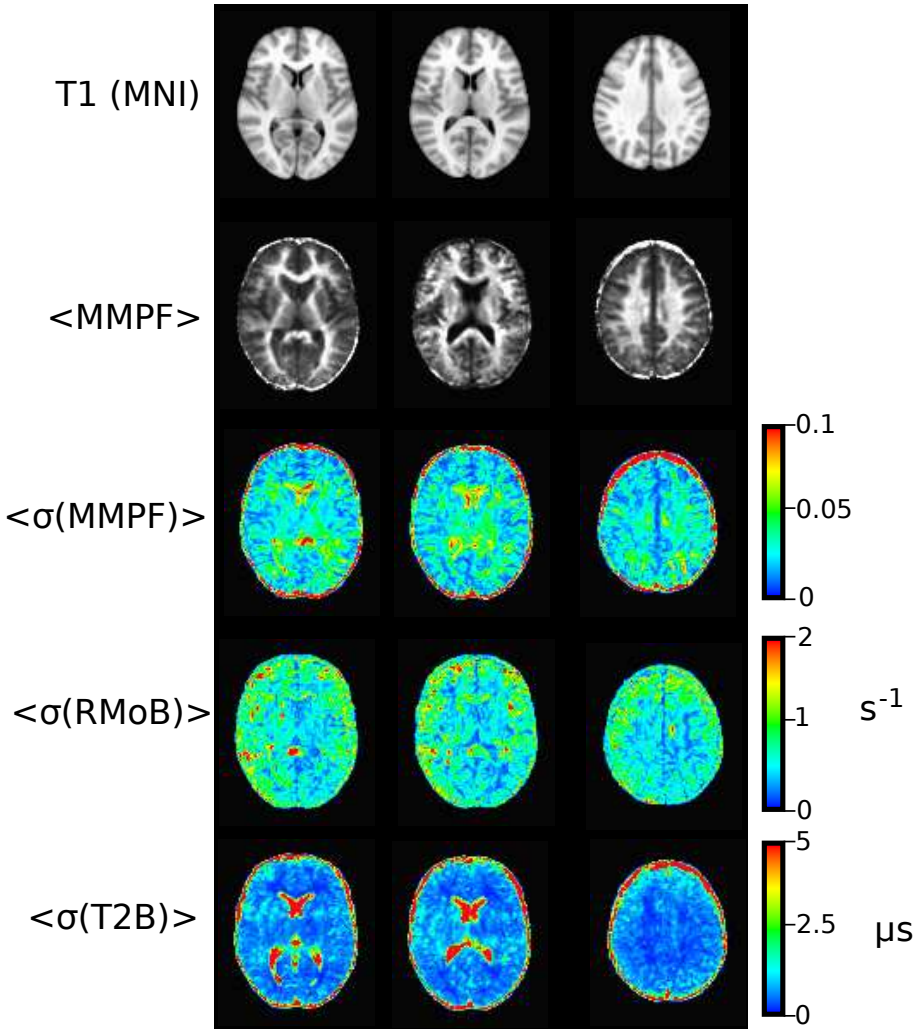

Figure 3.3: Wild bootstrap estimates for MMPF, RM_0^B and $T2^B$ from P16 data sets for one participant for three slices are shown (MNI=39,42,53). Row 1 is the anatomical T_1 template (MNI152) for each slice, Row 2 the average MMPF and Row 3-5 $\langle\sigma(MMPF)\rangle$ (dimensionless), $\langle\sigma(RM_0^B)\rangle$ (s^{-1}) and $\langle\sigma(T_2^B)\rangle$ μs, respectively. Overall, most of the WM regions in all three slices have good measurement precision indicated by blue/green colours in all three uncertainty maps. In addition, areas where there are increased uncertainties are within the grey matter and more specifically the ventricles.

rameter the uncertainties of $\langle\sigma(MMPF)\rangle$ within the genu is high across many of the protocols (P5-P8^{Ax}, P10^{Ax}, P15-P18^{Ax}, P23-P26^{Sag}, P28^{Sag}, P33-P36^{Sag}). All these protocols for both axial and sagittal acquisitions are unique in that they all use the 3 FA SPGR T_1 map. In the central regions of white matter the uncertainty maps of T_2^B demonstrate higher uncertainty within protocols P1-18^{Ax} (axially orientated), than the sagittally orientated protocols P19-P36^{Sag}.

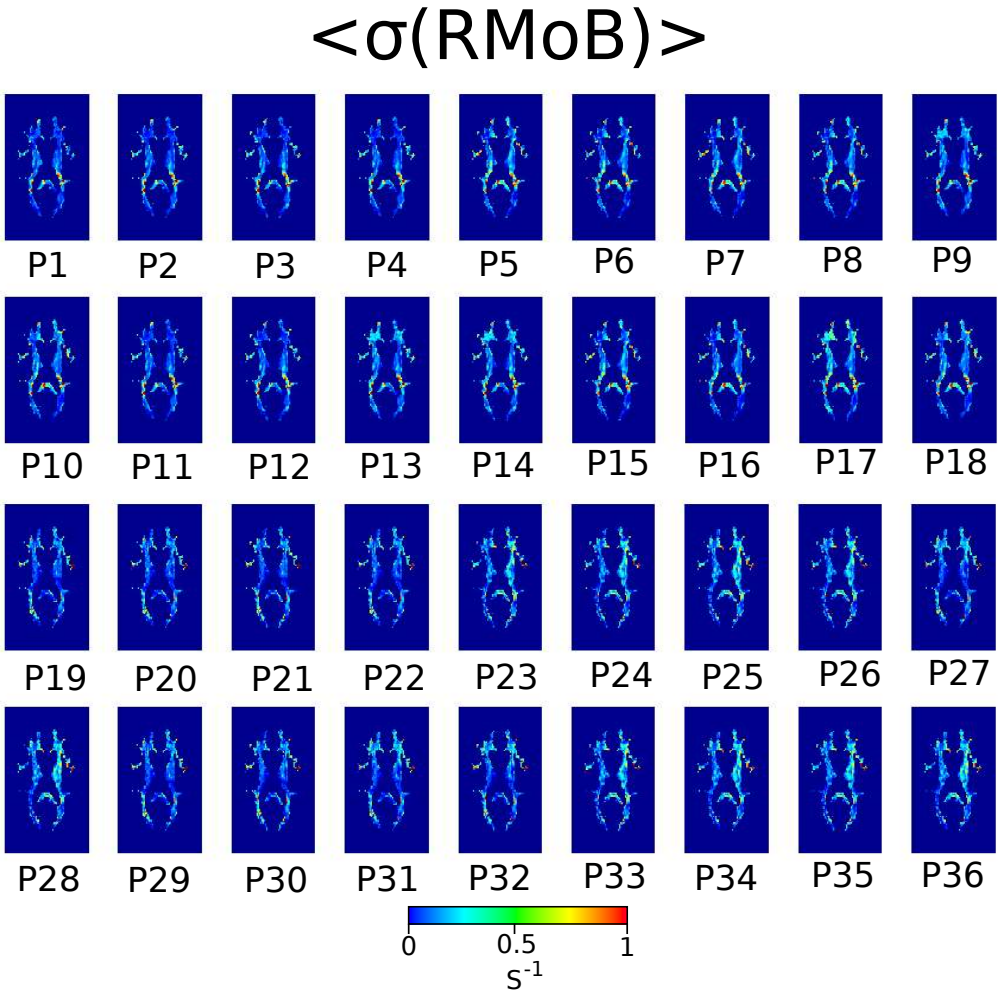

Figure 3.4: For a given slice, wild bootstrap estimates for $\langle\sigma(RM_0^B)\rangle$ (s^{-1}) across all protocols (P1-P36) within all 3 participants.

On the whole the wild-bootstrapping procedure reveals a large variability of measured uncertainties across protocols and tested parameters (RM_0^B, MMPF and T_2^B). The cross-correlation of the results from axial and sagittal acquisitions for the uncer-

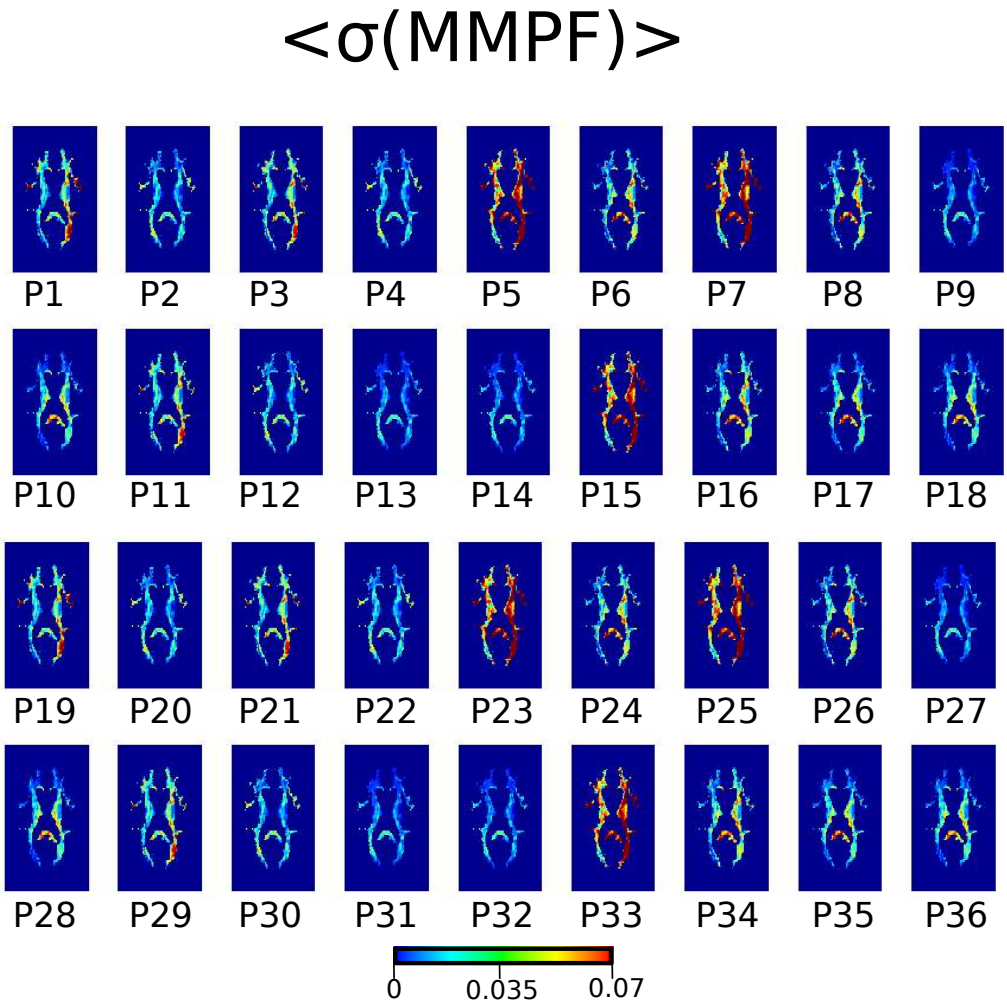

Figure 3.5: For a given slice, wild bootstrap estimates for $\langle \sigma(MMPF) \rangle$ (dimensionless) across all protocols (P1-P36) within all 3 participants.

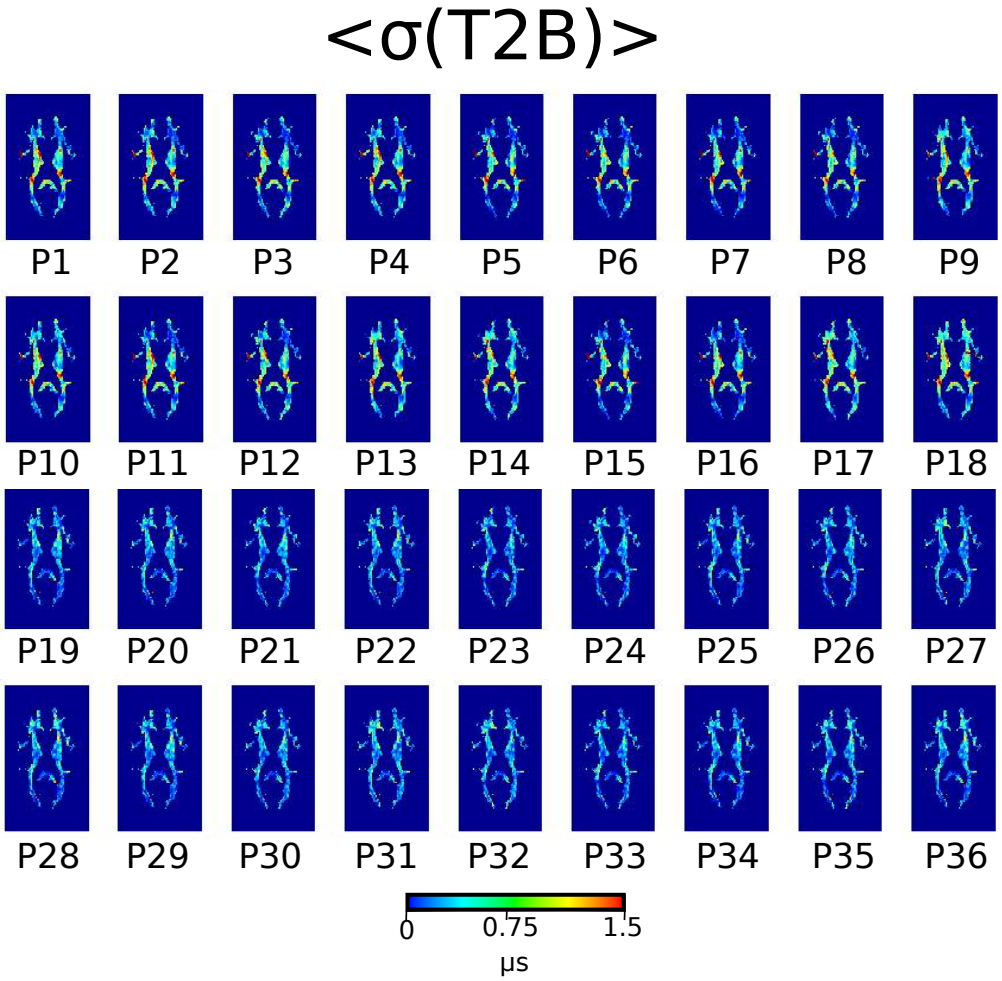

Figure 3.6: For a given slice, wild bootstrap estimates for $\langle\sigma(T_2^B)\rangle$ (μs) across all protocols (P1-P36) within all 3 participants.

tainty MMPF map reveals a large heterogeneity in the results (Figure 3.7). Selecting protocols in the last two rows of each CC-matrix in (A) shows that protocols P9^{Ax} and P14^{Ax} have similar uncertainties and as in Figure 3.5 have low uncertainty across WM; and (B) shows that protocols P27^{Sag} and P32^{Sag} have similar uncertainties and as in Figure 3.5 have low uncertainties. These two protocols are unique in that they do not combine a B_1 map with the mcDESPOT T_1 map.

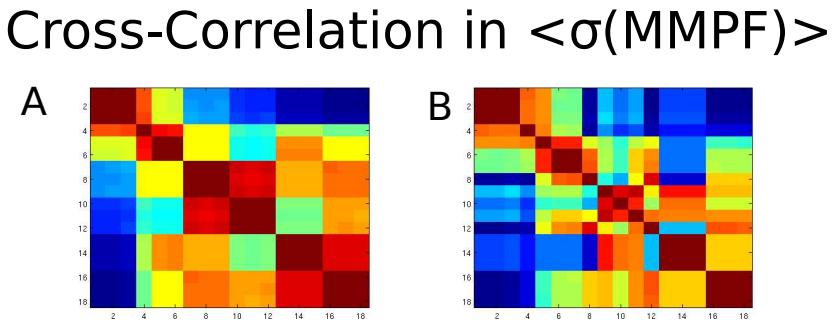

Figure 3.7: For a given slice the cross-correlations of MMPF uncertainty for each protocol/pipeline within all participants (N=16). (A) for axial protocol (P1-18) (B) for sagittal protocol (P19-P36).

3.3.3 Analysis of variance

The two-way ANOVA revealed that the protocol factor had a significant effect on three of the qMT parameters studied: $\langle\sigma(RM_0^B)\rangle$ ($F(35,2) = 4.53$, p <0.0001), $\langle\sigma(MMPF)\rangle$ ($F(35,2) = 4.53$, p<0.0001), and $\langle\sigma(T_2^B)\rangle$ ($F(35,2) = 8.21$, p<0.0001). No significant effect from the interaction between slice and protocol was observed. The results from the multi-comparisons for each map is as follows. For $\langle\sigma(RM_0^B)\rangle$ maps four protocols were labeled as having very high uncertainty (P13^{Ax}, P14^{Ax}, P17^{Ax} and P18^{Ax}) and the protocols that were determined to be significantly different from these four protocols were P19^{Sag}, P21^{Sag}, P27^{Sag}, P29^{Sag}, P30^{Sag} (p<0.05). For $\langle\sigma(MMPF)\rangle$ maps four protocols stood out as having extremely high uncertain-

ties ($P1^{Ax}$, $P5^{Ax}$, $P7^{Ax}$ and $P15^{Ax}$) and the protocols that were determined to be significantly different from these four protocols were $P9^{Ax}$, $P13^{Ax}$, $P27^{Sag}$ and $P32^{Sag}$ ($p < 0.05$). The uncertainty maps for T_2^B revealed four protocols with high uncertainties ($P13^{Ax}$, $P14^{Ax}$, $P17^{Ax}$ and $P18^{Ax}$) and the protocols that were determined to be significantly different from these four protocols were $P19^{Sag}$, $P21^{Sag}$, $P25^{Sag}$, $P29^{Sag}$, $P34^{Sag}$ and $P33^{Sag}$ ($p<0.05$).

3.4 Discussion

In the present study we used wild-bootstrapping to measure the uncertainties in qMT parameters in white matter across different qMT protocols. Two main findings resulted from our study. First, the residual deviation demonstrated that there are large differences in the residuals between the axial and sagittal acquisitions. Secondly, from wild-bootstrap analysis the uncertainties across protocols and between the three parameters studied were inconsistent. For example, within $P13^{Ax}$ the uncertainty within MMPF maps was deemed to be significantly lower than other protocols with the highest measured uncertainty, however, within T_2^B maps it is one of the protocols with the highest uncertainty. In other words, different protocols are optimal for different parameters. If one is most interested in estimating MMPF as precisely as possible, $P13^{Ax}$ appears to be the protocol of choice. However, to obtain reliable estimates of all three parameters (RM_0^B, MMPF and T_2^B), $P27^{Sag}$ was the best option since its uncertainty was low across all participants and parameters.

The residuals measured within MT-weighted fits demonstrate that certain offset frequencies produce higher errors. Specifically, the lowest offset frequency of 1000 Hz (MT points: 1, 2, 7 and 8), led to the largest residuals being largest with a saturation pulse ($\theta_{SAT} = 628$) (MT points: 7 and 8). Portnoy and Stanisz (2007) showed similar results that MT model using the CWPE approximation underestimated parameters when the offset frequency was 1000 Hz and below. With offset frequencies of this relatively small magnitude, the RF pulse frequency becomes close to the resonance frequency of the free water pool, and thus the direct effect (direct saturation of the liquid pool) will affect the measured MT-weighting. Therefore, it is desirable to acquire MT-weightings far enough away from 1000 Hz to make the direct effect negligible, but to cover enough of the frequency range to produce a reasonable model fit. Indeed, Portnoy and Stanisz (2007) have shown that the CWPE approximation does not model the system accurately below an offset frequency of 5 kHz resulting

in a reduction of approximately 1% in magnetisation of the liquid pool. On the whole all pulsed MT experiments/models have difficulty modeling the magnetization behaviour at low off-resonance frequencies. Moreover, with more qMT experiments being performed at higher magnetic field strengths the minimum offset frequency may need to be increased since fluctuations within the system (i.e. increased T_1 or decreased T_2) could cause the direct effect to persist at higher offset frequencies (Portnoy and Stanisz 2007). Thus, the cutoff frequency may need to be re-evaluated in our experiment and others that use CWPE approximation at higher field strengths.

Our results showed that the qMT fit residuals from the axial acquisitions (P1-P18^{Ax}) were lower than the sagittal acquisitions, which may be explained by the 8% difference in SNR between the the two sets of protocols (axial = 147.7 $\pm$ 27.2, sagittal = 135.4 $\pm$ 35.5).

In addition to RF noise, there are a number of other factors that introduce variance within the MRI system such as field inhomogeneities, which add variance within the measure MT-weighted signals and individual T_1 maps. Errors from T_1 maps and field maps can propagate into the qMT parameter estimation, thus these errors need to be evaluated and reduced. In the presence of field inhomogeneities, accurate modeling requires characterization of both B_1 and B_0 field distributions throughout the sample (Portnoy and Stanisz 2007). However, to reduce the influence of inhomogeneity on the free water pool it is recommended to apply a 1kHz cut off to the offset frequency to be further away from the direct saturation of the water pool (Portnoy and Stanisz 2007). Not sampling data at points below 1 kHz should not decrease the precision of qMT parameters since the signal change at these lower offset frequencies are mainly due to direct saturation of the liquid pool (A) and changes are independent of the sample's MT properties (Sled and Pike 2000a). Alternatively, there are a number of studies that have demonstrated that accurate B_1 and B_0 field maps provide more accurate MT calculations and thus more precise MT parameters (Sled et al. 2004; Ropele et al.

2005; Samson et al. 2006; Gochberg and Gore 2007). For example, Ropele et al. (2005) demonstrated that due to differences in coil characteristics between scanners differences of approximately 50% in MTR were observed between participants if B_1 errors were not corrected.

Uncertainties estimated from wild bootstraps (N=1000) for parameters RM_0^B, MMPF and T_2^B clearly demonstrate that uncertainties within and surrounding the ventricles are quite high. This is not unexpected since the ventricles are filled with free water and the CWPE model poorly characterizes this pool, especially at low offset frequencies (Portnoy and Stanisz 2007). On the other hand, the CWPE approximation can satisfactorily characterize the semisolid pool (B) since the uncertainties are lower within GM and WM as seen in Figure 3.2.

Our study revealed an unexpected result from the bootstrapping results, in that all three parameters had lower uncertainty with the sagittal acquisition than the axial acquisition. This appears counter-intuitive since one might predict from the residual deviation results that the uncertainty from the sagittal acquisition would produce higher uncertainty. However, this might arise from the model not fitting the data as well with the sagittal acquisition as it does with the axial acquisition.It should be noted, though, that the residual deviations measured within sagittal acquisition were significantly higher than the axial acquisition its average residual deviation is still below 1%, which is still a very good fit.

The variability in the uncertainties found in all three qMT parameters tested clearly illustrates the need to optimize the qMT method to reduce the uncertainties within a qMT protocol. Furthermore, the set of parameters that produced the lowest uncertainty in a given parameters was different for each qMT parameter. Specifically, the uncertainty in $P13^{Ax}$ was evaluated as low within MMPF maps, however, for T_2^B maps it was evaluated as high. The uncertainty within MMPF maps demonstrated

clear differences between the protocols. Protocols ($P5^{Ax}$, $P7^{Ax}$, $P15^{Ax}$, $P23^{Sag}$, $P25^{Sag}$ and $P33^{Sag}$) were found to have high uncertainty compared to the other protocols and more importantly heterogeneous uncertainty throughout white matter. The common features within these protocols are the combination of mcDESPOT B_1 map and SPGR 3-FA T_1 maps where there were no other protocols with this combination. This result is likely a result of poor estimation of B_1 within the mcDESPOT acquisition especially when using the SPGR 3-FA T_1 map to estimate MMPF. The protocols that used a B_1 map produced by the double angle method in combination of the SPGR 3-FA T_1 maps produced lower overall uncertainty, however this uncertainty was heterogeneously distributed throughout the brain, with high uncertainty in the genu of the corpus callosum. Considering the optimal protocol to have both low and homogenously distributed uncertainty throughout WM for all three model parameters, protocol $P19^{Sag}$ or $P27^{Sag}$ appears to be the best options. The first protocol $P19^{Sag}$ entailed using mcDESPOT to measure all three maps (B_1 and B_0 inhomogeneity maps and T_1 map). The second protocol $P27^{Sag}$ entailed using mcDESPOT for the T_1 map and had not field maps used in its analysis. This result demonstrates that the field maps used within this experiment may not appropriately characterize the field inhomogeneity within MT-weighted images especially if on wanted low uncertainity within MMPF, but for low uncertainty within RM_0^B and T_2^B field maps from mcDESPOT were deemed appropriate. Further investigation and evaluation of different field mapping methods is needed. Although improvements in measured uncertainties within some of the parameters, as a result of changing the protocol, were relatively small, it is important that the uncertainty is homogenously throughout white matter especially for clinical applications where qMT may be used to detect subtle changes in disease development that are undetectable with traditional MR contrast techniques.

Importantly, we showed using a wild bootstrap method is a powerful method in describing the uncertainty within qMT parameters that are used to describe subtle

changes in WM as in pathologies like MS. There is a critical need for the application of such methods in providing a component of quality control and parameter uncertainty estimation. In comparison to rescanning techniques, wild bootstrapping allows for the estimation of uncertainty in a more cost-effective manner (in terms of data acquisition) and can be used to further optimize qMT protocols and other quantitative methods. Continued efforts in optimizing and determining the best protocol through determining the best offset frequencies (perhaps moving further away from direct saturation), saturation pulses, inhomogeneity field maps (B_1 and B_0) and T_1 maps, will help us reduce the uncertainties further and to produce homogenous uncertainty maps for qMT parameters, such as MMPF.

Chapter 4

Tract-specific Measurements

4.1 Introduction

Neuronal white matter consists of a complex array of networks connecting cortices throughout the brain by means of distinct tracts. The microstructure of these tracts mediates the 'information' transfer or electrical transmission between the different cortical regions vital for functional connectivity. Most white matter fiber tracts within the brain are wrapped with an insulating membrane, known as myelin, which enhances fast electrical transmission along the axons. The microstructure of white matter is comprised of different subcomponents (including myelin and axons), and changes to any of those subcomponents will lead to neurological deficits. In understanding these deficits, it is important to be able to specifically probe these different subcomponents. The ability to quantify these subcomponents non-invasively is therefore of great importance within clinical neuroimaging research.

Regardless of recent developments in imaging technology, quantifying tissue microstructure subcomponents non-invasively is challenging. The difficulties in assessing myelin with magnetic resonance arise from that fact that its signal quickly decays to zero in a matter of microseconds ($\sim$10 us) and its signal is indistinguishable from other non-aqueous constituents in brain tissue (MacKay et al. 2006). Similarly, axonal density is difficult to estimate due to the heterogeneous nature of the surrounding tissue containing astrocytes, glia and extracellular molecules. A further limitation or challenge relevant to assessing myelin or axons non-invasively is spatial resolution,

since for healthy white matter axon diameters are in the range of 0.5-20 μm and myelin thickness is close to 1 μm. Nevertheless, a number of indirect magnetic resonance techniques have been used to further our understanding of myelin development, axonal loss and white matter pathology. Studies of conditions in which myelin is compromised, such as multiple-sclerosis (MS) (MacKay et al. 1994; Brochet and Dousset 1999; Assaf et al. 2002; Cercignani et al. 2009; Levesque et al. 2010) and schizophrenia (Flynn et al. 2003), have demonstrated that a decrease in myelination impacts functional connectivity, resulting in behavioural changes. Although these results are encouraging, there is no single technique that can capture specific changes in both axon and myelin thus no consensus on the best imaging method to measure changes in white matter microstructure.

The most common methods used to indirectly infer on changes/differences in myelination include diffusion-weighted imaging, quantitative magnetization transfer imaging and multi-component relaxometry. Other methods, such as those that quantify non-Gaussian diffusion processes have the potential to provide greater specificity to axonal damage or loss than Gaussian-diffusion-based methods, such as diffusion tensor MRI. Thus, while there is a spectrum of imaging methods that have differential sensitivities to myelin and axon properties, it is unclear how they compare with each other and how differently they characterise tissue microstructure.

Diffusion MRI (Le Bihan and Breton 1985) is able to probe white matter microstructure due to the fact that axons (and their subcomponents) create coherent obstacles to diffusion and therefore an orientational dependency of the apparent diffusion coefficient (Moseley et al. 1990). Frequently, this orientational dependence is modeled by a second-rank tensor assuming a uni-modal Gaussian displacement profile, and a diffusion tensor is fitted to the signals in each voxel (Moseley et al. 1990; Pierpaoli et al. 1996). Tensor estimates provide scalar indices, such as fractional anisotropy (FA) - a normalized index of the standard deviation of the eigenvalues

that has a range of 0-1 and radial diffusivity (RD) - the average of the eigenvalues perpendicular to the principal diffusion direction (Basser and Pierpaoli 1996).

Due to the excellent sensitivity of diffusion tensor imaging to various white matter structures it has been developed as a tool to investigate white matter pathways. Diffusion properties such as fractional anisotropy (FA), radial diffusivity and principal diffusion direction (eigenvector with the largest eigenvalue) have been used in a number of clinical, neuroscience and neurodevelopmental studies (Johansen-Berg et al. 2007; Johansen-Berg 2007). However, diffusion indices complex measures are influenced by various microstructural properties such as, axonal density and diameter, myelination and intra-voxel axon orientational dispersion (Beaulieu 2002). Thus, while diffusion measures are very sensitive to a change in microstructure, they are very non-specific indices (Beaulieu and Allen 1994a; Beaulieu 2002) and need to be interpreted with caution. In various animal models, invariably using isolated pathways, where all axons are aligned along the same axis, it has been shown that a reduction in myelin leads to an increase in the radial diffusivity (Song et al. 2002; Song et al. 2003). These studies have led some investigators to regard changes in RD, therefore, as a marker of changes in myelin. However, it is important to note that diffusion can be significantly hindered in the perpendicular direction (compared to the longitudinal direction) even when there is no myelin present (Beaulieu 2002). It is also known that the radial diffusivity changes with differences in axon diameter. Finally, when there is intravoxel orientational dispersion, the link between a change in RD and myelin content becomes even less clear.

Magnetisation transfer (MT) is a magnetic resonance (MR) imaging technique that provides a measure of the relative density of macromolecules within the tissue by harnessing information on the exchange of magnetization between macromolecular and water protons. MT provides quantifiable information on macromolecular components such as; protein, lipids and cellular membranes, which are invisible to

conventional longitudinal T_1 and transverse T_2-weighted scans owing to their very short T_2 decay times ($\sim$10μs) (Wolff and Balaban 1989). Often, MT acquisitions use time-varying pulsed amplitudes to apply an off-resonance radiofrequency (RF) pulse that selectively saturates the macromolecular magnetization (Sled and Pike 2001; Ramani et al. 2002; Yarnykh 2002). The resulting decrease in the signal measured from the free pool is attributed to the transfer of magnetization from saturated macromolecules to free water protons occurring through cross-relaxation or chemical exchange (Ceckler et al. 1991; Kucharczyk et al. 1994).

MT models typically split the brain into two different compartments by grouping spins into: a free or liquid pool (Pool A) consisting of water protons with a long T_2 (T_2 >10 ms) and a restricted or semisolid (macromolecular) pool (Pool B) consisting of protons within lipids with very short T_2s (T_2 <100 μs). Magnetisation transfer imaging provides an estimate of the macromolecular proton fraction (MMPF), which is a measure of the number of trapped protons in the macromolecular pool, such as myelin, relative to the total number of protons present (Ramani et al. 2002). Importantly, the MMPF has been shown to related to myelin lipid content measured using the Luxol fast blue stain within both postmortem fixed tissue (Schmierer et al. 2007) and fresh tissue (Schmierer et al. 2008). A number of research groups have demonstrated through histological staining of white matter that magnetisation transfer ratio (MTR - ratio between two volumes with and without an MT-pulse)(van Waesberghe and Barkhof 1999; Bot et al. 2004; Schmierer et al. 2008) significantly correlates with axonal density. Furthermore, MMPF has been shown to be a predictor of demyelination and remyelination within postmortem MS white matter studies (Schmierer et al. 2007). (Schmierer et al., 2007). It has thus been argued that MT parameters, such as the MMPF, are biomarkers for white matter pathologies such as inflammation, demyelination and axonal loss (Stanisz et al. 1999; Sled and Pike 2001; Stanisz et al. 2004; Davies et al. 2005; Levesque et al. 2005; Tozer et al. 2005).

Multi-component relaxometry (MCR) exploits the fact that different liquid sub-populations have unique relaxation times to provide detailed information on the brain's microstructure, including myelin water. Conventionally, multi-component T_2 relaxometry is performed using a multi-spin echo sequence, a 32- or 48-echo Carr-Purcell-Meiboom-Gill (CPMG) pulse sequence (MacKay et al. 1994). However, this sequence requires at least 15 minutes of scan time for only a few slices/very thick slices (Wu et al. 2006). This time requirements makes the multi-echo approach impractical for most applications, leading to the introduction of a number of alternative multi-component relaxometry techniques to reduce scan time (Jones et al. 2004; Vidarsson et al. 2005; Bells et al. 2007; Deoni et al. 2008; Deoni et al. 2008). In this work, we used the technique developed by Deoni et al. known as multi-component driven equilibrium single pulse observation of T_1 and T_2 (mcDESPOT) (Deoni et al. 2008; Deoni et al. 2008) which combines two rapid sequences: spoiled gradient recalled echo (SPGR) and balanced steady-state free precession (bSSFP) over a range of optimised flip angles. The mcDESPOT approach combines phase-cycling with a calibrated phase-precession map (B_0, off-resonance) for bSSFP images (Deoni et al. 2004) and transmit magnetic inhomogeneity (B_1) maps to reduce artifacts caused by field inhomogeneities (Deoni 2009). The advantage of mcDESPOT over multi-echo techniques is its higher signal to noise efficiency and shorter acquisition times, in turn resulting in smaller motion artifacts (Deoni et al. 2003).

Multi-component relaxometry models for white matter have at least three distinguishable water environments classified according to their relaxation times: water trapped in the myelin bilayer or sheath (T_2 = 10-50 ms), water in the intracellular and extracellular space (T_2 = 70-90 ms) and cerebral spinal fluid (T_2 >2s)(MacKay et al. 1994; MacKay et al. 2006). Dividing the signal from the myelin water by the signal from total water gives a metric known as the myelin water fraction (MWF) (MacKay et al. 1994), which is commonly regarded as a marker of myelin in white

matter. Comparison studies between MWF and histological-derived estimates using Luxol fast blue showed that changes in MWF and changes in actual myelin are highly correlated (Moore et al. 2000; Laule et al. 2006; Laule et al. 2008). MWF has been used to measure changes in white matter microstructure due to lesions and MS (Vavasour et al. 1998; Whittall et al. 2002; Laule et al. 2004).

Diffusion MR techniques that characterize the non-Gaussian properties of the signal are thought to provide enhanced sensitivity to intra-axonal compartments (while extra-axonal water diffusion is assumed to be Gaussian). In white matter, the diffusion MR signal digresses from mono-exponential decay, especially at high diffusion weightings or b-values (>1500 s/mm^2), suggesting the existence of more than one compartment. At higher b-values, the signal attenuation is dominated by slower diffusing species (assumed to be intra-axonal), while at lower b-values, signal attenuation is dominated by the faster-diffusing species, assumed to be hindered molecules in the extra-axonal space. The combined hindered and restricted model of diffusion (CHARMED) analysis pipeline (Assaf et al. 2004; Assaf and Basser 2005) acquires diffusion-weighted signals from a variety of diffusion weightings, including high and low. The CHARMED model separates the diffusion signal into two compartments: a hindered extra-axonal compartment, which is described by an effective diffusion tensor, and one or more intra-axonal compartments, which are described by a model of restricted diffusion within impermeable cylinders. CHARMED estimates provide micro-structural parameters, such as, fibre orientation, extra- and intra-axonal volume fractions (albeit T_2-weighted) and axonal diffusivities. The intra-axonal volume fraction estimated from CHARMED has been used as an index of axonal density. The potential of this metric as a biomarker for axonal microstructural changes arising from short term neuro-plasticity has recently been reported by Tavor et al. (2011). The CHARMED model has been extended to provide estimates of the axon diameter

distribution within a white matter bundle (Assaf et al. 2008; Barazany et al. 2009; Alexander et al. 2010).

Despite the growing number of experiments using different microstructure metrics in assessments of white matter, there has been limited work on the correlation between these different white matter metrics *in vivo* and along specific neuronal tracts. A great number of correlation studies have used postmortem brains (Schmierer et al. 2007), excised tissue (Stanisz and Henkelman 1998; Peled et al. 1999) or *in vivo* animal experiments (Andrews et al. 2006) due to of the ability to safely use strong MR gradients and provide complimentary histological measurements. One such postmortem study combined MTR, T_2-relaxometry and diffusion metrics (RD and FA), which revealed that all indices were predictors of myelin content and MTR was found to be the greatest predictor (Schmierer et al. 2008). However, within excised, the peripheral nerve, tissue it was found that MWF, axonal water and MTR all correlated weakly (Does et al. 1998). Only a handful of experiments have compared these metrics within the brain, such correlations include: DTI and MWF (Mädler et al. 2008), DTI and qMT (Underhill et al. 2009), qMT and MWF (Levesque et al. 2010) and MWF and MTR (Vavasour et al. 2011). Mädler et al. (2008) found significant correlations between MWF-FA and MWF-RD within regions of interest drawn in various white matter areas (genu of the corpus callosum(cc), minor and major forceps, splenium of the cc and posterior internal capsule) and grey matter areas (caudate nucleus, putamen, thalamus, cingulated gyrus, insular cortex and cortical gray). However, Underhill et al. (2009) found no correlation between DTI metrics: FA, ADC, RD and λ_1 and qMT metrics (MMPF). In addition, Levesque et al. (2010) found no significant correlations between qMT-MMPF and MWF maps in MS human data. This lack of correlation within white matter imaging metrics most likely reflects the differences in the physical principles underpinning their generation. In this work, a novel comprehensive assessment of tract-specific microstructural measurements is

introduced. This method, called 'tractometry', combines macromolecular measurements from quantitative magnetization (MMPF), multi-component T_2 species from relaxometry (MWF) and 'restricted diffusion' measurements from CHARMED along specific white matter pathways reconstructed from diffusion MRI. Results provide insights into the relationship between these microstructure metrics and help explain the relationship between radial diffusivity and other metrics of axon or myelin morphology.

4.2 Material and Methods

4.2.1 Participants

A total of twenty-seven healthy right-handed female participants (mean age= 31.7±4.0 y) were included in this study, where a subset of six participants was included in the CHARMED acquisition. Informed consent was obtained prior to scanning and the study was performed with ethics approval from the ethics review board at our institution.

4.2.2 MR Imaging acquisition

MRI data were acquired on a 3 T General Electric HDx MRI system (GE Medical Systems, Milwaukee, WI) using an eight channel receive only head RF coil (Medical Devices). Four different MRI protocols were used: high angular resolution diffusion-weighted, quantitative magnetization transfer, mcDESPOT and CHARMED (total scan time 1 hour and with CHARMED 1.5 hours).

4.2.3 High Angular Resolution Diffusion-Weighted MRI

A twice-refocused spin-echo EPI diffusion-weighted acquisition was peripherally gated to the cardiac cycle using an in-house modified version of the vendor's diffusion-weighted sequence resulting in 2-3 slices per R-R interval, conditional on the participant's heart rate. The diffusion-weighted protocol consisted of: sixty axial slices, with effective TR = 20/15 R-R intervals; effective TE = 87ms; acquisition matrix = 96x96; slice thickness = 2.4 mm; FOV of 230 mm; b-value of 1200 s/mm^2 along 60 isotropically distributed gradient directions (Jones et al. 1999); six non-diffusion weighted images; ASSET factor = 2 (Jones and Leemans 2011); total acquisition time = 30 minutes.

4.2.4 mcDESPOT

The mcDESPOT protocol consists of a combination of sagittally oriented SPGR, bSSFP and inversion-recovery prepared SPGR (IR-SPGR) sequences (Deoni et al. 2008; Deoni et al. 2008). All three were acquired with a FOV of 220 mm; 1.7 mm anterior-posterior x 1.7 mm left-right x 1.7 mm superior-inferior, with frequency encoding in the superior-inferior direction for a total mcDESPOT scan time of approximately 8 minutes. Additional sequence specific parameters were:

- SPGR: TE/TR = 2.1/4.7 ms; BW = ±25 kHz; flip angle (α) = [3°, 4°, 5°, 6°, 7°, 9°, 13°, 18°].

- bSSFP: TE/TR = 1.6/3.2 ms; BW = ±62.5; α = [10.6°, 14.1°, 18.5°, 23.8°, 29.1°, 35.3°, 45°, 60°] for both phase-cycling acquisitions of 0° and 180°.

- IR-SPGR: TE/TE = ms; BW = ±25; α = 5°; inversion time = 450 ms.

4.2.5 Quantitative Magnetization Transfer MRI

An optimized 3D MT-weighted fast spoiled gradient recalled-echo (SPGR) sequence (Cercignani et al. 2005) was used with the following parameters: TR/TE = 26.65/1.86 ms; Gaussian MT pulses, duration τ = 14.6 ms; FOV = 230 mm; acquisition matrix = 128x96x66; BW=$\pm$244Hz. The off-resonance irradiation frequencies (Δ) and their corresponding saturation pulse amplitude (θ_{SAT}) for the 11 MT weighted images were optimized using Cramer-Rao lower bound optimization (Cercignani and Alexander 2006) are: Δ = [1000.0 Hz, 1000.0 Hz, 12062.0 Hz, 47185.0 Hz, 56363.0 Hz, 2751.0 Hz, 1000.0 Hz, 1000.0 Hz, 2768.0 Hz, 2791 Hz, 2887.0 Hz] and their corresponding θ_{SAT} = [332.0°, 333.0°, 628.0°, 628.0°, 332.0°, 628.0°, 628.0°, 628.0°, 628.0°, 628.0°, 628.0°].

4.2.6 CHARMED

A spin-echo EPI diffusion-weighted acquisition was used to acquire whole brain coverage of CHARMED data with the following parameters: TR/TE = 17000/114 ms; Δ/δ = 50/43 ms; FOV = 230 mm; slice thickness = 2.4 mm; number of slices = 39; in-plane resolution = 1.8 x 1.8 mm^2. The diffusion encoding gradients were applied along 130 noncolinear directions at 8 different b values: 937, 1875, 2812, 3750, 4687.5, 5625, 6562.5, 7500 s/mm^2; resulting in a total acquisition time of approximately 30 minutes.

4.2.7 Additional Scans

In addition to the four main protocols, field maps were also acquired. For B_1 maps a two fast-spin echo sequences with double-angles were collected (TE = 1.6ms, TR = 3.2 ms, flip angles = 90, 45, respectively, matrix = 128x128, FOV =300x300x500mm^3,

scan time =1min each)(Cunningham et al. 2006) and for B_0 maps a two 3dgrass with different TE's were collected (TE = 9ms and 7ms,respectively, TR= 20ms, matrix=128x128, FOV= 220x220x3mm^3)(Jezzard and Balaban 1995).

4.2.8 Diffusion Data Pre-Processing

Diffusion-weighed images were corrected for participant motion and global geometric distortions using an affine (12 degrees of freedom) coregistration technique based on mutual information to the first non-diffusion weighted volume. This was followed by appropriate re-orientation of the diffusion encoding vectors (Leemans et al. 2009) and modulation of the signal intensity by the Jacobian determinant of the transformation (Jones and Cercignani 2010). The diffusion-weighted data were modeled three ways: (a) a single tensor (Basser et al. 1994b) was fitted using non-linear least squares estimation providing quantitative scalar indices such as fractional anisotropy (FA), mean diffusivity (MD), principal eigenvalue (λ_1), radial diffusivity (RD), mode of anisotropy (AM), geometric measures (GEO) and intervoxel diffusion coherence (IVDC); (b) a two compartment modelling approach termed 'Free Water Elimination' (FWE) (Pasternak et al. 2009) yielding diffusion metrics that are corrected for CSF partial-volume contamination and a tissue volume fraction V_f; and (c) constrained spherical harmonic deconvolution (CSD) to extract a fibre orientation density function (fODF) (Tournier et al. 2004) in each voxel to allow fibre tract reconstruction through areas of crossing fibres. The AM varies between -1 and +1 to describe the different shape types of anisotropy within a voxel and ranges from planar ($\lambda_1 \sim \lambda_2 > \lambda_3$ e.g. in regions of crossing fibres of two similar density fibre populations or regions of "kissing" fibres) to linear ($\lambda_1 > \lambda_2 \sim \lambda_3$ e.g. in regions where is a dominating single fibre population) (Ennis and Kindlmann 2006; Wang et al. 2008). The GEO is a decomposition of the diffusion tensor into basic geometric

shapes: linear ($\lambda_1 >> \lambda_2 \sim \lambda_3$) where diffusion is largely in the direction of λ_1 and planar ($\lambda_1 \sim \lambda_2 >> \lambda_3$) where diffusion is restricted to a plane represented by λ_1 and λ_2 (Westin et al. 2002). IVDC provides a quantitative measure of the directional coherence of the principal water diffusion based on the eigenvectors within a voxel and its neighbours. In areas where the directional diffusion is uniform IVDC increases, while IVDC approaches zero in areas where diffusion is heterogenous as in the ventricles (Wang et al. 2008).

4.2.9 mcDESPOT Pre-Processing

SPGR and bSSFP images for each participant were linearly coregistered using an affine (12 degrees of freedom) technique based on mutual information to the first image in the sequence to correct for interscan and intrascan motion (Jenkinson and Smith 2001). SPGR and IR-SPGR images were used for DESPOT1 with High-speed Incorporation (DESPOT1-HIFI) of RF Field Inhomogeneities processing as described in (Deoni et al. 2006; Deoni 2007), resulting in B_1 field and T_1 maps. Furthermore, the B_1 field and T_1 maps were used in the calculation of B_0 field and T_2 maps using two phase-cycled bSSFP data using the DESPOT2 with full modeling (DESPOT2-FM) algorithm (Deoni et al. 2004). Combining high-resolution DESPOT1-HIFI and DESPOT2-FM 3D sequences allowed for the fitting of the multi-component DESPOT model (Deoni et al. 2008; Deoni et al. 2008). This model provides whole brain estimates for the following parameters: myelin water fraction (MWF), myelin water residence time and intra- and extra-cellular (IE) water and myelin water T_1 and T_2.

4.2.10 qMT Pre-Processing

All eleven MT-weighted SPGR volumes for each participant were linearly coregistered to the MT-volume with the most contrast using an affine (12 degrees of freedom)

technique based on mutual information to correct for interscan motion (Jenkinson and Smith 2001). Furthermore, the map of the longitudinal relaxation rate, T_{1obs}, which was measured with DESPOT-HIFI processing was linearly registered using an affine (12 degrees of freedom) technique to the same MT-volume used in the previous registration. The 11 MT-weighted SPGR images and T_{1obs} map were modeled by the two pool Ramani's pulsed MT approximation (Ramani et al. 2002), which included corrections for static field (B_0) and amplitude of radio-frequency (B_1) field inhomogeneities. In total this model has six maps were produced: R_1^B, RM_0^A, gM_0^A, $MMPF/R_1^A(1-MMPF)$,$1/R_1^AT_2^A$ and T_2^B, where R_1^A and R_1^B are the reciprocals of the T_1 of the A and B pools, respectively, T_2^A and T_2^B are the transverse relaxation times of each pool, M_0^A the initial magnetization of the A pool and g the scanner gain. The longitudinal relaxation rate, T_{1obs}, estimated from the DESPOT pipeline was used in the estimation of the longitudinal relaxation rate for the liquid pool (R_1^A) using the approximation proposed by Henkelman et al. (1993), allowing one to determine the macromolecular proton fraction, MMPF.

4.2.11 CHARMED Pre-Processing

An in-house program (Matlab, The Mathworks, Natick, MA) was used to calculate CHARMED parameters based on previous work (Assaf et al. 2004). The calculations were performed using a non-linear least squares (Levemberg-Marquardt minimization) giving the estimation of restricted volume fraction, Fr.

4.2.12 Registration of White matter microstructure indices

Prior to further analysis, all quantitative maps from the different pipelines were first coregistered. To this end, all data were non-linearly registered to the FA map for each participant. Prior to registration, a synthetic T_1-weighted image was calculated

from the T_1-map (Deoni et al. 2006) and then used to non-linearly register the DESPOT images to the FA map of a participant (a nonlinear registration was used to compensate for EPI geometric distortions present in the diffusion data, that were not present in the DESPOT data). The non-linear registration approach was performed using the approach of Rueckert et al. (1999) as implemented in FNIRT - a part of the FSL software package (Andersson et al. 2007a; Andersson et al. 2007b). Similarly, a synthetic T_1-weighted image was derived from the calculated T_1 map of the free-water pool (T_1^A) from the qMT pipeline and used to non-linearly register the qMT data to the FA map of the participant.

4.2.13 Partial Volume Corrections of MWF and MMPF

When interpreting parameters such as myelin water fraction (MWF) and macromolecular proton fraction (MMPF), implicitly one thinks of the amount of signal coming from the tissue that has a short T_2 (MWF) or is macromolecular (MMPF). In voxels that only contain tissue, this interpretation is clear. However, in areas bordering CSF, for example, the finite volume of the voxel means that the signal comes partially from the tissue and partially from 'free water' (e.g. CSF). While methods have been developed in diffusion MR to account for CSF-partial volume contamination (Pasternak et al. 2009; Metzler-Baddeley et al. 2012), CSF-partial volume effects are largely ignored in methods such as mcDESPOT and qMT. We recently suggested a way in which the free water fraction derived from co-registered diffusion data could be used to correct other quantitative maps for CSF-contamination (Bells et al. 2011). Using the tissue-volume fraction map from diffusion imaging data the MWF and MMPF were corrected for partial volume effects (PVE)s. MWF and MMPF corrected data were calculated by dividing the measured MWF or MMPF by

the tissue volume fraction arising from Pasternak's pipeline, thus giving us a measure of uncontaminated MWF and MMPF values.

4.2.14 Fibre Tract Reconstructions

The tracking algorithm used here is an adptation of the standard streamline tractography for CSD (Jeurissen et al. 2011), whereby every voxel in the data set is considered as a possible seedpoint for the initiation of tracking and fODF peak estimation (Tournier et al. 2004; Tournier et al. 2007; Tournier et al. 2008) using *ExploreDTI* (Leemans et al. 2009). Afterwards, the fODF peak direction that is most aligned with the previous stepping direction is extracted and then the trajectory is advanced by a fixed step size (0.5 mm). Tracking is halted when the fODF peak intensity falls below the fixed threshold (0.1) or/and a maximum angle between two consecutive steps exceeds (30°). Three-dimensional reconstructions of the following tracts: uncinate fasciculus (UNC), cortico-spinal tract (CST) and splenium of the corpus callosum (sCC) were made using the neuroanatomical landmark techniques that have been previously shown to be highly reproducible (Catani et al. 2002) (See Figure 4.1 for reconstructed tracts). Metrics of MD, RD, λ_1, FA, V_f, MMPF and MWF were computed for individual streamlines at every 0.5 mm step and averaged to produce tract-specific mean values (Jones et al. 2005).

4.2.15 Correlation along specific white matter tracts

Correlations in microstructural metrics was looked for between the following metrics: FA, MD,λ_1/L1, RD, MWF and MMPF. Correlations of tract-averages were examined using a Pearson-correlation, preceded by a one-sample Kolmogorov-Smirnov to test for Gaussianity. Correlation measures were then adjusted for multiple compar-

isons using the false discovery rate (FDR) approach (5%) (Benjamini and Hochberg 1995).

4.2.16 Tractometry Analysis

All tract-reconstructions and metric overlays were performed with *ExploreDTI* (Leemans et al. 2009). The following maps were overlaid onto all tracts: FA, MD, RD, geometric image (GEO), mode of anisotropy (AM), intervoxel diffusion coherence (IVDC), MWF, MMPF and Fr. A Pearson-correlation between the following indices: FA, RD, MWF, MMPF and Fr were calculated for all steps along the left cortico-spinal tract (CST). To explore the relationship between the various parameters in greater detail, scatter plots were made of the data in a pairwise fashion. Domains within the scatter plots were identified using simple boundaries (e.g. dividing the scatter plot ranges into quadrants, with upper and lower 50^{th} percentile for both metrics). Subsequently these domains were backprojected onto the CST tract for visualisation.

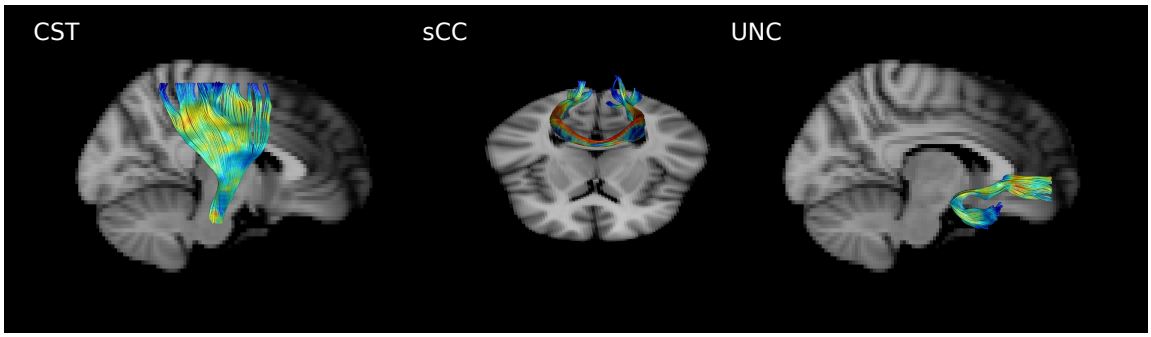

Figure 4.1: Example of the three tracts used in the analysis of this chapter. Cortico-spinal tract (CST), splenium of the corpus callosum (sCC) and uncinate fasciculus (UNC).

4.3 Results

A comprehensive comparison was conducted of the inter-correlations between the mean tract values of different white matter metrics across all 27 participants in the corticospinal tract (CST), splenium of the corpus callosum (sCC) and uncinate (UNC) fasciculus (Table 4.1-4.3, Figure 4.2). In Figure 4.2, the CST is used as an example to demonstrate the scatter plots for each comparison made (FA, RD, MWF, MMFP, T_1 and Fr). Two significant inverse correlations were found within the reconstructed CST tracts for both left and right hemispheres: FA versus RD and MWF versus T_1. No other pair-wise correlation reached significance. White matter metric correlations within the sCC are represented in Table 4.2. A significant inverse relationship was found between: FA versus RD, FA versus T_1 and MWF versus T_1, while only within the native (uncorrected CSF metrics) a significant inverse relationship was found between RD and MMPF (Table 4.2). No other pair-wise correlation reached significance. In the uncinate, significant inverse correlations were found between FA and RD and between MWF and T_1 for both the right and left hemisphere. In metrics not corrected for free water, the only pair-wise correlation that was significant was between RD and MWF in the right uncinate. No other pairwise metric correlations within the UNC reached significance.

To appreciate the impact of macrostructure on the microstructural metrics, parameters of interest were visualized along the trajectories of the three bundles: CST, sCC and UNC (Figure 4.3, 4.4 and 4.5). The differences in the spatial distribution of the different indices along the bundles can be clearly appreciated within these figures. In Figure 4.3 the metrics for CST are shown, where the metrics MWF, MMPF, Fr and FA all get progressively lower as the tract approaches the cortex, as expected. The diffusion metrics FA and AM appear to be more sensitive to areas of intra-voxel orientational heterogeneity and as expected give similar results to inter-voxel orietnational heterogeneity (IVDC). Overall, FA appears to be more heterogeneous

Table 4.1: Statistical results for the CST and the correlations between indices for 27 participants: Pearson coefficient (Superscripts 'u' and 'c' indicate the data are uncorrected or corrected for CSF-contamination by FWE approach, respectively). LS (left hemisphere), RS (right hemisphere), FA (fractional anisotropy), RD (radial diffusivity), MWF (myelin water fraction), MMPF (macromolecular proton fraction), T_1 (longitudinal relaxation time), Fr (restricted diffusion), $\star\star\star$ (p <0.001) $\star\star$ (p <0.01), $\star$ (p <0.05), $^{+}$ (p <0.05 - does not pass FDR multiple comparisons).

	Side	FA^u	RD^u	MWF^u	$MMPF^u$	T_1	Fr
FA^u	LS		-0.49***	-0.11	0.17	0.06	0.2
	RS		-0.52***	-0.12	0.11	0.009	-0.07
RD^u	LS			0.060	-0.16	0.11	0.067
	RS			0.066	-0.10	0.11	0.20
MWF^u	LS				0.13	-0.40***	-0.067
	RS				0.11	-0.49***	-0.20
$MMPF^u$	LS					0.18	0.20
	RS					0.088	0.33
$T_1{}^u$	LS						0.067
	RS						0.067
	Side	FA^c	RD^c	MWF^c	$MMPF^c$	T_1	Fr
FA^c	LS		-0.61***	-0.11	0.18	0.0028	0.2
	RD		-0.71***	-0.12	0.12	-0.037	0.067
RD^c	LS			0.12	0.23	0.031	0.067
	RD			0.048	0.05	0.088	0.2
MWF^c	LS				-0.17	-0.62***	-0.067
	RD				-0.15	-0.73***	-0.20
$MMPF^c$	LS					0.19	0.067
	RD					0.071	0.067

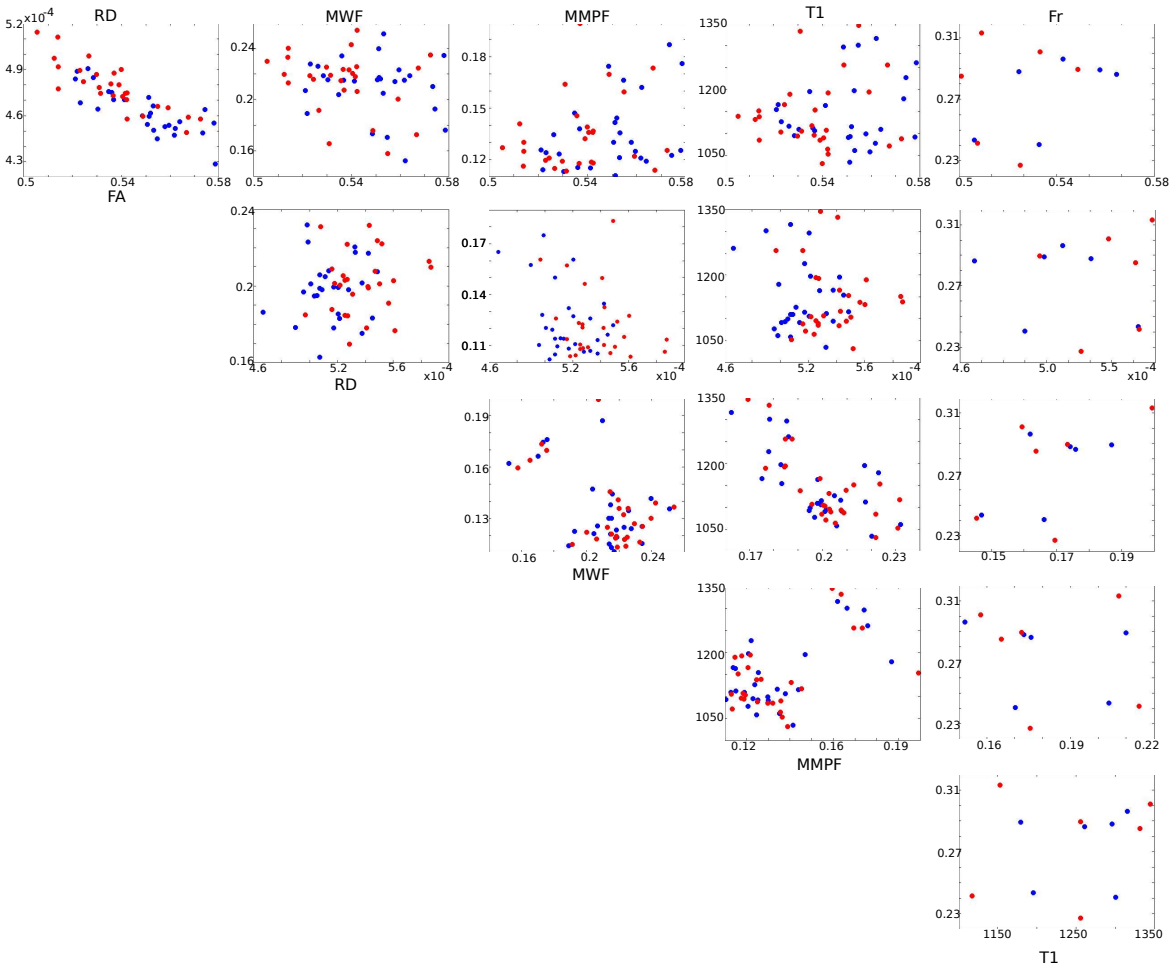

Figure 4.2: Scatter plots for the CST for different white matter metrics. Left hemisphere (blue), right hemisphere (red), FA (fractional anisotropy), RD (radial diffusivity), MWF (myelin water fraction), MMPF (macromolecular proton fraction), T1 (longitudinal relaxation time), Fr (restricted diffusion).

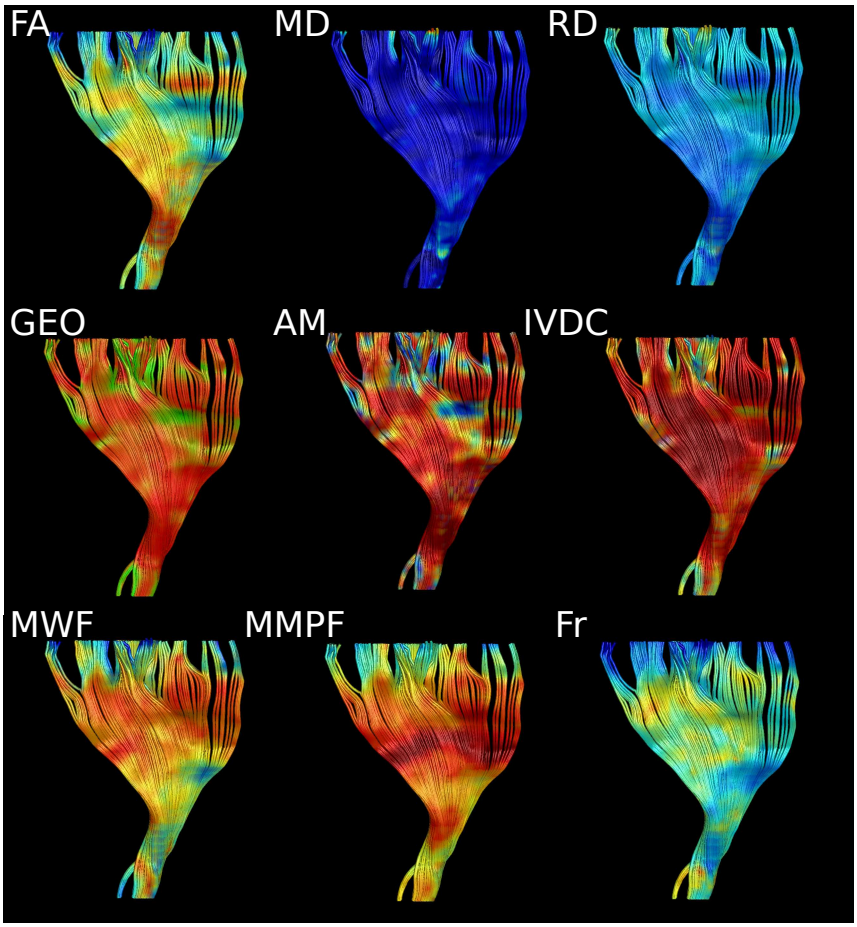

Figure 4.3: Tract-specific microstructural measurements or tractometry of the CST. FA (fractional anisotropy), MD (mean diffusivity), RD (radial diffusivity), GEO (geometric image), AM (mode of diffusion), IVDC (intravoxel diffusion coherence), MWF (myelin water fraction), MMPF (macromolecular proton fraction), Fr (restricted diffusion).

Table 4.2: Statistical results for the sCC and the correlations between indices for 27 participants: Pearson coefficient (Superscripts 'u' and 'c' indicate the data are uncorrected or corrected for CSF-contamination by FWE approach, respectively). FA (fractional anisotropy), RD (radial diffusivity), MWF (myelin water fraction), MMPF (macromolecular proton fraction), T_1 (longitudinal relaxation time), Fr (restricted diffusion), $\star\star\star$ (p <0.001) $\star\star$ (p <0.01), $\star$ (p <0.05), $^{+}$ (p <0.05 - does not pass FDR multiple comparisons).

	FA^u	RD^u	MWF^u	$MMPF^u$	T_1	Fr
FA^u		-0.68***	0.18	0.24	-0.34***	-0.067
RD^u			-0.15	-0.35**	0.31	-0.20
MWF^u				0.11	-0.60***	-0.20
$MMPF^u$					0.10	-0.067
${T_1}^u$						-0.067
	FA^c	RD^c	MWF^c	$MMPF^c$	T_1	Fr
FA^c		-0.77***	0.066	0.11	-0.40**	0.067
RD^c			0.071	-0.24	0.25	-0.067
MWF^c				-0.15	-0.62***	-0.067
$MMPF^c$					0.16	0.067

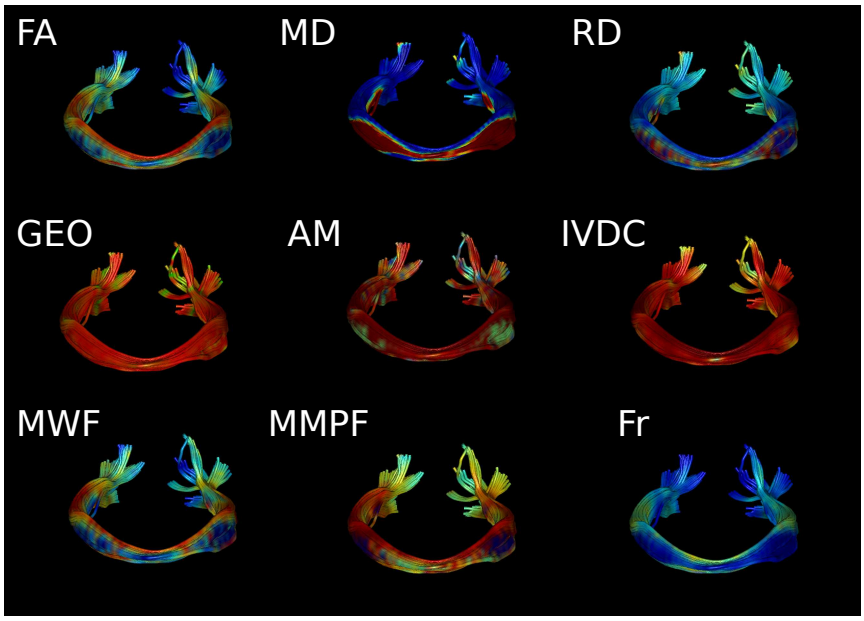

Figure 4.4: Tract-specific microstructural measurements or tractometry of the sCC. FA (fractional anisotropy), MD (mean diffusivity), RD (radial diffusivity), GEO (geometric image), AM (mode of diffusion), IVDC (intravoxel diffusion coherence), MWF (myelin water fraction), MMPF (macromolecular proton fraction), Fr (restricted diffusion).

Table 4.3: Statistical results for the UNC and the correlations between indices for 27 participants: Pearson coefficient (Superscripts 'u' and 'c' indicate the data are uncorrected or corrected for CSF-contamination by FWE approach, respectively). LS (left hemisphere), RS (right hemisphere), FA (fractional anisotropy), RD (radial diffusivity), MWF (myelin water fraction), MMPF (macromolecular proton fraction), T_1 (longitudinal relaxation time), Fr (restricted diffusion), $\star\star\star$ (p <0.001) $\star\star$ (p <0.01), $\star$ (p <0.05), $^{+}$ (p <0.05 - does not pass FDR multiple comparisons).

	Side	FA^u	RD^u	MWF^u	$MMPF^u$	T_1	Fr
FA^u	LS		-0.62***	0.07	0.17	-0.13	0.07
	RS		-0.57***	0.22	0.11	-0.11	-0.2
RD^u	LS			-0.17	-0.05	0.11	-0.2
	RS			-0.33*	-0.09	0.26	0.07
MWF^u	LS				-0.19	-0.62***	0.33
	RS				-0.01	-0.65***	0.20
$MMPF^u$	LS					0.16	-0.07
	RS					0.15	0.07
$T_1{}^u$	LS						-0.33
	RS						0.20
	Side	FA^c	RD^c	MWF^c	$MMPF^c$	T_1	Fr
FA^c	LS		-0.64***	0.07	0.06	-0.20	0.07
	RD		-0.63***	0.14	-0.002	-0.19	-0.07
RD^c	LS			-0.54	0.008	0.12	-0.06
	RD			-0.20	0.02	0.25	0.06
MWF^c	LS				-0.24	-0.70***	0.33
	RD				-0.16	-0.80***	0.20
$MMPF^c$	LS					0.12	0.07
	RD					0.16	0.2

Table 4.4: Statistical results for CST within the left hemisphere: Pearson coefficient (r), 95% CI (confidence interval), r bias (B) (how much it overestimates or underestimates the correlation).(Superscripts 'u' and 'c' indicate the data are uncorrected or corrected for CSF-contamination by FWE approach, respectively). FA (fractional anisotropy), RD (radial diffusivity), MWF (myelin water fraction), MMPF (macromolecular proton fraction), T_1 (longitudinal relaxation time), Fr (restricted diffusion), $\star\star\star$ (p <0.001) $\star\star$ (p <0.01), $\star$ (p <0.05), $^{+}$ (p <0.05 - does not pass FDR multiple comparisons).

	FA^u	RD^u	MWF^u	$MMPF^u$	T_1	Fr
FA		r=-0.97*** CI_{95}[-0.97,-0.96] B = 0.0009	r=0.19*** CI_{95}[0.12,0.26] B = -0.001	r=0.11*** CI_{95}[0.04,0.18] B = -0.0003	r=-0.16*** CI_{95}[-0.24,-0.08] B = 0.001	r=0.025 CI_{95}[-0.04,0.11] B = 0.005
RD			r=-0.16*** CI_{95}[-0.24,-0.09] B = 0.0008	r=-0.09** CI_{95}[-0.16,-0.03] B = 0.0002	r=0.16*** CI_{95}[0.08,0.25] B = -0.001	r=-0.03 CI_{95}[-0.10,0.03] B = 0.0007
MWF				r=0.46*** CI_{95}[0.41,0.51] B = -0.00009	r=-0.82*** CI_{95}[-0.85,-0.79] B = 0.0006	r=0.37*** CI_{95} [0.29,0.44] B = -0.00003
MMPF					r=-0.62*** CI_{95}[-0.66,-0.59] B = -0.0005	r=0.37*** CI_{95} [0.17,0.26] B = -0.0003
T_1						r=-0.43*** CI_{95}[-0.35,-0.26] B = 0.0006

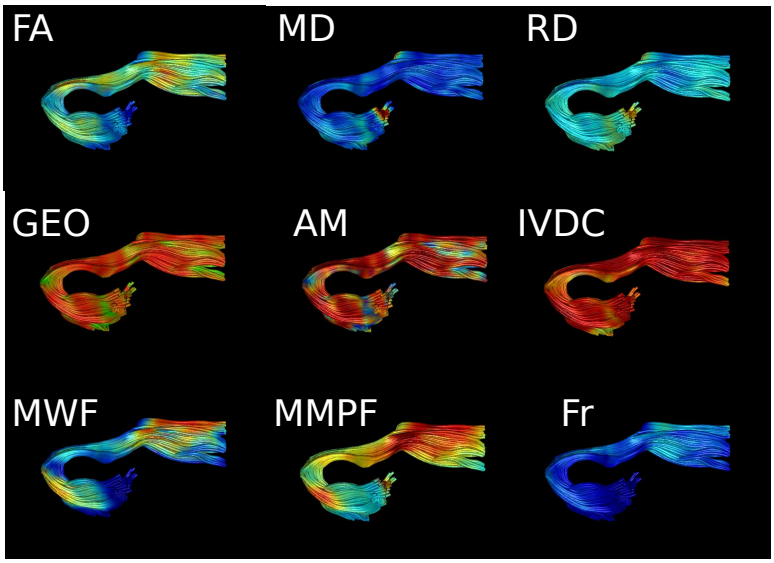

Figure 4.5: Tract-specific microstructural measurements or tractometry of the UNC. FA (fractional anisotropy), MD (mean diffusivity), RD (radial diffusivity), GEO (geometric image), AM (mode of diffusion), IVDC (intravoxel diffusion coherence), MWF (myelin water fraction), MMPF (macromolecular proton fraction), Fr (restricted diffusion).

throughout the whole tract than non-diffusion metrics (MWF, MMPF and Fr), which we attribute to the fact that FA is exquisitely sensitive to intra-voxel orientational dispersion whereas, to the best of our knowledge, Fr, MWF and MMPF are not. Figure 4.4 presents results for the splenium of the corpus callousm. As with the CST, MWF, MMPF, Fr and FA all decreased as the tract heads towards grey matter. The same metrics also decrease in the inferior section of the tract where it links the right and left hemispheres. Notably, the MD is high within this same area, which is in close proximity to the third ventricle suggesting that CSF contamination correction may not be perfect. Furthermore, the diffusion metrics, such as FA and AM, within the sCC do not appear to be more sensitive in areas of intra-voxel heterogeneity. Finally for the UNC, metrics MWF, MMPF and FA have similar patterns throughout the tract (Figure 4.5). All three metrics are lower as the tracts reach the grey matter and where the UNC bends in the area where it connects the temporal and frontal

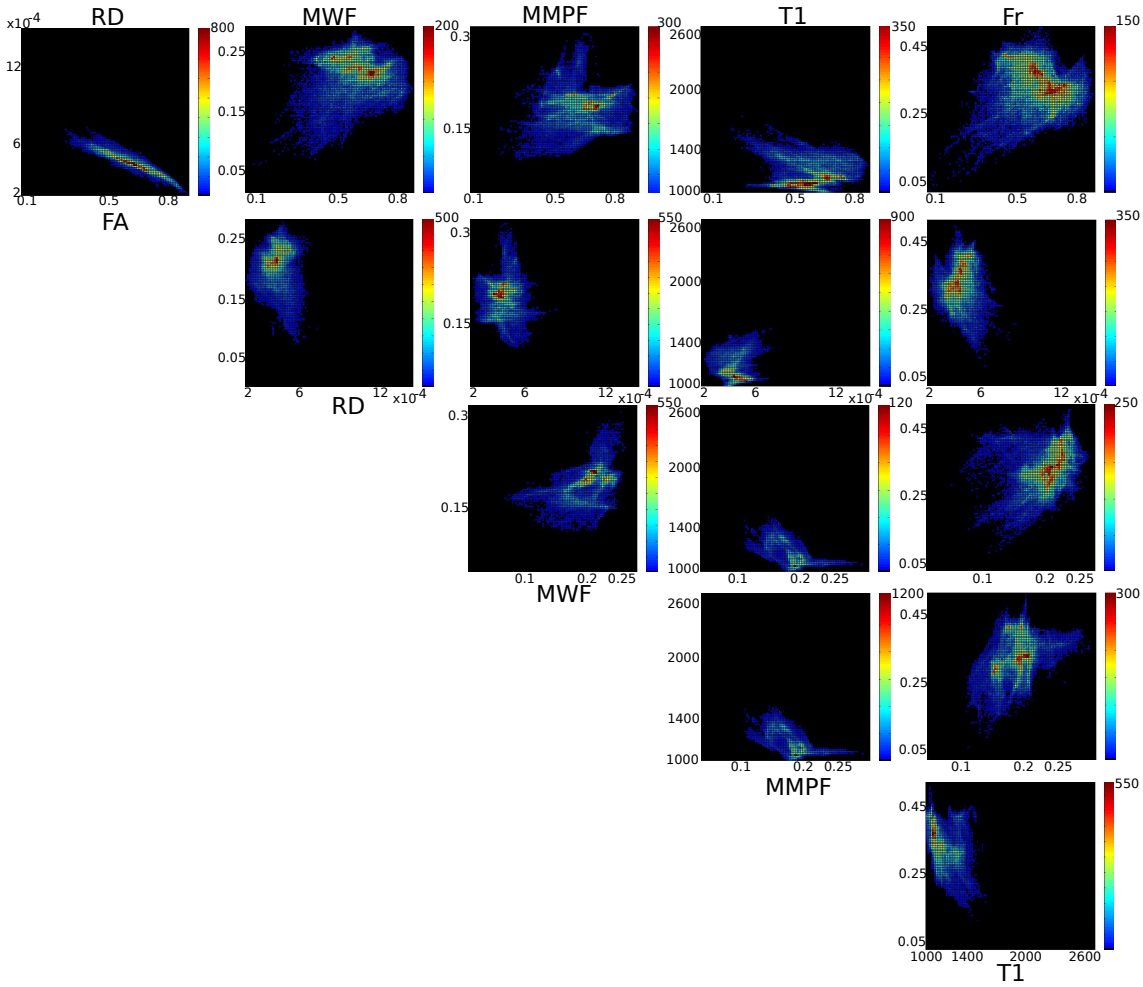

Figure 4.6: Histogram-scatter plots for the CST for different white matter metrics in one participant within all voxels demonstrating where majority of the voxels lie. FA (fractional anisotropy), RD (radial diffusivity), MWF (myelin water fraction), MMPF (macromolecular proton fraction), T1 (longitudinal relaxation time), Fr (restricted diffusion).

lobes. Within this mid-section, or where the UNC bends, the MD does not appear to increase, hence the decrease within the other white matter metrics is unlikely to be CSF partial volume artifact. The mode of anisotropy (AM) is heterogeneous throughout the tract and low especially in the mid-section of the UNC where the individual streamlines tend to fan suggesting that the low FA is most likely driven by crossing or kissing fibre configurations.

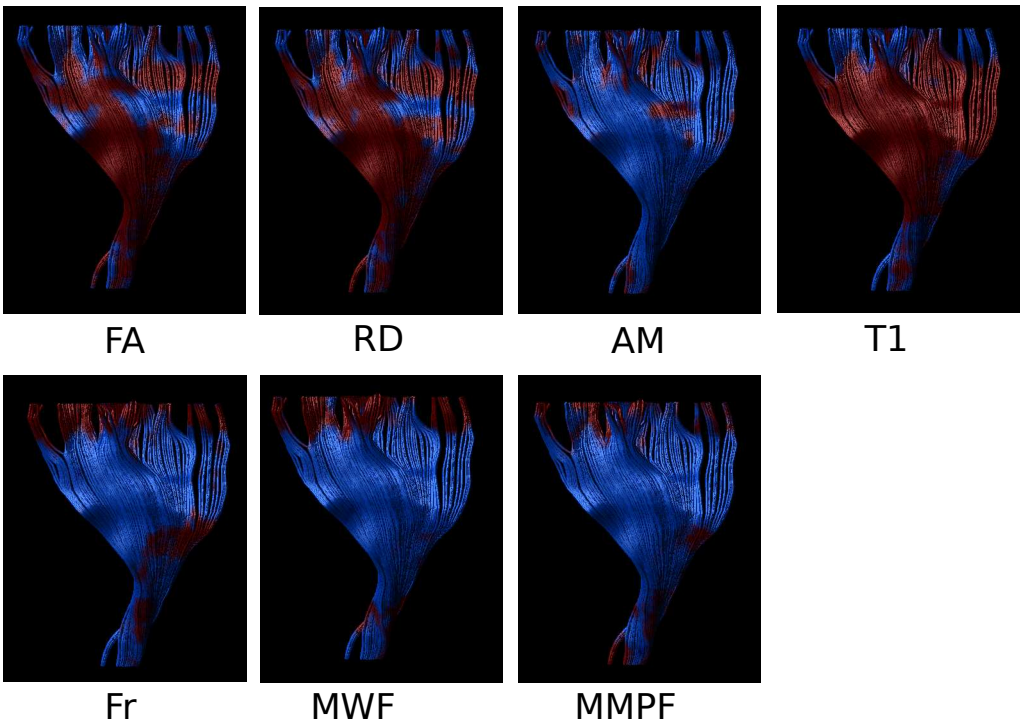

Figure 4.7: Reconstructed tracts illustrating high (blue) and low (red) white matter metrics within the left CST. FA (fractional anisotropy), RD (radial diffusivity), MWF from mcDESPOT (myelin water fraction), MMPF from qMT (macromolecular proton fraction), T_1 from mcDESPOT (longitudinal relaxation time), Fr from CHARMED (restricted diffusion).

For a more comprehensive comparison a single participant was used to illustrate the inter-correlations between the different white matter metrics within the left CST. Pair-wise Pearson correlations were computed between all metrics for the CST along with the confidence interval and corresponding bias (how much the correlation over

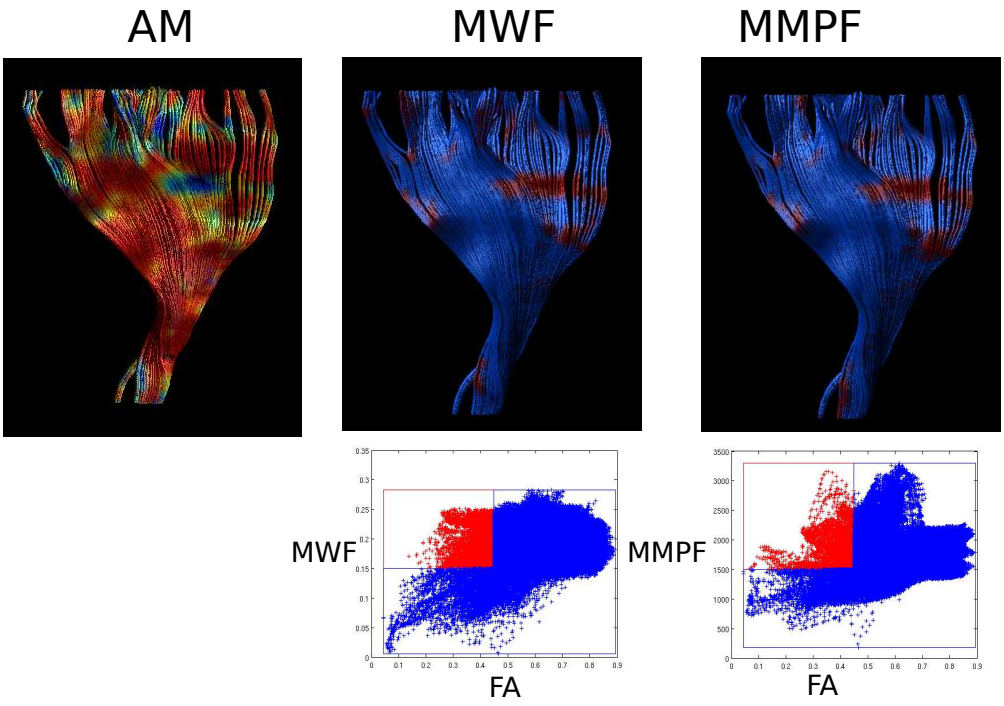

Figure 4.8: Reconstructed tracts illustrating the mode of anisotropy (AM) within CST and the correlations between FA versus MWF and FA versus MMFP. The scatter plots for both correlations are divided into two regions (1) low FA-high MWF or MMPF (reconstructed in red) (2) all other areas (reconstructed in blue) and then backprojected onto the CST tract.

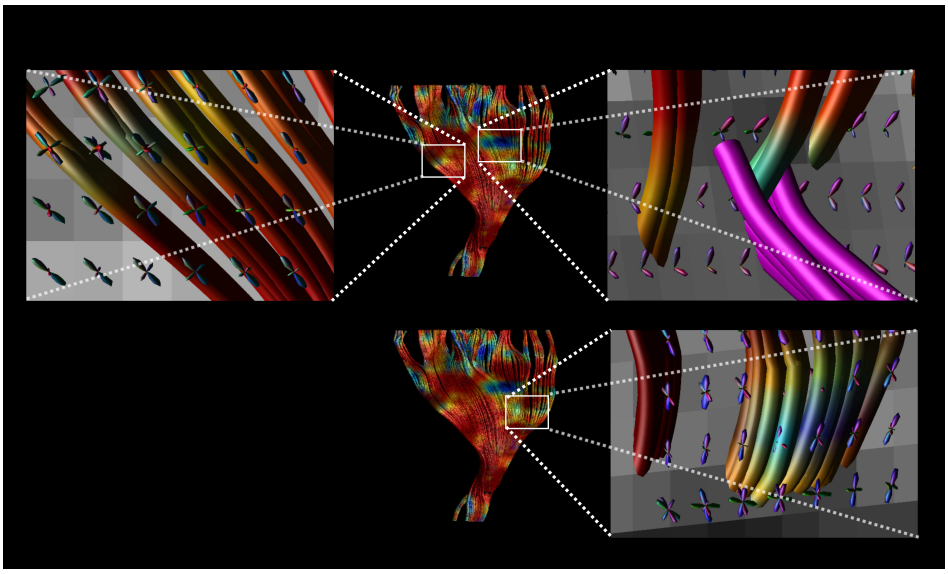

Figure 4.9: Reconstructed tracts illustrating the mode of anisotropy (AM) within CST, where three region of interest (ROI) are drawn in regions of low AM and HARDI glyphs are illustrated. ROI on the top left demonstrates more than one dominant fibre through HARDI glyphs and the reconstruction of a crossing-fibre drawn in purple. The other two ROIs also illustrate that area of low AM clearly have multiple fibres crossing the voxel.

or underestimates the estimation of r) (Table 4.4). If we consider correlations above 0.3 to be significant, where at least the relationship between the variables can explain 9% of the variance the correlations that reached significance ($r > 0.3$ considered a medium effect size) (Cohen 1988), where an inverse relationship between FA and RD (r=-0.97), a positive relationship between MWF and MMPF ($r = 0.46$) and a positive between MWF and Fr (r=0.37) was seen. Furthermore, the following metrics were significantly negatively correlated with T_1: MWF (r=-0.82), MMPF (r=-0.62) and Fr (r=-0.44) (Table 4.4). Figure 4.6 shows histograms-scatter plots for all pairs of indices obtained from the CST. With the exception of FA vs RD (where a highly linear relationship is seen), all other joint histograms do not demonstrate a strong linear correlation between the two parameters, echoing the results from the Pearson correlation analysis obtained from the tract means.

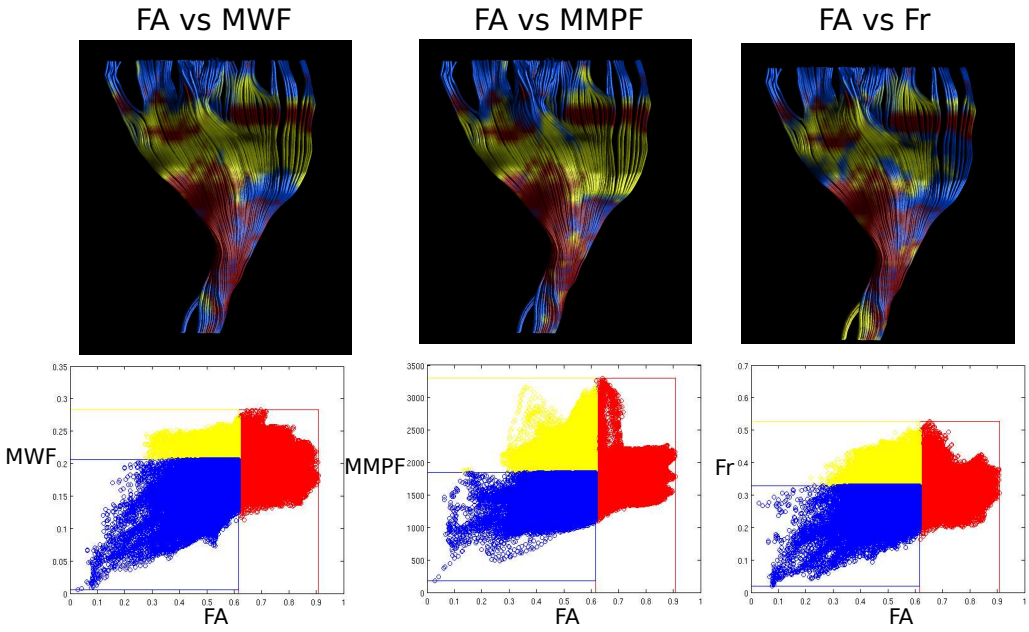

Figure 4.10: Reconstructed tracts illustrating correlations between fractional anisotropy (FA) versus myelin water fraction (MWF), FA versus macromolecular proton fraction (MMPF) and FA versus Fr. The scatter plots for all correlations are divided into three regions (1) high FA (reconstructed in red) (2) low FA and high white matter metric (MWF or MMPF) (reconstructed in yellow) (3) low-FA and low white matter metric (MWF or MMPF) (reconstructed in blue) and then backprojected onto the CST tract.

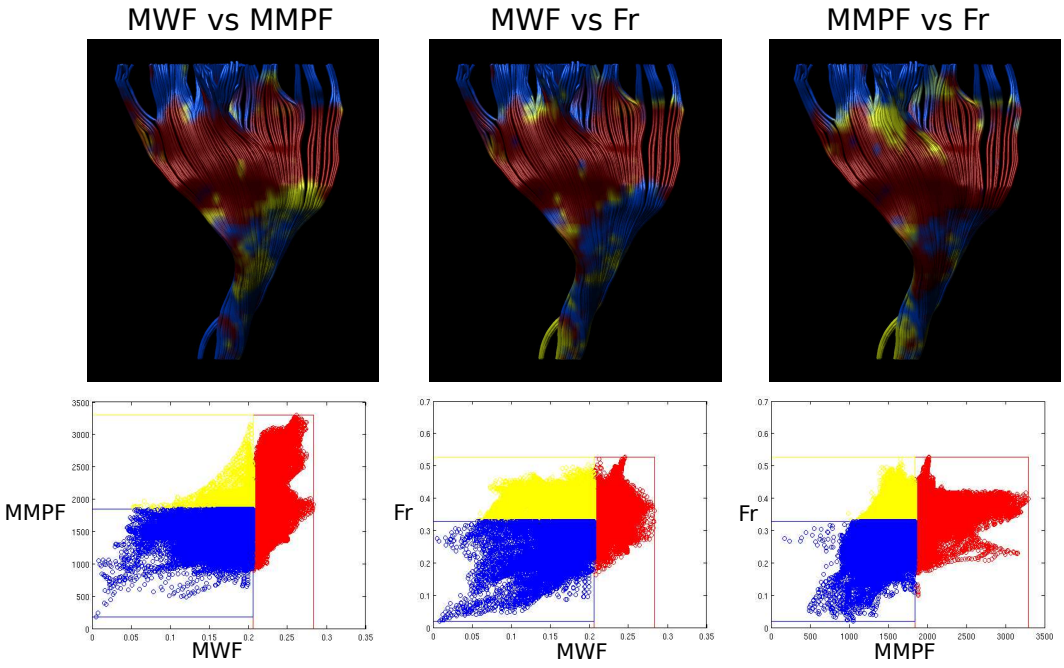

Figure 4.11: Reconstructed tracts illustrating correlations between myelin water fraction (MWF) versus macromolecular proton fraction (MMPF), MWF versus restricted diffusion (Fr) and MMPF versus Fr. The scatter plots for all correlations are divided into three regions (1) high WM metric (reconstructed in red) (2) low WM metric and high WM metric (reconstructed in yellow) (3) low WM metric and low WM metric (reconstructed in blue) and then backprojected onto the CST tract.

To explore the spatial distribution of each white matter metric further, each was divided into the upper and lower 50^{th} percentile and projected back onto the tracts. The results (Figure 4.7) demonstrate that the white matter metrics: MWF, MMPF and Fr all decrease as the white matter heads towards grey matter, while FA and RD appear to be more sensitive to areas of intra-voxel heterogeneity (tract curvature /dispersion) and are thus more heterogeneously distributed throughout the whole tract, than MWF and MMPF. Fr is less homogeneous than both MWF and MMPF particularly in areas where the tract narrows and heads towards the brain stem. Similarly, T_1 also increases in the same areas suggesting subtle changes in white matter microstructure. In areas where FA is low, but neither MWF nor MMPF decrease, the mode of anisotropy, AM, is low, suggesting that these areas contain one or more fibres that are crossing or kissing. To further explore the differences between these parameters, data points lying in the upper 50%-ile of MMPF /MWF and lower 50%-ile of FA are identified and projected back onto the tracts (Figure 4.8), where it is seen that the low FA/ high MWF and low FA/ high MMPF regions occupy very similar regions in the pathway. Interestingly, these areas correspond closely to the locations where AM is negative - areas of crossing or kissing fibres. To drive down further into this phenomenon, three ROIs are drawn and HARDI glyphs are reconstructed for the voxels within each ROI (Figure 4.9). In the first case it is clear that there are crossing fibres as demonstrated by the reconstructed crossing fibre plotted in purple. For the second and third ROIs, it is evident that in areas of low FA but high MWF or MMPF there is more than one fibre entering those voxels as seen through the HARDI glyphs. Thus, FA appears to be more sensitive to areas where crossing fibres are seen than other white matter metrics such as MWF and MMPF.

To further investigate the spatial distribution of different combinations of white matter metrics, each pair-wise scatter plot was subdivided into 3 separate domains: (i) Upper 50%-ile of FA; (ii) Lower 50%-ile of FA and upper 50%-ile of MWF/MMPF/Fr;

and (iii) Lower 50%-ile of FA and lower 50%-ile of MWF/ MMPF/Fr, and the data points lying within these domains were back-projected onto the tracts for visualization and interpretation (Figures 4.10). The spatial distributions thus obtained for the three metrics (MWF/ MMPF and Fr) are very similar to each other. Finally, Figure 4.11 shows a similar analysis for the relationship between non-DTI metrics.

4.4 Discussion

We studied white matter using diffusion-tensor MRI, CHARMED, quantitative magnetization transfer imaging and multi-component relaxometry, each of which has its strengths and limitations. Diffusion-weighted imaging is sensitive to changes in white matter structure, however it is not specific with regard to which microstructural subcomponent drives this change (i.e., myelin or axon diameter). CHARMED, on the other hand, collects data at multiple b-values and fits a two compartment model that aims to extract quantitative data from both extra- and intra-axonal water. It is assumed that the latter provides more specificity to change in axon properties. Quantitative magnetization transfer imaging using pulsed MT is sensitive not only to myelin, but also other semisolids within its macromolecular measurements. Despite the fact that the concentration of nonaqueous molecules is higher within myelin it has been shown that the magnetization transfer of myelin water is nine times more efficient than in the intermediate T_2 compartment demonstrating that the observed MT is mainly due to myelin (Stanisz et al. 1999). Myelin-water mapping, from multi-component T_2 imaging, characterizes myelin indirectly by measuring water trapped within the bilayer and inferring those changes as variations in myelin content. All these methods have been previously studied, but not all together within a group of participants along a specific white matter tract.

Diffusion tensor MRI-based tractography was initially used to reconstruct white matter pathways, but is limited in voxels that contain more than a single dominant fibre (Vos et al. 2012). Such limitations lead to recent developments into advanced diffusion weighted imaging methods such as high angular resolution diffusion (HARDI) (Frank 2001; Tuch et al. 2002; Wedeen et al. 2005) crossing fibres within voxels are able to be resolved allowing for a more detailed description of the tissue composition (Douaud et al. 2011). Combining the ability to distinguish crossing fibres using diffusion-weighted images and other more specific techniques that allow measure of myelin or axon diameter, such as quantitative magnetization transfer imaging, allows for a more details microstructure description along a specific white matter tract - termed '*Tractometry*'.

Tractometry is a powerful tool that combines the ability to distinguish crossing fibres using HARDI with quantitative white matter images to investigate the correlations between different white matter metrics. Results show that there was no or little correlation found between white matter microstructure measurements. Comparing the mean values of specific metrics along the splenium of corpus callosum, uncinate and cortico-spinal tracts resulted in FA and RD being highly correlated, as expected. Another significant correlation found was between MWF and T_1 in all three tracts. This is an interesting result and indicates that for a control participant population quantitative T_1 maps are adequate for a microstrucutral measure. However, this may not be the case for a clinical population when things like inflammation will affect these values differently. However, only for sCC a significant correlation between MMPF and RD and for the UNC a significant correlation between MWF and RD were found. These findings suggest that even in highly organized fibre arrangements like the sCC, high FA values do not directly correspond to higher degree of myelin content as measured in MWF and MMPF maps, demonstrating that intravoxel orientational coherence is the main factor driving regional variations in RD and

FA and myelin content or axonal density could play a peripheral role in these DTI parameters. Moreover, there are clearly some similarities between these microstructure measurements since correspondences between MWF or MTR/MMPF with diffusion metrics have been reported using multiple ROIs within different white matter structures (Mädler et al. 2002; Bells et al. 2007). Although, like in this research Underhill et al. (2009) found no correlation between DTI metrics, FA and RD, versus MMPF and Levesque et al. (2010) found no significant correlations between MMPF and MWF maps in MS human data. The reason for the differences among these findings may be because the two studies that found a significant correlation used multiple white-matter structures to measure correlation, thus increasing the range of observed values within the measures and the likelihood of finding a relationship. Instead of using ROIs another study used a voxel-based method to demonstrate a negative correlation between RD and MWF (Mädler et al. 2008). In our study, we found a very weak correlation between RD and MWF ($r \sim 0.2$ for CST) emphasizing that other factors such as fibre arrangements, packing, volume fraction and angular orientation distribution also play a major role in this relationship (Beaulieu and Allen 1994a; Beaulieu and Allen 1994b) and demonstrates that RD is over interpreted as a direct measure of myelin.

Focusing on the correlation calculations along a specific white matter tract - left CST, it was shown that there is little or no correlation when comparing the same metrics in a voxel-wise fashion. Areas of low FA found in the CST can be attribute to intra-voxel heterogeneity from dispersion, curvature or crossing-fibres. It has been previously found that in white matter areas with disorganized fibre bundles, or multiple fibre crossings, that low FA values could be found despite MWFs being high (Oouchi et al. 2007) as seen here in this experiment. Correlations between white matter metrics, such as MMPF and MWF, were weak indicating that they provide complementary information, but are mainly independent as suggested by others

(Tozer et al. 2005; Levesque et al. 2010). Stronger correlations have been seen between white matter measures in clinical populations (i.e. MS lesion), but this is most likely due to the larger variation in values measured between non-healthy white matter (increased severity within MS lesions) and healthy white matter (Tozer et al. 2005).

Despite the evidence of a strong relationship between myelination and white mater metrics (i.e. MTR, MWF) through animal research (Deloire-Grassin et al. 2000; Zaaraoui et al. 2008), confirming a similar relationship in humans is more challenging in humans since it requires post-mortem tissue. Histological measurements can be performed at 3 to 10 microns; conversely MRI is usually on the order of 1 mm. One study attempted to correlate DTI metrics with histological stains and found that RD was altered with demyelination, and axon injury (Klawiter et al. 2011). In our healthy subjects, we found no correlation between RD and white matter measurements like MWF or MMPF. Several studies have demonstrated strong correlations between MTR reduction and the amount of demyelination (Dousset et al. 1992; Deloire-Grassin et al. 2000; Barkhof et al. 2003; Schmierer et al. 2004; Schmierer et al. 2008), meanwhile others have shown a significant correlation between MTR and axonal density (Gass et al. 1994; van Waesberghe et al. 1999), while others have demonstrated both (Mottershead et al. 2003; Schmierer et al. 2007). In fixed brains a significant correlation ($r^2 = 0.6$) between FA and MWF in normal white matter was found in most structures (MacKay et al. 2006). This supports previous findings that FA is weakly modulated by myelin, but mostly dominated by intact axonal membranes (Beaulieu 2002). These studies all demonstrate the differences in magnetization transfer and multi-component relaxometry experiments, suggesting they measure slightly different mechanisms.

Previously there have been a number of research groups that have studied the differences between MWF and MMPF using postmortem or animal models. A few

have found that MWF is less sensitive to inflammation and edema than MMPF using human models (Moore et al. 2000). Inflammation will increase the amount of free water within the area thus affecting the MMPF since the semisolid protons including macromolecules, such as myelin, are independent of free water. Although we corrected for CSF contamination, we cannot prove with this experiment that it eliminated all CSF contamination. Even fewer have studied the relationship between MMPF/MTR and axonal changes. One group found a high correlation between MTR and axonal loss measured using retinal nerve fiber layer thickness, which is independent of the level of demyelination (Klistorner et al. 2011). Within the current research we cannot provide concrete evidence as to which measure is more specific to myelin, however there is a difference between the microstructure measures that are sensitive to different things and making both valuable to use in future studies.

Tractometry provides a comprehensive assessment of multiple microstructure metrics in a unique way - along specific white matter tracts. While it demonstrates promising results, there remains a few issues to be addressed before it is widely translated into clinical applications. Most importantly the concern regarding the specificity of all white matter measurements and how they are affected by changes of free water within a voxel as in inflammation. Where weak correlations between measurements are seen, these are driven by different mechanisms. Importantly, we find little correlation between proxy indices of myelination and axonal morphology, suggesting that additional complementary WM microstructural information is obtained with our approach.

Chapter 5

Exploring the Asymmetry in MRI measurements

5.1 Introduction

Asymmetric-hemispheric cognitive functionality is an important attribute of the human brain, generally referred to as lateralization (Geschwind and Galaburda 1985). It is believed that functional and structural asymmetry results from years of evolutionary interhemispheric specialization, such as language representation (Toga and Thompson 2003) and visuo-spatial processing (Corballis 1997; Vogel et al. 2003). Affirmation for left hemispheric dominance within language processing was first introduced by Broca (1861) with further evidence from lesion, functional and structural anatomical findings (Geschwind and Levitsky 1968; Geschwind and Galaburda 1985; Stephan et al. 2003; Toga and Thompson 2003). The ability to characterize the lateralization within white matter microstructure with MR provides potential insights into functional asymmetry (Büchel et al. 2004; Park et al. 2004; Stephan et al. 2007; Putnam et al. 2010; Wahl et al. 2010).

Diffusion MRI (Le Bihan et al. 1986; Moseley et al. 1990) has become one of the most popular techniques used by the neuroscientific community (Geschwind and Levitsky 1968; Geschwind and Galaburda 1985; Stephan et al. 2003; Toga and Thompson 2003). The principal source of contrast in diffusion tensor MRI is that axons (and its subcomponents) within white matter create coherent obstacles to diffusion, thus

creating an orientational dependency of the apparent diffusion coefficient (Moseley et al. 1990). In diffusion tensor MRI, this orientational dependence is modeled by a second-rank tensor assuming a uni-modal Gaussian displacement profile, and a diffusion tensor is fitted to the signals in each voxel (Basser et al. 1994b; Basser and Pierpaoli 1996). Tensor estimates provide scalar indices, such as the fractional anisotropy (FA) - a normalized index of the standard deviation of the eigenvalues that has a range of 0-1 (Basser and Pierpaoli 1996).

Due to the excellent sensitivity of diffusion tensor imaging to various sub-components of white matter at the microstructural level, it has been widely used as a tool to investigate white matter pathways, including their lateralization. Diffusion properties such as FA and the radial diffusivity (given by the average of the two smallest eigenvalues of the tensor, $\frac{1}{2}(\lambda_2 + \lambda_3)$) have been used to probe the language pathway and it was found to have a leftward asymmetry (Powell et al. 2006), meaning that the diffusion metrics (e.g. FA) in the left hemisphere tend to be larger than in the right. Differences in structural asymmetry of diffusion MRI metrics have been reported in a number of clinical populations. For example, Lange et al.(2010) reported increased rightward lateralization of the tensor skewness within autism compared to controls, and right temporal lobe epilepsy patients demonstrated increased ipsilateral FA-asymmetry to the seizure focus compared to left temporal lobe epilepsy patients (Ahmadi et al. 2009). In contrast, in studies of other clinical populations, differences in asymmetry are not always found. For example, Takao et al.(2010) found no difference in asymmetry of diffusion measurements between schizophrenia and controls.

One concern with clinical applications is that most diffusion studies do not take into account partial volume artifacts caused by cerebrospinal fluid (CSF) contamination, resulting in errors within diffusion parameters (Alexander et al. 2001; Metzler-Baddeley et al. 2012; Vos et al. 2011). Clearly, ignoring CSF contamination will inappropriately elevate diffusion indices, such as, principal eigenvalue (λ_1), radial dif-

fusivity (RD) and mean diffusivity (MD), whereas it will inappropriately decrease fractional anisotropy (FA) (Alexander et al. 2001; Pfefferbaum and Sullivan 2003). This also has implications for the reconstruction of white matter pathways (Vos et al. 2011). Moreover, the location of a white matter pathway influences how vulnerable it is to CSF contamination. For example, periventricular pathways like the fornix and splenium / genu of the corpus callosum are more prone to CSF contamination (Concha et al. 2005; Jones and Cercignani 2010). Considering that CSF-contamination effects are heterogeneously distributed across the brain, there is no simple global correction that can be applied, e.g. scaling by intracranial volume. If it were the case that all structures were affected in the same manner, then asymmetry measurements would negate this artifact. However, as this is not the case, failing to correct for CSF contamination may also affect assessment of microstructural lateralization.

A number of groups have proposed methods to correct for CSF-contamination. In one approach, CSF contamination is corrected by fitting the diffusion-weighted signal to a two-compartment model: tissue and CSF (Pierpaoli and Jones 2004). However, this approach requires the collection of additional diffusion-weighted data at various b-values, resulting in increased scan time. Alternatively, the 'Free Water Elimination' (FWE) approach proposed by Pasternak et al.(2009) uses a single b-value diffusion acquisition and fits two compartments: tissue and CSF. This approach is able to estimate CSF contamination on conventional diffusion MRI data (i.e. single b-value or single shell (Jones et al. 1999)) by imposing local smoothness constraints on the tissue compartment and using a regularisation term to estimate the tissue volume fraction, V_f, (i.e., the fraction of the signal that is attributed to tissue), and to provide diffusion metrics that are corrected for CSF-contamination.

One concern with DT-MRI derived metrics such as fractional anisotropy (FA) and radial diffusivity (RD), is that they are not straightforward to interpret - as they are influenced by various microstructural properties including axonal density and di-

ameter, myelination and the intravoxel architectural configuration (Beaulieu 2002). Consequently, these measures are very sensitive, albeit very non-specific indices of tissue microstructure. Other quantitative microstructural imaging methods, such as quantitative magnetization transfer imaging (Henkelman et al. 1993; Sled and Pike 2001; Ramani et al. 2002) and multi-component T_2 relaxometry (MacKay et al. 1994; Deoni et al. 2008; Deoni et al. 2008) provide greater specificity to a particular subcomponent of the tissue microstructure (in this case, myelin), compared to conventional diffusion-weighted imaging. If functional lateralization occurs in tandem with structural lateralization, and there are accompanying differences in myelination, then using these more specific markers may accordingly provide new insights into the inter-hemispheric distribution of white matter attributes.

Magnetisation transfer (MT) imaging harnesses contrast based on the exchange of magnetization between macromolecular and water protons, providing a measure of the relative density of macromolecules within the brain (such as protein, lipids and cellular membranes) that are invisible to conventional T_1-weighted and T_2-weigthed scans on account of their short relaxation times (Wolff and Balaban 1989; Wolff et al. 1991; Kucharczyk et al. 1994; Samson et al. 2006). MT parameters, such as MMPF, have been shown to provide valid biomarkers for white matter pathologies such as; inflammation, demyelination and axonal loss (Stanisz et al. 1999; Sled and Pike 2001; Stanisz et al. 2004).

Multi-component relaxometry (MCR) exploits the fact that different liquid subpopulations have unique relaxation times to provide detailed information on the brain's microstructure, including myelin water. Dividing the signal from the myelin water by the signal from total water gives a metric known as the myelin water fraction (MWF) (MacKay et al. 1994), which is commonly regarded as a marker of myelin in white matter. Comparison studies between MWF and histological-derived estimates using Luxol fast blue showed that changes in MWF and changes in ac-

tual myelin are highly correlated (Moore et al. 2000; Laule et al. 2006; Laule et al. 2008). Furthermore, it has been shown that MWF is unaffected by inflammation in histological-derived estimates using hematoxylin and eosin (inflammation) (Gareau et al. 2000). MWF has been used to measure changes in white matter microstructure due to lesions and MS (Vavasour et al. 1998; Whittall et al. 2002; Laule et al. 2004).

The aim of this study was to measure asymmetry within different white matter metrics. We combine for the first time a number of different quantitative white matter metrics including those derived from diffusion tensor MRI and from qMT and MWF, to address the question of whether more specific white matter metrics provide a more specific characterization of microstructural asymmerty than diffusion-weighted measurements alone. First, we examine the asymmetry within specific white matter pathways, reconstructed using tractography. For this part of the study, we focused on a number of tracts known for their asymmetry within diffusion or structural measures (Thiebaut de Schotten et al. 2011): arcuate fasciculus (AF), Cingulum (Ci), Inferior-Fronto-Occipital Fasciculus (IFO), Inferior Longitudinal Fasciculus (ILF), Uncinate Fasciculus (UF) and Optic Radiation (OpR). Secondly, we adopted a whole brain approach to look for asymmetry on a voxel-by-boxel basis using tract-based spatial-statistics (TBSS) (Smith et al. 2006). Finally, we studied the impact of performing Pasternak's free water elimination (FWE) correction for CS-contamination on asymmetry, on both the tract-based and voxel-based analyses.

5.2 Material and Methods

5.2.1 Participants

A total of twenty-one healthy right-handed female participants (mean age= 36.7±4.0 y) were included in this study. Informed consent was obtained prior to scanning and

the study was performed with ethics approval from the ethics review board at our institution.

5.2.2 MR Imaging acquisition

MRI data were acquired on a 3 T General Electric HDx MRI system (GE Medical Systems, Milwaukee, WI) with an eight channel receive coil (Medical Devices). Three different MRI scans were acquired: diffusion-weighted, magnetization transfer and mcDESPOT. Please refer to Chapter 4 for specific acquisition parameters and pre-processing steps for each MRI technique (DTI, qMT and mcDESPOT)- including details on registration of each white matter microstructure index and partial volume correction for myelin water fraction (MWF) and macromolecular proton fraction (MMPF).

5.2.3 Tract-specific Asymmetry

Asymmetry in tract-specific mean values was assessed for the following indices: corrected FA^c, MD^c, λ_1^c, RD^c, MWF^c $MMPF^c$ and V_f tissue volume calculated from FWC analysis and uncorrected FA^u, MD^u, λ_1^u, RD^u, MWF^u and $MMPF^u$ (where c and u are used to indicate CSF-contamination corrected metrics, and uncorrected, respectively). Left/right asymmetry was examined using a two-tailed paired t-test using mean tract values, preceded by a one-sample Kolmogorov-Smirnov test to check for Gaussianity. The t-tests compared right against left, so that a negative T-statistic means that the left is larger than the right. The results were then adjusted for multiple comparisons using the false discovery rate (FDR) approach (5%) (Benjamini and Hochberg 1995). Next, an asymmetry index was computed between tracts in the right hemisphere (RH) and left hemisphere (LH) for all the tracts under investigation for all participants (Asymmetry Index = 2(RH-LH)/(LH+RH)), resulting in a lat-

eralization measure for each individual participant. To assess asymmetry across the twenty-one participants a group lateralization index was calculated (Lateralization Index=(# of participants with rightward lateralization - # with left lateralization)/(# with rightward lateralization + # with leftward lateralization)) for each tract under investigation: AF, Ci, IFO, ILF, UNC and OpR. Statistical significance was tested using a one-sample t-test and was then adjusted for multiple comparisons using the false discovery rate (FDR) approach (5%).

5.2.4 Voxel-Based Asymmetry Analysis

Whole brain left/right asymmetry assessments for each metric (FA, MD, λ_1, RD, MWF, MMPF and V_f) were performed using tract-based spatial statistics (TBSS) (Smith et al. 2006) using a study specific template. Following the standard skeletonization of the mean FA, a threshold of FA>0.2 was applied to only include major white matter pathways and ignore the peripheral pathways with higher inter-participant variability and make the skeleton less sensitive to CSF contamination. The FA skeleton was then symmetrised and all remaining metrics were projected onto this skeleton. For each skeleton voxel, the difference between the left and right hemisphere was computed, resulting in asymmetry measures (results for left >right and right >left). Voxel-based analysis for each metric was carried out using randomize (Nichols and Holmes, 2002) a permutation-based unpaired t-test (5000 permutations) with threshold cluster enhancement (TFCE) (Smith and Nichols 2009) for each index. Asymmetry was considered significant when the p-value was <0.05 after correction for multiple comparisons.

5.3 Results

5.3.1 Hemispheric asymmetries using Tractography

Interhemispheric differences for all indices for the reconstructed tracts are shown in Figure 5.1 with their corresponding t-statistic and p-value presented in Table 5.1. Figure 5.1(A) shows the lateralization index for all white matter metrics along the AF. A significant leftward asymmetry was found across most of the white matter measurements for the arcuate fasciculus (AF), with the exception of FA and MMPF. A trend for leftward lateralization was found within MMPF the lateralization was not significant after correcting for multiple comparisons. Importantly, after performing the correction for CSF-contamination, some asymmetries were preserved (λ_1, RD, MD), while the asymmetry for MMPF become significant even after multiple-comparison correction. Furthermore, a significant rightward distribution was found for the tissue-volume fraction (V_f) ($T_{(20)} = 4.0$, $p = 0.0021$).

Table 5.1: Statistical results for each tract and index: Kolmogorov-Smirnov test, pairwise t-test between left/right tracts and one-sample t-test for lateralization index (LI). (Superscripts 'u' and 'c' indicate the data are uncorrected or corrected for CSF-contamination by FWE approach, respectively). FA(fractional anisotropy), MD(mean diffusivity), λ_1 (longitudinal diffusivity), RD (radial diffusivity), $\star\star\star$ (p <0.001) $\star\star$ (p <0.01), $\star$ (p <0.05), $^+$ (p <0.05 - does not pass FDR multiple comparisons).

Tract	Index	K-S test [LS,RS]	LS-RS t-test	LI t-test
AF	FA^u	$[0.65,0.65]^{\star\star\star}$	0.76	0.76
	FA^c	$[0.66,0.66]^{\star\star\star}$	0.19	0.86
	$\lambda_1{}^u$	$[0.50,0.50]^{\star\star\star}$	$-2.93^{\star}$	$-2.95^{\star}$
	$\lambda_1{}^c$	$[0.50,0.50]^{\star\star\star}$	$-2.52^{\star}$	$-2.54^{\star}$
	MD^u	$[0.50,0.50]^{\star\star\star}$	$-5.04^{\star\star\star}$	$-4.91^{\star\star\star}$
	MD^c	$[0.50,0.50]^{\star\star\star}$	$-5.80^{\star\star\star}$	$-5.69^{\star\star\star}$
	RD^u	$[0.50,0.50]^{\star\star\star}$	$-3.20^{\star\star}$	$-3.16^{\star}$

Continued on next page

Table 5.1 – continued from previous page

Tract	Index	K-S test [LS,RS]	LS-RS t-test	LI t-test
	RD^c	[0.50,0.50]***	-2.90*	-2.89*
	$MMPF^u$	[0.54,0.54]***	-2.14$^+$	-2.16$^+$
	$MMPF^c$	[0.54,0.54]***	-2.72*	-2.76*
	MWF^u	[0.58,0.58]***	-8.47***	-7.10***
	MWF^c	[0.58,0.58] ***	-7.11***	-8.46***
	V_f	[0.82,0.82]***	3.95**	3.98**
Ci	FA^u	[0.63,0.64]***	-5.30***	-5.49***
	FA^c	[0.64,0.65]***	-5.50***	-5.69***
	${\lambda_1}^u$	[0.50,0.50]***	-6.53***	-6.57***
	${\lambda_1}^c$	[0.50,0.50]***	-7.03***	-7.13***
	MD^u	[0.50,0.50]***	-1.68	-1.69
	MD^c	[0.50,0.50]***	-2.43*	-2.41*
	RD^u	[0.50,0.50]***	2.46*	2.53*
	RD^c	[0.50,0.50]***	4.38***	4.31***
	$MMPF^u$	[0.53,0.53]***	-3.27**	-3.30**
	$MMPF^c$	[0.54,0.54]***	-3.39**	-3.48**
	MWF^u	[0.56,0.57]***	-5.78***	-5.29***
	MWF^c	[0.57,0.57]***	-5.51***	-5.58***
	V_f	[0.81,0.81]***	0.89	0.89
IFO	FA^u	[0.66,0.66]***	-1.31	-1.34
	FA^c	[0.67,0.67]***	-1.76	-1.77
	${\lambda_1}^u$	[0.50,0.50]***	-2.03	-2.04
	${\lambda_1}^c$	[0.50,0.50]***	-2.76$^+$	-2.75$^+$
	MD^u	[0.50,0.50]***	-0.73	-0.81
	MD^c	[0.50,0.50]***	-0.995	-1.04
	RD^u	[0.50,0.50]***	0.29	0.17
	RD^c	[0.50,0.50]***	0.83	0.75
	$MMPF^u$	[0.54,0.54]***	-1.75	-1.74
	$MMPF^c$	[0.54,0.54]***	-2.34$^+$	-2.24$^+$
	MWF^u	[0.57,0.57]***	-3.29*	-2.85$^+$
	MWF^c	[0.57,0.57]***	-2.80$^+$	-3.24$^+$
	V_f	[0.80,0.81]***	0.87	0.83
ILF	FA^u	[0.65,0.64]***	1.15	1.16
	FA^c	[0.65,0.64]***	0.81	0.82
	${\lambda_1}^u$	[0.50,0.50]***	-3.02*	-3.06*
	${\lambda_1}^c$	[0.50,0.50]***	-2.42$^+$	-2.47*
	MD^u	[0.50,0.50]***	-4.92***	-5.03***
	MD^c	[0.50,0.50]***	-5.40***	-5.48***
	RD^u	[0.50,0.50]***	-2.97*	-3.04*
	RD^c	[0.50,0.50]***	-2.21$^+$	-2.22$^+$

Continued on next page

Table 5.1 – continued from previous page

Tract	Index	K-S test [LS,RS]	LS-RS t-test	LI t-test
	$MMPF^u$	[0.54,0.53]***	0.94	1.14
	$MMPF^c$	[0.55,0.54]***	0.51	0.72
	MWF^u	[0.55,0.54]***	0.29	0.89
	MWF^c	[0.57,0.55]***	0.76	0.47
	V_f	[0.81,0.81]]***	4.56***	4.5]***
UNC	FA^u	[0.65,0.63]***	0.64	0.58
	FA^c	[0.66,0.64]***	1.11	1.05
	${\lambda_1}^u$	[0.50,0.50]***	3.95**	2.28^+
	${\lambda_1}^c$	[0.50,0.50]***	3.92**	2.71^+
	MD^u	[0.50,0.50]***	2.65*	1.69
	MD^c	[0.50,0.50]***	4.02**	2.17^+
	RD^u	[0.50,0.50]***	0.94	0.75
	RD^c	[0.50,0.50]***	0.61	0.49
	$MMPF^u$	[0.53,0.53]***	-0.14	-0.06
	$MMPF^c$	[0.53,0.53]***	0.30	0.17
	MWF^u	[0.55,0.55]***	-2.51*	-1.44
	MWF^c	[0.55,0.55]***	-2.86*	-1.29
	${V_f}^u$	[0.80,0.80]***	-2.84*	-1.70
OpR	FA^u	[0.67,0.67]***	0.040	-0.03
	FA^c	[0.68,0.68]***	-0.512	-0.60
	${\lambda_1}^u$	[0.50,0.50]***	-4.64***	-4.68***
	${\lambda_1}^c$	[0.50,0.50]***	-4.70***	-4.78***
	MD^u	[0.50,0.50]***	-4.21**	-4.29**
	MD^c	[0.50,0.50]***	-4.80***	-4.89***
	RD^u	[0.50,0.50]***	-2.65*	-2.73*
	RD^c	[0.50,0.50]***	-1.98	-2.03
	$MMPF^u$	[0.54,0.54]***	-0.40	-0.51
	$MMPF^c$	[0.54,0.54]***	-1.11	-1.19
	MWF^u	[0.57,0.58]***	0.14	0.16
	MWF^c	[0.57,0.58]***	-0.95	-0.91
	V_f	[0.81,0.80]***	2.99*	2.98 *

A statistically significant leftward asymmetry was found within the cingulum for the following white matter metrics: FA, λ_1, MWF and MMPF, while, a significant rightward distribution was found for RD (Figure 5.1 B and Table 5.1). After correction for CSF-contamination and differences in tissue-volume fraction, some asym-

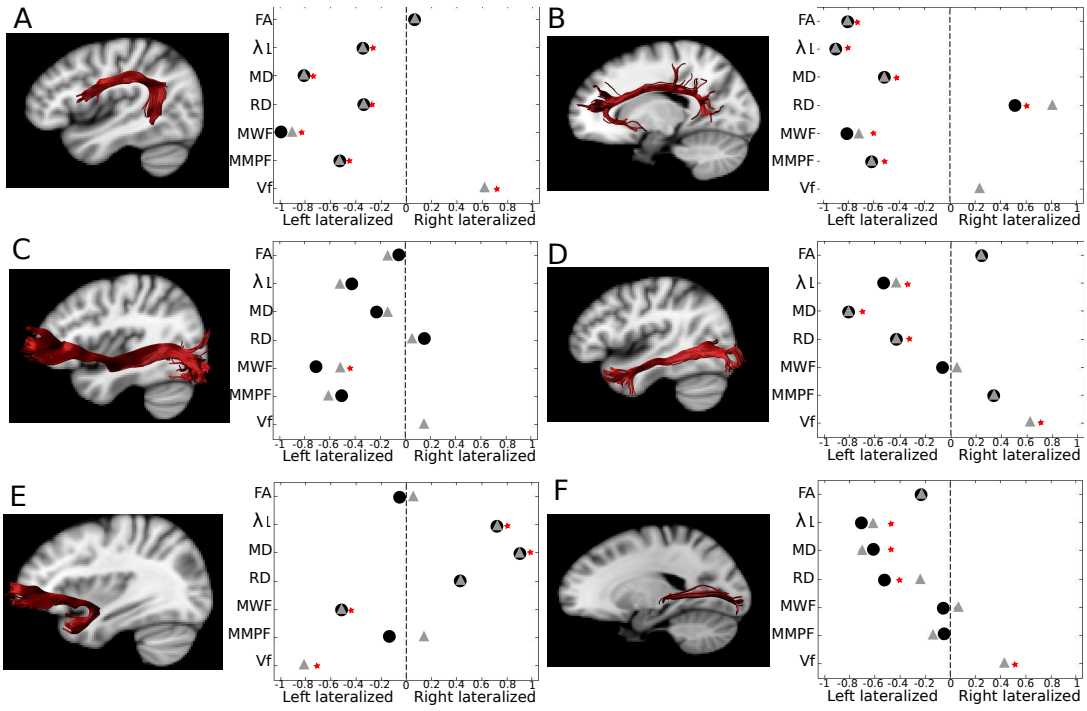

Figure 5.1: Lateralization index for fractional anisotropy (FA), principal eigenvalue (λ_1/L1), mean diffusivity (MD), radial diffusivity (RD), myelin water fraction (MWF), macromolecular proton fraction (MMPF) and tissue volume V_f for the following pathways: (A) Arcuate (B) Cingulum (C) Inferior fronto-occipital (D) Inferior longitudinal (E) Uncinate (F) Optic radiation. Where $\triangle$ for corrected indices and $\bullet$ for uncorrected indices and $\star$ represents significant ($p < 0.05$) t-test results after correction for multiple comparisons.

metries were preserved (FA, λ_1, RD, MMPF, MWF), while a significant leftward asymmetry for MD appeared ($p = 0.029$). Furthermore, there was no significant lateralization found within the volume tissue fraction for the cingulum (Table 5.1).

For the inferior-fronto occipital fasciculus, most metrics failed to show asymmetry either before or after CSF-contamination (Figure 5.1C and Table 5.1), with the exception of CSF-contamination-corrected MWF, which showed a leftward lateralization. (Asymmetry in MWF^{u} was insufficiently significant to survive multiple-comparison correction).

In the inferior-longitudinal fasciculus (ILF), a significant left lateralized asymmetry was found for λ_1, MD and RD (Figure 5.1D and Table 5.1). After correction for CSF-contamination, the MD asymmetry was preserved, while the asymmetry within both λ_1 and RD disappeared since they did not survive multiple comparison correction. Asymmetry was not found within MMPF and MWF either with or without CSF-contamination correction. Furthermore, a significant rightward distribution was found for the tissue-volume fraction (V_f) ($T_{(20)} = 4.6$, $p = 0.0008$).

The uncinate fasciculus (UNC) showed differences between the two hemispheres at varying degrees of lateralization. Significant rightward lateralization was found for λ_1 and MD white matter microstructure measurements (Figure 5.1E and Table 5.1). Conversely, a significant leftward lateralization was found for MWF ($T_{(20)} = -2.5$, $p = 0.039$). After correction for CSF-contamination and differences in tissue-volume fraction, all asymmetries were preserved (λ_1, MD and MWF). Furthermore, a significant leftward distribution was found for the tissue-volume fraction (V_f) ($T_{(20)} = -2.84$, $p = 0.0026$).

Finally, a significant leftward asymmetry was found in the optic radiation for the following white matter metrics: λ_1, MD and RD (Figure 5.1F and Table 5.1). After correction for CSF-contamination, some asymmetries were preserved (λ_1 and

MD), while the asymmetry for RD disappeared. Furthermore, a significant rightward distribution was found for the tissue-volume fraction (V_f) ($T_{(20)} = 3.0$, $p = 0.0019$).

Overall for all the tracts in this study we found no significant differences between lateralization measurements between tracts corrected and uncorrected for CSF contamination, using a paired t-test. Within each participant, the typical coefficient of variation in any diffusion-MR-based metric (FA, λ_1, RD and MD) along any of the tracts studied was in the range of 1-8%. For MMPF and MWF, the range was slightly larger (7-15%).

5.3.2 Asymmetry: Whole brain Tract Based Spatial Statistics

Results from whole brain voxel-wise (TBSS) asymmetry assessments clearly demonstrate a significant ($p < 0.05$, threshold-free cluster enhancement (TFCE) corrected, see Figure 5.2) left lateralization in all metrics along many of the white matter tracts studied earlier, while both FA and V_f also demonstrate a significant amount of right lateralization. Comparing voxel-wise to tracts based measures of pathways such as, AF, Ci, IFO and OpR, demonstrates that both provide evidence for a significant leftward asymmetry. However, for other tracts such as, UNC and ILF there is little evidence of asymmetry found within voxel-based measures. Notably, V_f demonstrated a significant leftward lateralization within frontal and temporal lobe white matter areas and a significant rightward lateralization within parietal and occipital lobe white matter. Thus, the data suggest that partial volume contamination due to free water is significantly different in frontal and posterior areas of the white matter when comparing hemispheres using this technique, and may therefore confound assessments of tracts, particularly of asymmetry in these regions. Treating the voxels showing a leftward asymmetry in tissue volume fraction, V_f, as 'waypoints' to filter whole brain tractography results, led to three major association pathways being reconstructed:

the uncinate fasciculus (UNC), the inferior fronto-occipital (IFO) fasciculus and the inferior longitudinal fasciculus (ILF) (Figure 5.3). This has implications when studying these particular tracts, particularly when studying asymmetry or when using the values in the contralateral hemisphere as a control.

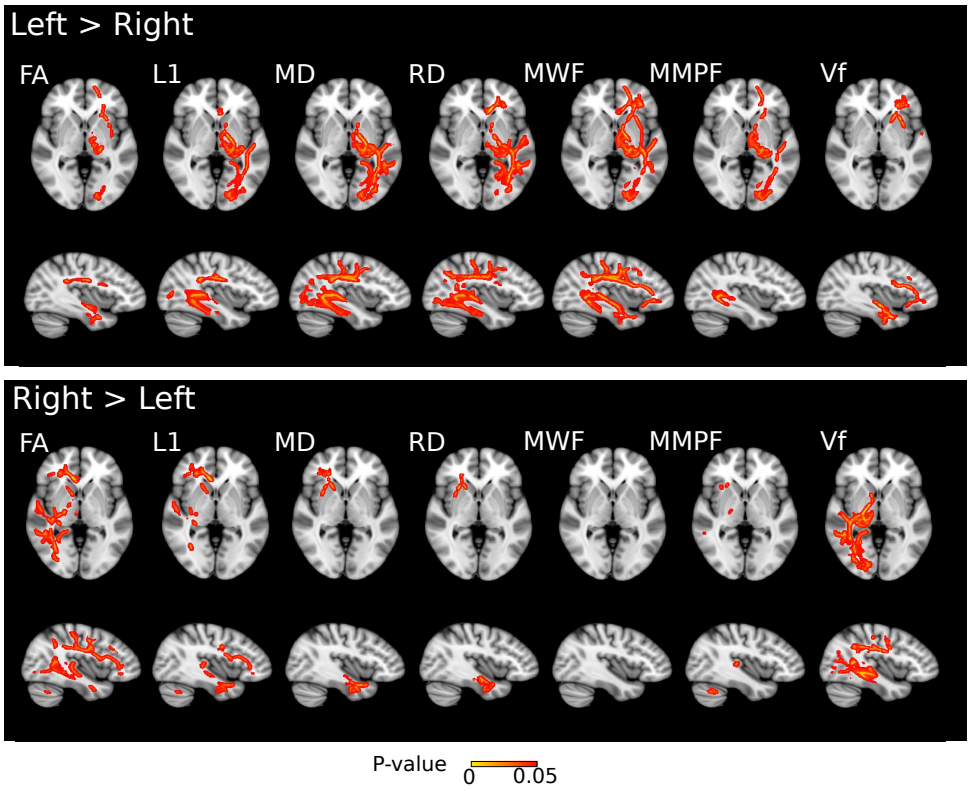

Figure 5.2: Significant voxel-wise asymmetries in diffusion metrics across the whole brain (Radiological convention): Results are thresholded at p <0.05, TFCE corrected. Asymmetries in all white matter metrics are shown: FA, MD, RD, λ_1/L1, MWF and MMPF, along with the asymmetry within the tissue volume fraction (V_f). For interpretive purposes, the statistical maps are overlaid on the T_1-weighted structural scan in MNI space.

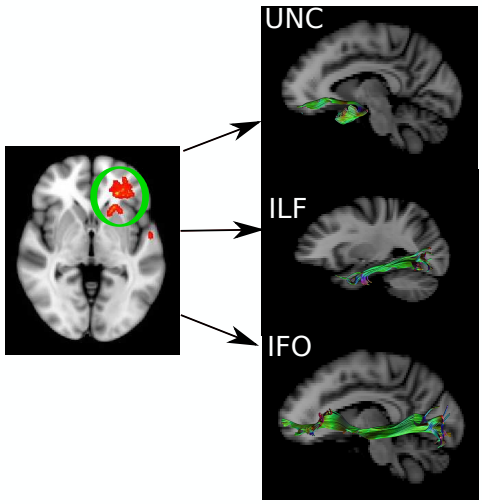

Figure 5.3: Significant voxel-wise asymmetry (left greater than right) within the tissue volume fraction (V_f) map (p <0.05) (left) and reconstructed white matter pathways when a waypoint is drawn around the significant FWC voxels.

5.4 Discussion

In this study we used tract-specific measures and voxel-based tract-based spatial statistics to study interhemispheric asymmetry in white-matter microstructure. Three main findings resulted from our research. First, white matter pathways such as the AF, Ci, ILF, OpR and UNC have more than one index that is left lateralized. Secondly, the non-diffusion metric MWF demonstrated a rightward lateralization within the UNC, opposite from RD (FA no lateralization was found). That is as myelination increases there will be an increase in hindrance to diffusion perpendicular to the main direction, so RD will go down. Finally, the tissue volume fraction was found to be selectively left lateralized in frontal and temporal areas and selectively right lateralized in parietal and occipital areas using voxel-wise analysis. Consistent with previous diffusion-MRI based neuroimaging studies (Büchel et al. 2004; Nucifora et al. 2005; Hagmann et al. 2006; Powell et al. 2006) a left lateralization was observed in our sample group of twenty-one healthy female adults.

The association between structural and functional lateralization are reflectant on differences in language and visuo-spatial processing and handedness. The most widely investigated tract, in terms of asymmetry, is the arcuate fasiculus (AF) (Ellmore et al. 2010), which connects cortical regions in the frontal, temporal and parietal lobes (Catani et al. 2007; Dronkers et al. 2007; Catani and Mesulam 2008). The horizontal portion of the AF runs in close proximity to parts of the superior longitudinal fasciculus (SLF) (Dejerine 1895), SLF II and III (Kaplan et al. 2010). With current diffusion-weighted *in vivo* techniques/methodology one cannot disentangle the three bundles within this area, thus most AF tracts will include some of the SLF II and III fibres. The AF is associated with language and asymmetric distribution of white matter microstructure may indicate increased 'connectivity' between the frontal and temporal lobes within the dominant hemisphere to support fluent language processes (Catani et al. 2007; Dronkers et al. 2007; Rodrigo et al. 2007; Catani and Mesulam 2008). Using a diffusion-based assessment of the AF/SLF in combination with fMRI (Powell et al. 2006; Vernooij et al. 2007) or cognitive assessment (Lebel and Beaulieu 2009) others have found a relationship between its leftward structural FA asymmetry and language lateralization. An increase in FA lateralization within the AF/SLF has been seen during development (Schmithorst et al. 2002; Barnea-Goraly et al. 2005; Lebel et al. 2008) and the adult population (Lebel and Beaulieu 2009), similarly this lateralization was seen in white matter density measures using T_1-weighted images (Paus et al. 1999). A leftward asymmetry was seen in many of our white matter metrics in the long segment of AF in agreement with previous in vivo DTI-tractography experiments using either fractional anisotropy or number of streamlines to measure lateralization (Nucifora et al. 2005; Hagmann et al. 2006; Eluvathingal et al. 2007; Lebel and Beaulieu 2009) and voxel-based analysis of T_1-images (Good et al. 2001). Notably, in our study we did not find evidence for asymmetry in FA. We note, however, that we studied a female population and our findings are completely in keeping

with those of Catani et al.(2007) who reported in their sample that asymmetry was only found in males.

The cinglulum (Ci) lies above the corpus callosum for a portion of its length connecting different areas that are part of the limbic system and is associated with the ability to process information, memory and executive function (Yu et al. 2008). Our results of a leftward lateralization from tractography of the anterior section of the cingulum are consistent with other studies that demonstrated lateralization in FA measurements using tractography (Park et al. 2004; Gong et al. 2005) and voxel-based statistics (Park et al. 2004). All microstructural metrics was significantly left lateralized (FA, λ_1, MD, MWF and MMPF) but one, with RD being right lateralized. On the other hand, a previous study demonstrated using the mean FA value along the entire Ci bundle, that FA appears to be symmetrically distributed (Thiebaut de Schotten et al. 2011) revealing potential functional differences between the anterior and posterior sections of the cingulum, in keeping with recent findings of Jones et al. (2012).

The uncinate fasciculus (UNC) links the anterior temporal lobe to the medial and lateral orbitofrontal lobe and may be associated with the ability to convey information about memory and semantic language (Lu et al. 2002; Rodrigo et al. 2007; Govindan et al. 2008). Primate electrophysiological and invasive tract tracing experiments suggest that the UNC is part of the ventral language pathway (network) (Romanski et al. 1999). Using DTI a study found that increased mean diffusivity (MD) within the left UNC relates to verbal memory deficits (McDonald et al. 2008). Furthermore, using histology the UNC was found to have a rightward asymmetry in size and number of axons (Highley et al. 2002). We found the tissue volume fraction (V_f) and MWF measured here to be significantly leftward lateralized, possibly being a simple reflection of the fact that V_f and MWF are not direct probes of axon morphology.

Other techniques, such as AxCaliber and CHARMED (Assaf and Basser 2005; Assaf et al. 2008), should represent or correlate better to axon measures *in vivo*.

Through cerebral cortex lesion studies, spatial processing has been shown to be functionally lateralized on the right (Vallar and Perani 1986). Furthermore, lesions within parietal lobe lead to neglect, which is the inability to process visual sensory information in one hemisphere and is more common when lesions occur in the right hemisphere. A number of tracts have been associated with visuo-spatial processing and neglect-related disorders, such as the SLF II, ILF and IFO. Visual-spatial performance has been shown to correlate with the degree of right-ward asymmetry of volume in the SLF II (Thiebaut de Schotten et al. 2011). The ILF has been shown to be associated with the ability to convey information about objects, faces and written words from neuroimaging studies (Mandonnet et al. 2007; Catani and Mesulam 2008; Epelbaum et al. 2008). Structural asymmetric measurements in controls found that a greater number of tracts reconstructed along the IFO are measured in the right hemisphere (Thiebaut de Schotten et al. 2011), which may portray a correlation between anatomical asymmetry and hemispheric dominance for visuo-spatial processing. However, here like in the previous study by de Schotten et al(2011) no significant lateralization was found within FA or other diffusion metrics for the IFO. For the ILF, it has been shown that FA within controls is left lateralized (Thiebaut de Schotten et al. 2011). In our study, however, for the ILF no significant lateralization within FA was found and left lateralization was only found in λ_1, RD and MD. Both of these results suggest that right-hemispheric asymmetry along the IFO and ILF is weak or small, unlike the dominance of left-hemispheric language-related processing (Corballis 1997).

The transfer of visual information to the visual cortex occurs along the optic radiation (OpR) and structural asymmetry measures from T_1-weighted images of tract volume show a leftward asymmetry within a right-handed females and males

(Bürgel et al. 1999), while diffusion-weighted measures demonstrated a leftward asymmetry within tract volume and a right-lateralization within FA measurements - with no statistical difference between the two genders (Thiebaut de Schotten et al. 2011). Here, using CSD to determine the orientation distribution function (fODF) for deterministic-tracking instead of tensor-based tracking we did not find a significant lateralization in FA, MWF or MMPF suggesting that tissue microstructure, in fact, is symmetrically represented in the visual system in females.

In this study, our voxel-based analyses demonstrated a leftward asymmetry in all white matter metrics as previously demonstrated in DTI measures (Gong et al. 2005; Thiebaut de Schotten et al. 2011). Overall, similar results were found between tract specific and voxel-based asymmetry. In both measurements a leftward asymmetry was found in the cingulum and arcuate fasciculus, while the other tracts studied (IFO, ILF, UNC) were not significantly lateralized along the entire tract within voxel-wise analysis. Using voxel-based analysis, Büchel et al. (2004) demonstrated that FA was higher within the AF of the hemisphere contralateral to the dominant hand (i.e. higher on the left for right handers) (Jahanshad et al. 2010). Similar to earlier studies we found a leftward asymmetry within FA measurements in the AF using voxel-based statistics (Büchel et al. 2004; Catani et al. 2007).

Interestingly, we demonstrate lateralization within volume fraction (V_f) suggesting that when comparing diffusion measurements for asymmetry, correction for CSF-contamination should be applied prior to measurements. We only calculated such an effect in a young control population and it is expected that this will be an exaggerated confound in an older population due to atrophy or in diseased populations (Metzler-Baddeley et al. 2012). To explore which white matter tracts can be affected by the leftward lateralization seen in frontal areas, waypoint ROIs were placed around significant leftward-asymmetric regions seen in the tissue volume fraction (V_f) map to reconstruct tracts. Three tracts, UNC, IFO and ILF, were reconstructed from

these ROIs (Figure 5.3). The same leftward asymmetry result was seen within our tract-specific measures of V_f along the UNC, however our tract-specific measure for V_f along ILF demonstrated a rightward asymmetry. This discrepancy may be due to the fact that it was only the anterior portion of the ILF that was more leftward asymmetric and the posterior portion of the ILF would be more rightward asymmetric (Figure 5.3).

In addition to our findings based on diffusion-derived metrics, we report, for the first time, asymmetry measurements within MWF and MMPF. These findings have high relevance for studies for multiple sclerosis that often compare, say, MWF between tissue affected by MS lesions and homologous regions in the contralateral hemisphere (Laule et al. 2004; MacKay et al. 2006). Importantly, if MWF is asymmetric and one uses two ROIs within separate hemispheres to interpret the difference between normal-appearing MWF and contralateral healthy tissue there is increased risk of misinterpretation. The estimated effect size for measuring the differences between a lesion and its contralateral healthy tissue is high (~ 0.98) (Laule et al. 2004), while the effect size for measuring differences between hemispheres is (~ 0.4) (estimated from Pearsons correlation r, where r $>$0.3 is considered to be a medium effect size according to (Cohen 1988)). Although the effect size is therefore larger when comparing differences between a lesion and its contraleral side its comparison should still take into account the influence of hemispheric differences. The full extent of the influence of asymmetry ROI based multi-hemispheric measurements on such studies should be further investigated.

Diffusion MRI tractography is currently the only MRI technique that allows the identification of large white matter pathways non-invasively. Nonetheless, it is important to note that diffusion measures are sensitive to differences in multiple tissue compartments and only an indirect index of tissue properties, and therefore not a specific measure of tissues biology (e.g.,myelination or axon diameter). Similar asym-

metric patterns among all white matter pathways and metrics under investigation were found. Pathways serving functions that are known to be lateralized, such as the arcuate fasciculus demonstrated a leftward structural lateralization. Interestingly we found a lateralization with the relative tissue volume fraction measured from diffusion-weighted images and in myelin water fraction. For tissue volume fraction maps a rightward lateralization was found in frontal white matter areas and a leftward lateralization was found in posterior white matter areas. This spatial heterogeneity of partial volume effects can potentially lead to implications in studies where contralateral hemispheres are used as an internal control regions of interest by either exacerbate the tissue difference or possibly negating it.

Chapter 6

Reproducibility in Tract-based Statistics

6.1 Introduction

Studies of non-invasive assessment of tissue microstructure, and how it impacts on function are becoming increasingly prevalent in the neuroimaging literature (Johansen-Berg and Rushworth 2009). White matter pathways form connections between cortical regions to form distributed networks. The ability to characterize the microstructure of these pathways, therefore gaining potential insights into brain connectivity, is the main focus of diffusion MR research (Jones 2008a; Jones 2010).

The principle underpinning diffusion tensor MRI is that axons within the white matter (and its subcomponents) create coherent obstacles to diffusion and therefore an orientational dependency of the apparent diffusion coefficient (Moseley et al. 1990). Most commonly, this orientational dependence is modeled by a second-rank tensor assuming a uni-modal Gaussian displacement profile, and a diffusion tensor is fit to the signals in each voxel (Basser et al. 1994b; Basser and Pierpaoli 1996). In turn, scalar indices are derived from the tensor (such as the mean diffusivity and fractional anisotropy (FA) a normalized index of the standard deviation of the eigenvalues that has a range of 0 - 1 (Basser and Pierpaoli 1996).

Given the fact that diffusion tensor imaging is sensitive to various white matter structures it has been developed as a tool to investigate white matter pathways. Diffusion properties such as FA and the radial diffusivity (given by the average between

the two smallest eigenvalues of the tensor, $\frac{1}{2}(\lambda_2 + \lambda_3)$) have been used in a number of clinical, neuroscience and neurodevelopmental studies (Johansen-Berg et al. 2007). Furthermore, derived white matter pathways from diffusion imaging potentially provide information on the connections between cortical regions or physical brain connectivity (Mangin et al. 2002; Shimony et al. 2004; Mori and Zhang 2006; Assaf and Pasternak 2008; Jones 2008a; Bernal and Ardila 2009; Johansen-Berg and Rushworth 2009; Jones 2010; Li et al. 2011; Zalesky et al. 2012).

A number of group analysis methods have been used, such as region of interest (ROI)-based approaches, to explore *prior* hypotheses, and have taken two paths (Cercignani 2010). In one approach, the ROI is drawn manually on a parametric map and the mean diffusion metric derived from within it. Alternatively, the diffusion metric of interest is sampled along a white matter pathway reconstructed using tractography (Kanaan et al. 2006; Jones et al. 2005). However, in many neuroscience studies the researcher does not have a clear prior hypothesis involving specific areas, or may wish to rule out of the possibility of there being differences in unhypothesized regions. In such circumstances, a global and exhaustive search of the brain is necessary. This search most frequently takes the form of searching on a voxel-by-voxel basis, in a family of approaches that we refer to here as voxel-based analysis (VBA). VBA was originally developed to detect differences in volume / density within white and grey matter using a T_1-weighted scan, when it is called voxel based morphometry (Ashburner and Friston 2000). In principle, VBA approaches are less susceptible to operator bias than ROI-based approaches since every voxel in the data set is effectively treated the same.

Prior to a global search, the images need to be registered to a common reference space to the extent that, post-registration, one assumes that a voxel at a specific grid location corresponds to the same anatomical structure in all participants. A challenge for VBA is that imperfect co-registration of participants means that small

misalignments might cause apparent changes in tissue volume / thickness at a given location that are not genuinely related to volume / density differences (Ashburner and Friston 2001; Bookstein 2001; Davatzikos 2004). Nevertheless, carefully designing and validating the VBA procedure has been shown to provide reasonable results (Watkins et al. 2002). In contrast to the T_1-weighted scans that are used for VBA, which lack contrast within a particular tissue type (white matter, grey matter) - largely on account of small differences in the inherent relaxation time constants, parametric maps derived from diffusion tensor MRI, such as FA, are extremely heterogeneous with many boundaries in the image (Basser and Pierpaoli 1996). Small misalignments will therefore have a larger effect on VBA results with FA data than with T_1-weighted data. The standard VBA pipeline incorporates the use of smoothing kernels, introduced (in part) to ameliorate the impact of imperfect registration. However, due to the Matched Filter Theorem (Rosenfeld and Kak 1982), the width of the smoothing kernel can dramatically change the VBA results, not just the spatial extent of group differences but also their spatial location (Jones et al. 2005). Furthermore, if the inter-subject variance in the parameter of interest is non-uniform across the image, the effect of smoothing is to shift the true location of any between-group difference towards the region of lower variance - and this shift increases with the size of the smoothing kernel (Jones and Cercignani 2010). To overcome these concerns over smoothing 'skeleton-projection' was introduced for voxel based analysis of diffusion MRI parametric maps (Smith et al. 2006; Smith et al. 2007), which requires no smoothing step.

Tract based spatial statistics (TBSS) (Smith et al. 2006) combines the 'skeleton-projection' method with non-parametric statistical inference based on threshold-free cluster enhancement (TFCE, (Smith and Nichols 2009)) and has rapidly become the most widely used voxel-based technique for analyzing diffusion MRI data. More than a hundred papers have been published using TBSS (search term='TBSS' in PubMed), which has been designed for easy use for the end-user with an automated pipeline,

and no need to choose a smoothing kernel (Smith et al. 2006). Briefly, the pipeline starts by registering the images to a common reference space using a high-dimensional non-linear warp. Any residual misalignment is catered for by the skeleton-projection approach. First, the average map (averaged across the population) is eroded so only peak FA values one or two voxels thick produce a skeleton. To populate the skeleton, the algorithm searches perpendicularly for the voxel with the highest anisotropy - which is assumed to represent the centre of the tract - and this value is projected on to the skeleton. This step obviates the need for a smoothing kernel to correct for any residual misalignments. Once the skeleton is populated, statistical inferences are made at the cluster level using non-parametric testing (Smith et al. 2006).

There has been a growing number of voxel-based analysis studies of the relationship between white matter microstructure and task performance in behavioural tasks (Johansen-Berg et al. 2004; Madden et al. 2004; Bengtsson et al. 2005; Deutsch et al. 2005; Schulte et al. 2005; Tuch et al. 2005; Wolbers et al. 2006; Johansen-Berg et al. 2007; Flöel et al. 2009) or age-related changes in task performance (Kennedy and Raz 2009; Johansen-Berg 2010). In this work we investigate the stability (reproducibility) of inferences drawn from skeleton-projection based analyses of task-performance versus tissue microstructure correlations and also of the assessment of inter-hemispheric asymmetry of DTI metrics. Specifically, we examine the sensitivity of the result to the exact membership of the group of healthy participants drawn randomly from the same population.

To study the stability of inferences drawn from microstructure-task performance correlations, three behavioural tasks that have previously been shown to correlate with white matter were used:

1. *Choice Reaction Time (CRT)*: Reaction time varies among individuals due to differences in information processing speed. Tuch et al. (2005) previously

showed that CRT within twelve participants (4 Male; mean 23.2y) positively correlates with FA in projection and association pathways, concluding that individual differences in CRT can be explained by individual differences in white matter microstructure within the visuospatial attention network.

2. *Mental Rotation (MR)*: This task looks at the ability to image spatial transformations and differences within the visual-spatial pathway. It is therefore reasonable to hypothesize that tissue microstructure in the visual spatial pathway would correlate with task performance. Wolbers et al. (2006) used this task with sixteen healthy male volunteers (19-29 years) and found a positive correlation between FA and task performance in the white matter underlying the anterior part of the intraparietal sulcus that is known to be important for visuospatial processing.

3. *Intelligence quotient (IQ)*: The intelligence quotient is commonly used in many developmental (Schmithorst et al. 2005; Clayden et al. 2012), clinical (Yu et al. 2008) and more recently genetic (Chiang et al. 2009; Chiang et al. 2011) performance-microstructure correlation studies. Positive correlation has previously been found between FA and task performance within the frontal and occipito-parietal areas ((Schmithorst et al. 2005) N=47) and the right uncinate fasciculus (Yu et al. 2008).

Having studied the reproducibility of TBSS results when correlating microstructural indices with task-performance on the three tasks highlighted above, we then study the reproducibility of results when using TBSS to assess inter-hemispheric asymmetry of microstructural indices.

6.2 Material and Methods

6.2.1 Participants

Across twenty-six TBSS-based studies of microstructure-task performance correlations published in the literature, the median participant-sample size is 21 (range 12-93), which dictated the sample size used in the present study. A total of twenty-four healthy right-handed female participants (age= 31.1± 6.7) were included in this study. Informed consent was obtained prior to scanning and the study was performed with ethics approval from the ethics review board at our institution.

6.2.2 MR Imaging acquisition

MRI data were acquired on a 3 T General Electric HDx MRI system (GE Medical Systems, Milwaukee, WI) with an eight channel receive coil (Medical Devices) using a peripherally gated twice-refocused spin-echo EPI diffusion-weighted acquisition. The diffusion-weighted protocol consisted of: sixty axial slices, with effective TR = 20/15 R-R intervals; effective TE = 87ms; acquisition matrix = 96x96; slice thickness = 2.4 mm; FOV of 230 mm; b-value = 1200 s/mm^2 along 60 isotropically distributed gradient directions (Jones et al. 1999); six non-diffusion weighted images; ASSET factor = 2 (Jones and Leemans 2011); total acquisition time = 30 minutes.

6.2.3 Diffusion Data Pre-Processing

Diffusion-weighed images were corrected for participant motion and global geometric distortions using an affine (12 degrees of freedom) coregistration technique using mutual information as the cost-function to normalize the diffusion-weighted images to the first non-diffusion weighted volume. This was followed by appropri-

ate re-orientation of the diffusion encoding vectors (Jones and Leemans 2011) and modulation of the signal intensity by the determinant of the Jacobian of the transformation (Jones and Cercignani 2010) in *ExploreDTI* (Leemans et al. 2009). The diffusion-weighted data were modeled with a single tensor (Basser et al. 1994b) using a non-linear least squares estimation to obtain quantitative scalar indices including fractional anisotropy (FA), mean diffusivity (MD), axial diffusivity (λ_1) and radial diffusivity (RD).

6.2.4 Behavioural Data Acquisition

Each of the three behavioral tests: choice reaction time (CRT), mental rotation (MR) and IQ were performed on each participant prior to their MR session in a quiet room with a trained psychologist and are described in more detail below:

CRT Paradigm

The CRT paradigm used within this experiment was based on Tuch's CRT experiment (Tuch et al. 2005). Briefly, four white horizontally arranged squares were presented on a black background and the participant responded to one of the squares, which changed colour, by pressing the corresponding button with the dominant hand on a response pad, as quickly and accurately as possible for a total of six blocks of 72 trials (total 432 trials). The average reaction time for each participant was recorded.

Mental Rotation Paradigm

Mental rotation ability was evaluated via the paradigm used by Peters et al. (1995), which sets a time limit for responses. Briefly, participants must correctly identify which two of four stimuli are rotations of the target for a subset of twelve targets during a three-minute period. Following a four-minute break, the test is repeated

for another set of twelve targets. A score of "1" for each target is given when both choices are correct, yielding a maximum possible score of 24.

IQ Paradigm

IQ measurements were based on the Cattell Culture-Fair III Test of Nonverbal Intelligence (Scale 2, form A) (Cattell 1973), which was based on fluid and crystallized intelligence factors (Cattell 1963). The test consists of four timed problem sets (series completions, odd-one outs, matrices, topological relations). Each of the four subcomponents were run consecutively with no breaks with progressing difficulty each running three, four, three and two-and-half minutes, respectively.

6.2.5 Behavioural Data Pre-processing and Statistical Analysis

Behavioural measurements were inspected for outliers initially using a boxplot. The relationship between behavioural scores and DTI metrics was assessed on the skeletonised data by linear regression analysis using TBSS.

6.2.6 Assessment of the stability of TBSS Results

Stability was assessed using a bootstrap / jackknife technique where a 'leave 4 out' procedure was used for the 24 participants. For each of 100 iterations, a unique set of 4 participants was randomly eliminated from the total of 24, and the TBSS analysis run on the remaining 20 participants.

For performance correlation analysis three separate procedures were carried out, each containing 100 iterations. In first, labeled A, the 'traditional' or most common study-specific skeletonisation-projection procedure was performed for all diffusion metrics on the subsample of 20 participants for all 100 iterations. The second, labeled B, was carried out to eliminate any variance caused by the skeletonisation

itself, whereby the skeletonisation procedure was performed only once by deriving the mean FA from all 24 participants to acquire a single, and common study-specific skeleton to use on separate iterations. The third, labeled C, was carried out on a predefined 'FMRIB58_FA' mean FA and skeleton for all iterations. For all 3 pipelines, the following standard steps in the TBSS pipeline were carried out: (1) the mean FA map was thresholded to FA > 0.2 to exclude the peripheral pathways which have higher inter-participant variability (2) for each participant their "centre" of a tract was projected onto the skeleton (3) Voxel-wise statistics for behaviour-microstructure correlations were obtained through permutation-based non-parametric inference using randomize (Nichols and Holmes 2002) (1000 permutations) with threshold free cluster enhancement (TFCE) (Smith and Nichols 2009) for each index. Correlations were considered significant if the p-value < 0.05 after correction for multiple comparisons.

Voxel-wise statistics for inter-hemispheric asymmetry were computed using a one-sample t-test on the symmetric-skeletonised mean. The following steps were carried out: (1) the average mean FA is reflected about the midline to produce a symmetrised mean-FA (2) this map is then skeletonised (3) the skeleton is masked from a dilated version of the skeleton produced in the original full-brain skeletonisation (4) steps (1)-(3) are repeated, flipping and masking the non-flipped version, followed by thresholding to creating the final thresholded symmetrised skeleton.

The final results yielded 100 TBSS results for both behaviour-microstructure correlations and interhemispheric asymmetry analysis.

6.2.7 Cross Correlation

To assist in visualization of the similarity / heterogeneity of results, the skeletonised and threshold t-statistic maps for a given slice location were binarized and collapsed into a single vector comprising zeros (not significant) or ones (significant be-

havioural correlation / asymmetry). For each DTI metric, and for each TBSS analysis performed, for a given slice location, a cross-correlation (CC) matrix for vectors containing at least one significant voxel was computed. (Note, the resulting CC-matrices had different sizes for different metrics /different tasks, dependent on the number of significant voxels within each of the 100 vectors). Each resulting CC-matrix was then re-ordered using the Fiedler vector of the normalized Laplacian formed from this CC-matrix (Barnard et al. 1993) (See Figure 6.1 for an example). This step was performed to assist in finding similarities (adjacent entries in the re-ordered CC-matrix) and dissimilarities (entries that are far apart in the re-ordered CC-matrix) within the TBSS results.

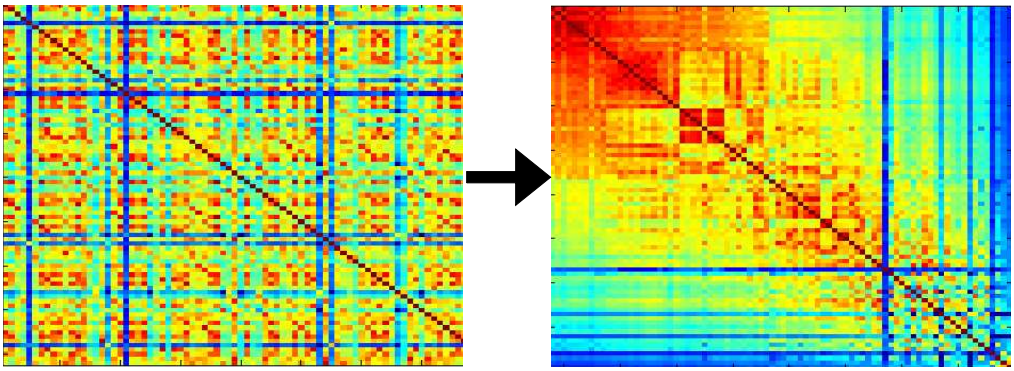

Figure 6.1: An example of a CC-matrix before (left) and after (right) being re-ordered using the Fiedler vector of the normalized Laplacian. This step was performed to assist in finding similarities (adjacent entries in the re-ordered CC-matrix) and dissimilarities (entries that are far apart in the re-ordered CC-matrix) within the TBSS results.

6.2.8 Plotting Frequency and Confidence Intervals

To visualize the reproducibility of the TBSS result, we map the frequency with which a given voxel reaches significance ($p < 0.05$ after correction for multiple comparisons) over the 100 iterations. However, while this provides a picture of how likely

the two variables under investigation are actually correlated in the general population, it does not tell us how strong that correlation is. Confidence intervals indicate the range of possible effect sizes compatible with the acquired data. Furthermore, the greater the variance within the dataset the larger the confidence interval and hence less precise estimates of the parameter. Confidence intervals of 95% were estimated and mapped from the 2.5^{th} and 97.5^{th} quantiles derived from the t-statistic calculated for the 100 bootstraps. To provide a rough indication of the effect size of the correlation under investigation the width of the confidence interval and the lower bound of the confidence interval is mapped. To aid in visualization, voxels in which the confidence interval overlapped zero were set to zero

6.3 Results

6.3.1 Behavioural Measures

Figure 6.2 shows the boxplots for all three behavioural measures: CRT, IQ and MR. These results suggest that there is large inter-individual variability in the behavioral measures, where IQ appears to have the largest variability and CRT is skewed towards smaller reaction times. From the box-plot, it appears that three participants are outliers within the CRT experiment.

6.3.2 Performance-Microstructure Stability Measures

The bootstrapping procedure reveals a large variability of results when correlating task-performance with diffusion metrics and this is despite the fact that the group of 20 participants in each iteration was drawn from the same pool of 24 participants (Figures 6.5, 6.7 and 6.9). Regardless of the skeleton-projection procedure taken for

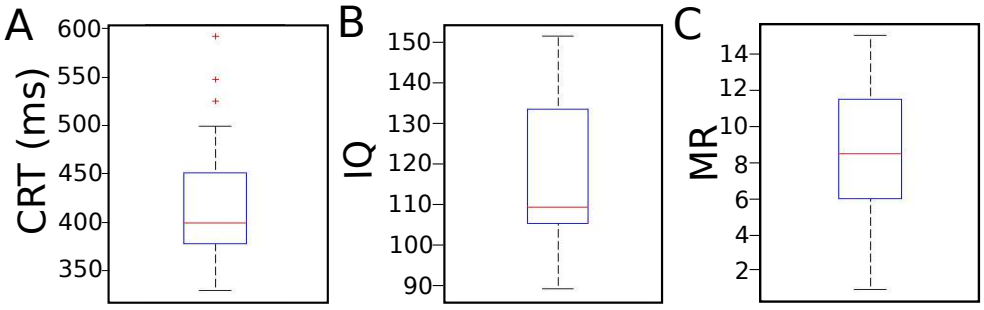

Figure 6.2: Boxplots showing the behavioural values for A) CRT B) IQ C) MR. The red line indicates the median value, the box the interquartile range (3 percentile values: 25,50,75) and the whiskers the extreme values. Red crosses indicate extreme values.

correlation analysis, the large variability between iterations is still present (Figures 6.5, 6.7 and 6.9). Thus, potential variance from differences in the skeleton used has minimal impact on the variability between iterations. Figure 6.3 shows the differences between skeletons among iterations for all three pipelines. Each of the three behavioural-microstructure correlations is described in more detail below.

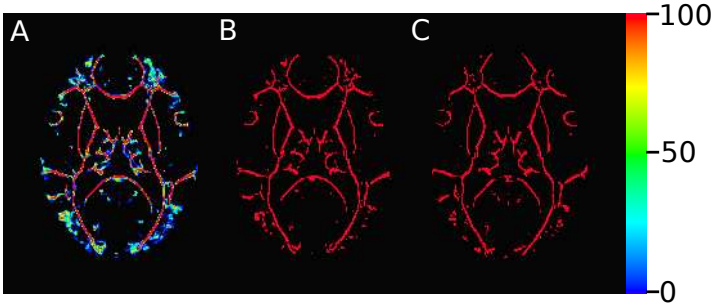

Figure 6.3: Percent overlap or similiarity between mean-skeletons across the 100 iterations. A) Pipeline A: traditional subject-specific skeletonisation-projection procedure applied to all iterations B) Pipeline B: using the same registration and skeletonisation for all iterations within a subject-specific skeletonisation-projection procedure C) Pipeline C: using a predefined-skeleton for skeletonisation-projection procedure.

6.3.3 Choice Reaction Time-Architecture Stability Measures

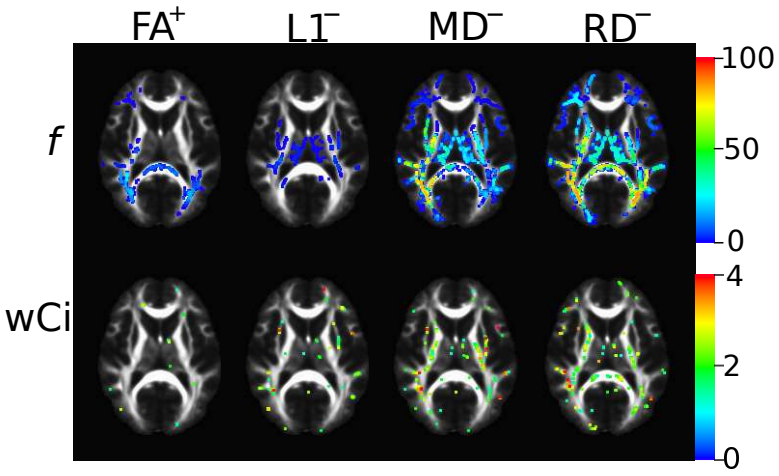

Figure 6.4: For a given slice, the frequency (f) of significant FA-CRT,λ_1/L1-CRT, MD-CRT and RD-CRT correlations in a voxel, where +/- represent if the correlation was positively or negatively correlated. To visualise the effect size the width of the confidence intervals (wCi) for FA-CRT, L1-CRT, RD-CRT and RD-CRT correlations for a given slice location are shown.

Figure 6.4 shows, in each voxel, the frequency with which a significant correlation between CRT and microstructure was found for a given slice, and shows that the results are highly variable. In the majority of the white matter skeleton voxels, there was a significant correlation for MD-CRT or RD-CRT on at least one of the 100 iterations. However, in these voxels, the exact number of times that a significant correlation was found to vary between 1 and 85% of the time. Similarly, in voxels where at least one iteration yielded a significant FA-CRT and/or λ_1-CRT correlation, the frequency of a significant correlation varied between 1 and 30%. Importantly, in the majority of voxels where a significant correlation between FA and CRT or λ_1 and CRT was found at least once, the total number of times a significant result was found in that voxel was less than 50% (i.e., less than chance). In contrast, in voxels yielding at least one significant correlation between MD and CRT and between RD and CRT, the majority (especially within the main white matter pathways) were significant on more than 50% of the iterations. FA was positively correlated with CRT, while λ_1, MD and RD were all negatively correlated with CRT. It is worthy of note that for

FA, MD and RD, the structures in which correlations are found most frequently are the optic radiations, which is in keeping with the result of (Tuch et al. 2005). Those areas that do not overlap with Tuch *et al.*'s findings (e.g. in the frontal white matter) are observed with far lower frequency.

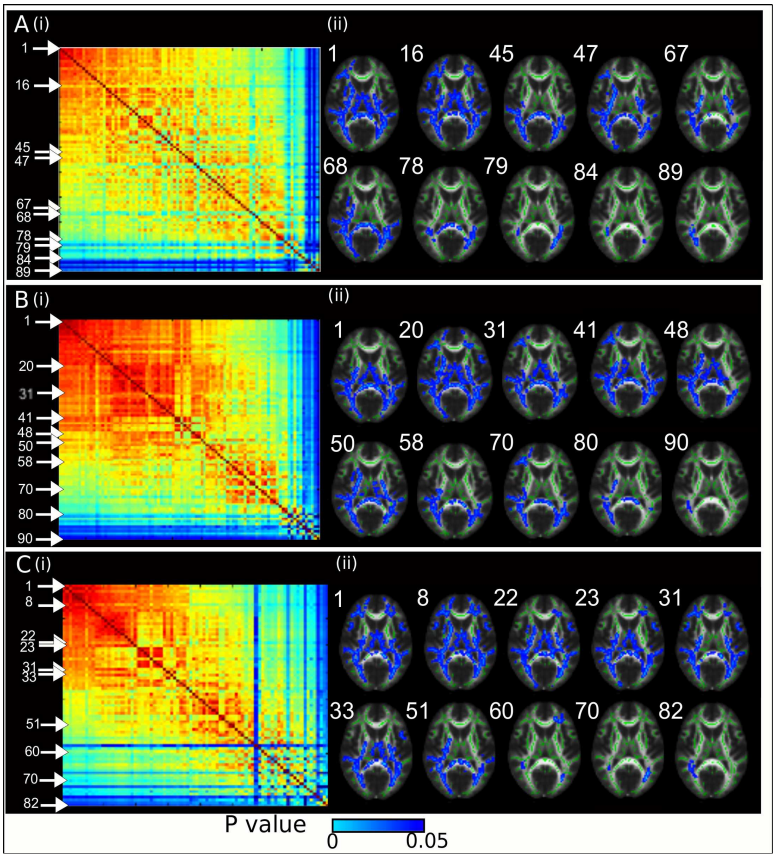

Figure 6.5: For a given slice the CRT-RD cross-correlations for each pipeline (A) subject-specific skeletonisation-projection procedure applied to all iterations (first row) (B) using the same registration and skeletonisation for all iterations within a subject-specific skeletonisation projection procedure (second row) (C) using a predefined-skeleton for the skeletonisation-projection procedure (third row). The cross-correlation matrices for CRT-RD correlations of the vectorized voxels from each iteration, where non-significant iterations were set to zero, were re-ordered for the slice location shown (left). From the re-oredered CC-matrix iterations were selected where borders appear to demonstrate disparate results (right).

Figure 6.5 shows an example of the wide array of results obtained when correlating CRT with RD. The cross-correlation of the results from the 100 iterations reveals a

large heterogeneity in the results, and selecting iterations from the first and last few rows from the sorted CC-matrix shows just how different the results can be. Again, using CRT-RD correlations as an example, the effect size for this correlation is visualized in Figure 6.4 (where the width of the confidence interval and the lower bound are mapped), for a given slice location. Clearly, looking at the CRT-RD correlations one can see as the frequency of getting a significant result increases (Figure 6.4, from p-values) the more confident we are that a relationship exists (Figure 6.4, from confidence intervals).

6.3.4 Mental Rotation-Architecture Stability Measures

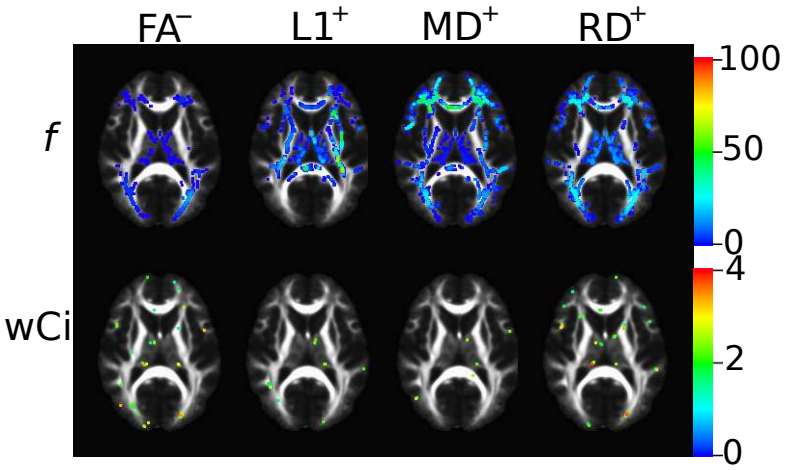

Figure 6.6: For a given slice, the frequency (f) of significant FA-MR, 1/L1-MR, MD-MR and RD-MR correlations in a voxel, where +/- represent if the correlation was positively or negatively correlated.To visualise the effect size the width of the confidence intervals (wCi) for FA-MR, L1-MR, RD-MR and RD-MR correlations for a given slice location are shown.

Figures 6.6 and 6.7 demonstrate the wide array of results obtained from MR-microstructure correlations. For the majority of the white matter skeleton voxels at least one iteration yield a significant correlation for MD-MR or RD-MR among the 100 iterations. Nevertheless, the exact number of times that a significant correlation

was found varied between 1-70% (Figure 6.6) and was very heterogeneous across the skeleton. Likewise, where at least one iteration yielded a significant FA-MR and λ_1-MR correlation was found to vary between 1 and 30%. Furthermore, the confidence interval (Figure 6.6) indicates there is a large variance within the parameters across the skeleton, thus a large range of effect sizes and a low confidence that a relationship actually exits. FA was negatively correlated with MR, while λ_1, MD and RD were positively correlated with MR. Figure 6.7 shows an example of the wide array of results obtained when correlating MR with FA and RD. The cross-correlation of the results from the 100 iterations reveals a large heterogeneity in the results.

6.3.5 IQ-Architecture Stability Measures

Figure 6.8 and 6.9 shows the stability of IQ-RD correlations. For voxels in the white matter skeleton in which at least one iteration yield a significant correlation, the frequency with a significant FA-IQ, λ_1-IQ, MD-IQ and RD-IQ ranged from 1-30% (Figure 6.8). FA was negatively correlated with IQ, while λ_1, MD and RD were positively correlated with IQ. Furthermore, no major differences between pipelines A, B and C can be seen and the variability among white matter structures was fairly consistent between the three pipelines (Figure 6.9). Using IQ-RD correlation as an example, effect size can be visualized in Figure 6.8, for a given slice.

6.3.6 Stability of Microstructural-Asymmetry Measures

The results from inter-hemispheric asymmetry analysis were found to be far more stable (in terms of sensitivity to group membership), than assessment of structure-performance correlations. Figure 6.10A shows results for FA, and even when selecting iterations from the top, mid or bottom of the sorted cross-correlation matrix, the results are largely consistent, with little variation along the skeleton. Similar results

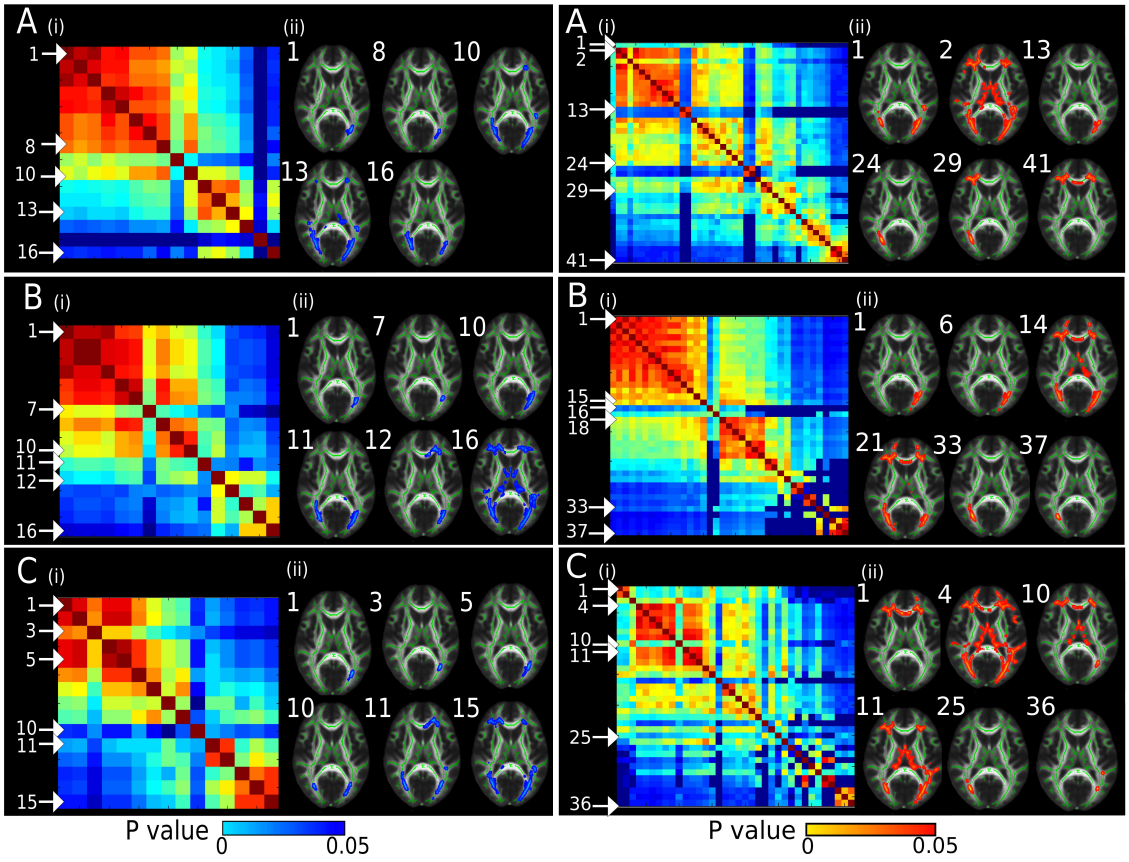

Figure 6.7: For a given slice the MR-FA (left) and MR-RD (right) cross-correlations for each pipeline (A) subject-specific skeletonisation-projection procedure applied to all iterations (first row) (B) using the same registration and skeletonisation for all iterations within a subject-specific skeletonisation projection procedure (second row) (C) using a predifined-skeleton for skeletonisation-projection procedure (third row). The cross-correlation matrices of the vectorized voxels from each iteration, where non-significant iterations were set to zero, were re-ordered for the slice location shown (left). From the re-ordered CC-matrix iterations were selected where borders appear to demonstrate disparate results (right).

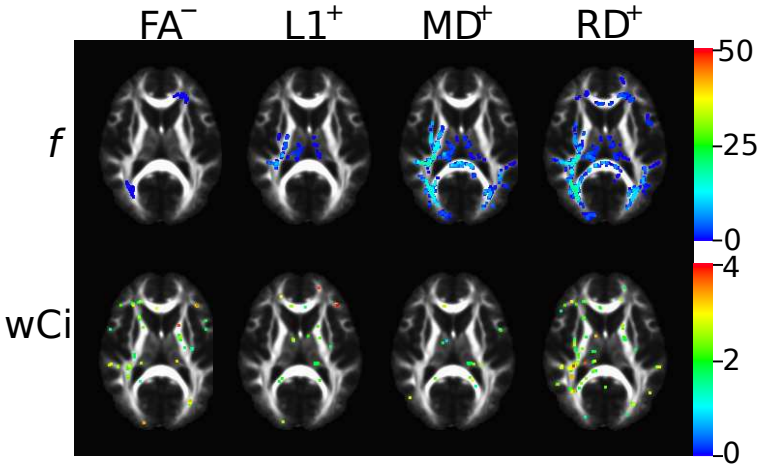

Figure 6.8: For a given slice, the frequency (f) of significant FA-IQ, λ_1/L1-IQ, MD-IQ and RD-IQ correlations in a voxel, where +/- represent if the correlation was positively or negatively correlated.To visualise the effect size the width of the confidence intervals (wCi) for FA-IQ, L1-IQ, RD-IQ and RD-IQ correlations for a given slice location are shown.

can be seen for the comparison of asymmetry in λ_1, MD and RD, where the same voxels showing significant asymmetry are found in most of the 100 iterations (Figure 6.10 B, C and D). For voxels showing a significant asymmetry effect in at least one iteration, the frequency with which an asymmetry effect was found ranges between 1 and 100% (Figure 6.11). The findings tend to be more consistent along major white matter pathways, but become less homogenous towards the brain periphery. Importantly, looking at the inter-hemispheric asymmetric results one can see its increased stability and as the frequency of getting a significant result increases (Figure 6.11, p-values) the confidence of the relationship existing also increases (Figure 6.12, from confidence intervals).

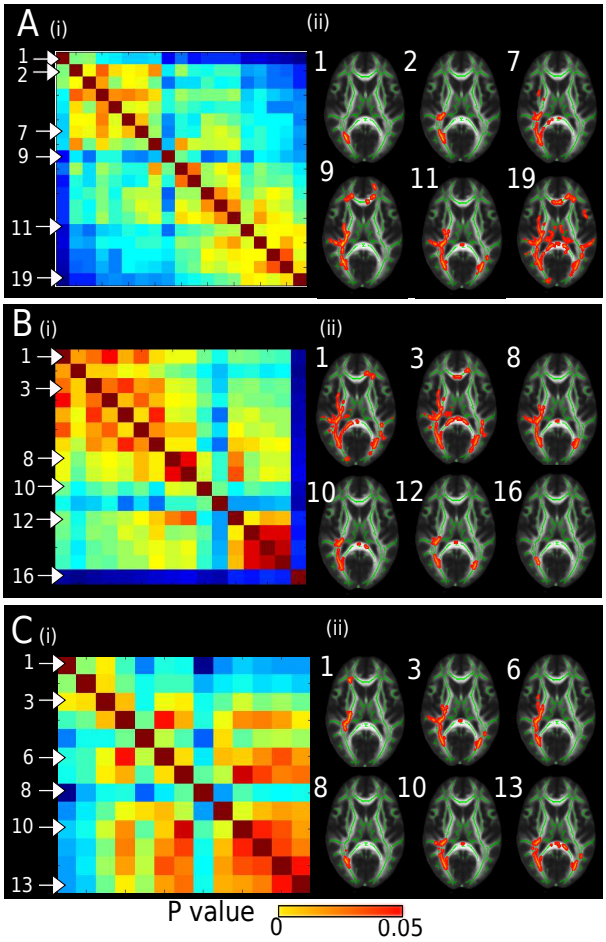

Figure 6.9: For a given slice the IQ-RD cross-correlations for each pipeline (A) subject-specific skeletonisation-projection procedure applied to all iterations (first row) (B) using the same registration and skeletonisation for all iterations within a subject-specific skeletonisation projection procedure (second row) (C) using a predifined-skeleton for skeletonisation-projection procedure (third row). The cross-correlation matrices for IQ-RD correlations of the vectorized voxels from each iteration, where non-significant iterations were set to zero, were re-ordered for the slice location shown (left). From the re-oredered CC-matrix iterations were selected where borders appear to demonstrate disparate results (right).

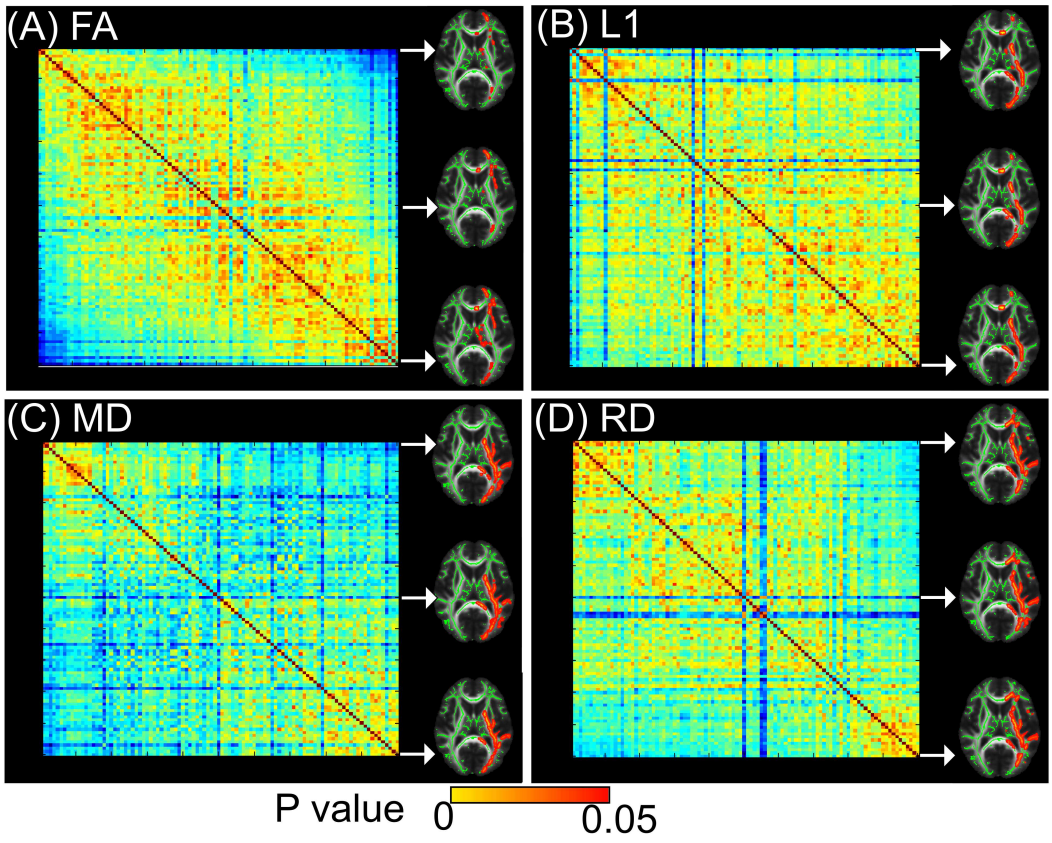

Figure 6.10: For a given slice location the cross-correlations across the 100 interations for symmetric measurements (A) FA (B) L1 (C) MD (D) RD. The re-ordered cross-correlation matrices for SYM correlations of the vectorized voxels from each iteration, where non-significant iterations were set to zero, were re-ordered for the slice location are shown (left). From the re-oredered CC-matrix three iterations were selected where borders appear to homologous results (right).

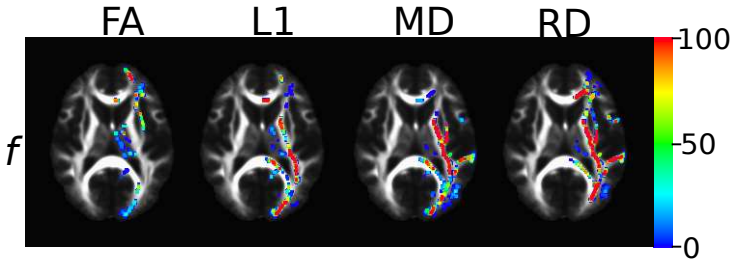

Figure 6.11: For a given slice, the frequency (f) of significant FA-SYM, λ_1/L1-SYM, MD-SYM and RD-SYM correlations in a voxel.

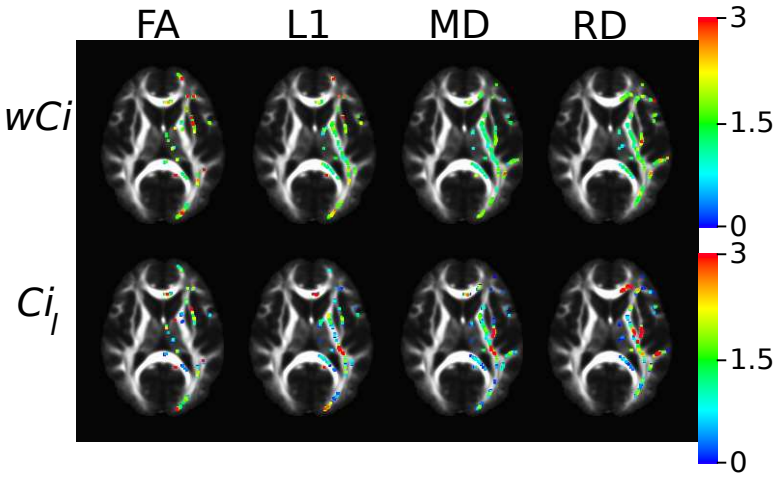

Figure 6.12: To visualise the effect size for the interhemispheric asymmetries the width of the confidence intervals (wCi) and the lower bound of the confidence interval (CiL) for SYM-FA, SYM-L1, SYM-RD and SYM-RD correlations for a given slice location, where confidence intervals that cross zero were set to zero.

6.4 Discussion

This study makes two main observations:

1. Despite the use of randomization testing procedures, TBSS results can be rather unstable when performing structure-performance correlation studies, showing a high sensitivity to the exact sample of participants used in the test.

2. Assessment of asymmetry using TBSS seems to be much less susceptible to this effect.

The boxplot of CRT emphasizes the variance within this measure. A number of factors can contribute to this variance (e.g. inattentiveness) while others are assumed to be negligible (i.e. fatigue or sequential effects (Thornton and Gilden 2005)). However, any extreme values should be further investigated before being labeled as outliers, as they often contain valuable information about the biological process under investigation or the data-gathering process. If such values are due to a biological process they can change the meaning of results if eliminated, especially if differences

in scores from individual may be explained by their white matter microstructure. Correlation results from Tuch et al. (2005) demonstrated that individual differences in CRT are related to individual differences in tissue microstructure (FA measures). Here, our 'extreme' values within the CRT paradigm are actually within the same range as the previously published data (Tuch et al. 2005). Thus, eliminating these values may not be justified and may have profound effects on interpretation. The main difference between the study of Tuch et al. (2005) and the present study is that majority of our participants had lower CRT measures (median CRT in our study= 399.8±65.7 ms, median CRT in Tuchs study 447±62.7 ms). A positive skew in reaction time distribution is a well-known phenomenon since there is a lower biophysical limit to how fast participants can respond, but not an upper one (Luce 1986). Importantly, skewed reaction time data cannot be tested using parametric tests without transforming the data, thus in such cases the non-parametric TBSS procedure is ideal.

The choice reaction time task is known to evoke visual attention network and has been shown the correlate with diffusion indices (Tuch et al. 2005). Here, using TBSS the frequency with which a significant CRT-RD correlation was found to vary significantly across anatomical locations depending on the iteration you are looking at (Figure 6.5). For example, correlations between CRT-RD one can see that from the reordered graph some iterations demonstrate a wide range of significant voxels and others only show the left or right occipital lobe. Importantly, if the results can vary to this degree by only changing a few participants it can have profound implications on the generalization of such correlations to the wider population. For this reason maps, such as frequency or confidence intervals, are useful in interpreting how large the effect is and how much confidence can be placed in a correlation actually existing.

The mental rotation task is also known to involve a number of different cortical structures, such as those within the posterior parietal subdivision. Through both human and monkey experiments (Andersen et al. 1997; Grefkes and Fink 2005)

these areas are known to process external objects and imagined motion in two or three-dimensional space. Variations between participants' ability to perceive spatial transformation of an object is due to differences within the ability to transfer information between necessary brain structures and it is reasonable to hypothesize that task performance might depend on the white matter pathways that connect these areas. Wolbers et al. (2006) found that FA within the intraparietal sulcus correlated positively with the ability to mentally rotate objects. Furthermore, in a recent review it was noted that white matter pathways that connect the parietal and frontal lobes are important in spatial attention (Doricchi et al. 2008). It is important to note from Figure 6.7 that the anatomical location where a significant correlation appears varies quite a bit across different iterations. For example, correlations between MR-RD one can see that from the reordered graph that the first volume has significance only in the frontal cortex and the last volume from the reordered matrix shows significance only in the occipital lobe.

The frequency with which a significant IQ-RD correlation was found was quite low (Figure 6.8), with only 19% of the bootstrapped iterations producing a significant correlation in any voxel, and the voxels showing significant correlations being heterogeneously distributed across the iterations. For example, some iterations only have significant voxels within the frontal cortex while others only have significant voxels in the occipital lobe. There has been a number of studies correlating intelligence quotient and total brain volumes, finding a positive correlation (e.g. Andreasen et al. (1993), who studied 67 participants, and Witelson et al. (2006) who studied 100 participants postmortem). In addition, VBM studies find correlations between IQ and structural measures in various brain regions: within grey matter correlations in frontal, parietal, temporal and occipital cortex (Haier et al. 2004; Colom et al. 2006) and white matter correlations in parietal fibre tracts (Haier et al. 2004). Thus, there is converging evidence that IQ is dependent on a number of higher cognitive brain

areas involved in language, memory and attention, which highlights how essential the connections between different brain structures are. Looking into the connections or the white matter pathways between these areas may help us understand individual differences in IQ within the healthy adult population. Another study using voxel-wise correlations of FA with IQ (using statistical parametric mapping (Friston 1995)) found a positive correlation between FA and IQ in frontal and occipito-parietal white-matter areas within a healthy pediatric population ((Schmithorst et al. 2005) N=47). However, within our own TBSS analysis we found negative correlations between FA and IQ, while the other DTI indices were positively correlated.

Our study revealed other unexpected correlations, such as the positive correlation seen between CRT and FA (i.e., the higher the anisotropy, the longer the reaction time) which replicates the earlier finding of Tuch et al. (2005). This is, perhaps, counter-intuitive and one might predict that higher FA means better task performance. However, this is only the case if there is a single fibre population in the voxel. In cases where there are multiple fibre populations, one may find increased FA in disease (e.g. (Douaud et al. 2011)).

These apparently anomalous findings may simply reflect the fact that we do not really understand exactly what FA is sensitive to, or rather, what substructure in the white matter is most responsible for differences in performance on a given task. DTI metrics such as FA, are very non-specific, and can change in response to differences in axon morphology (diameter, packing, orientational dispersion), the degree of myelination, and the intravoxel orientational coherence of the constituent microstructure (Beaulieu and Allen 1994b). If we were to assume that correlation between behavioural measures and task performance was due to differences in myelin thickness, one may expect or predict a negative correlation between reaction times from the CRT experiment and FA, meaning that an increase in myelin thickness increases FA and in turn increases the conduction velocity along the relevant pathways resulting

in faster reaction times. Contradictorily, the CRT-FA correlations within this experiment were, however, found to be positive, which was also reported by Tuch et al. (2005). This result might be explained by differences in intravoxel orientational dispersion, or in axon diameter distribution, axon packing, or some other factor, the point being that FA cannot distinguish between them. Here, measures of microstructure that are more selectively specific to white matter sub-components such as myelin or axon diameter, for example, may provide a better measure to correlate microstructure to performance.

The complete network of white matter pathways involved in the specific behavioural tasks used in this study is unknown, as is the case for almost any function of the brain. Thus the desire for a robust global- voxel-based search for correlation between performance-microstructure correlations is understandable. The introduction of skeleton-based projection based methods, as in TBSS, is most certainly an improvement on the original voxel-based analysis methods that were developed primarily for the analysis of T_1-weighted structural image data. However, the effective power or the number of participants needed to robustly identify a correlation between tissue microstructure and task performance is unknown. Recently, it was demonstrated that the power to detect group differences in a white matter structure using TBSS is dependent on the location and orientation of that tract (Edden and Jones 2011). It was also found that the inter-subject variance in FA across the skeleton was extremely heterogeneous. Moreover, the orientation of skeletonised white matter in relation to the imaging matrix alters the thickness of the skeleton, thus impacting the number of voxels in the local neighbourhood that can contribute to the evidence of a cluster in cluster-based statistical inference (Edden and Jones 2011). This can have a major affect on detection differences between different white matter pathways and their correlation with behavioural measurements in tract-based statistics analysis.

In this study, we illustrate an additional concern within TBSS analysis: the low stability of performance-microstructure correlations as seen in all three of our behavioural tasks. Specifically we found low reproducibility of results among 100 resamples of 20 participants (total 24 participants, leave out four). We are confident that this variability or low stability is attributed to the analysis of the correlation data since the variability among task performance and micro-structure correlations were very similar between the three pipelines (A,B and C): one where registration was performed for each iteration, the second registration and skeletonisation was performed once for all 24 participants and the third a predefined skeleton was used. In addition: (1) among most voxel-based studies in the literature the median number of participants is 21 (average = 25, std 17); (2) most studies do not report on the confidence intervals or effect size of these performance-microstructure correlations. It is well known through fMRI behavioural group analysis that significant results will vary depending on your sample pool especially within small sample sizes (Murphy and Garavan 2004). Here, instead of removing a specific participant to improve homogeneity we randomly did a leave out 4 approach to assess the reliability of performance-microstructure correlations by producing frequency or confidence interval maps. However, to reduce the vulnerability to inhomogeneites even more it is suggested to do a leave out 1 approach, particularity in small group sizes (<20) (Wilke 2012). That being said the number of participants or initial group membership needed to produce a stable result needs to be further explored (See Murphy and Garavan (2004) for work in fMRI).

The variability in the correlations found over the 100 bootstraps iterations clearly demonstrates the need to report confidence intervals or the frequency of a significant result. Others that have gone beyond just reporting p-values from correlations have done so in fMRI (Friston and Penny 2003). Recently, Wilke (2012) used a resampling technique to produce a group percent overlap map for fMRI group analysis similar to

our frequency maps. Until our study most performance-microstructure correlations have not reported confidence intervals or frequency plots, most likely because re-sampling techniques are heavily computer intensive. That being said, the likelihood of getting a significant result could be overestimated and not reporting confidence intervals, which indicates the size of the effect, can lead to misinterpretations. Importantly, not reporting confidence intervals in under-powered studies, such as small sample sizes, when the magnitude of the effect is less than 20% of the standard deviation of the noise or when number of comparisons are large as in voxel based MRI analysis, will lead to overestimating effect size due to larger confidence intervals (Gelman and Weakllem 2009; Vul et al. 2009; Cohen 1988). Naturally, for under-powered studies most effects are not detected and sometimes one is fortunate to measure a significant effect, which is most likely to be much larger than the true effect. Although it is possible to observe a significant correlation between FA and MR in a few of the bootstrap iterations, examination of the confidence interval maps suggest that the effect size is too small to be able to generalize to the population. On the other hand, both CRT and IQ demonstrate that the measured effect size is large enough, in the slice studied, to conclude that there is a relationship between CRT-RD and IQ-RD that can be generalized to the population. Conversely, interhemispheric asymmetry measures demonstrate small/narrow confidence interval widths and thus a small range of effect sizes across all microstructural measures and our results demonstrate that a higher confidence can be placed in finding a real asymmetry within the generalized population.

With the increased use of push-button operation software, that provides a correction for multiple comparisons, many users will regard the result of a significant correlation as a reliable result that can be extended to the general population. Our findings that such results are not generalizable and are, in fact, very sensitive to the exact group membership, is extremely worrying. Importantly, we showed using a

resampling method that for three different behavioural measures the stability for a literature median number of participants (N=21) was low. Thus, based on these finding, adoption of TBSS for microstructure-performance correlation may be premature until such time as robust analysis of the number of participants needed for reliable results has been conducted. Although we have no gold standard against which to validate the accuracy of asymmetry measures, it appears that TBSS provides far more reproducible (i.e., precise) estimates of interhemispheric asymmetries than of performance-microstructure correlations. Furthermore, if our recommended approach of presenting confidence interval maps alongside the usual results is adopted, the reporting of results in such studies would be more cautious, and perhaps even unimportant / ungeneralizable results would not be reported. Continued efforts in estimating the exact number of participants to produce stable results with performance-microstructure correlations through the establishment of confidence interval maps, together with the adoption of more specific white matter markers (as myelin and axon specific indices), will help us to understand more about the apparently anomalous relationships seen here, such as that positive correlation between FA and CRT and give better understanding in general of the relationship between task performance and white matter microstructure.

Summary of Contributions and Future Work

This thesis has combined novel imaging methods in a unique multi-modal approach called *Tractometry*. Tractometry permits simultaneous quantitative assessment of different microstructural attributes, such as metrics of quantitative mangetisation transfer (qMT), multi-component relaxometry and advanced models of diffusion (CHARMED) along specific pathways. The major contributions of this work are summarized below along with directions for future research.

Short synopsis and Contributions/Implications

The relationship between structure and function is a recurring theme throughout neuroscience. Functional connections within the brain grey matter depend on physical connections formed by the white matter. The white matter is formed from tubular-axons, of varying diameter, wrapped in a fatty insulating layer of myelin. The axons form distinct bundles, or tracts, that connect different brain regions. The axon diameter and myelin thickness are optimised for efficient information transfer, and individual differences in these parameters (due to development, genetic, and/or pathological influences) may explain differences in brain function, behaviour or disease symptomatology.

To date nearly all imaging studies of white matter microstructure have used diffusion tensor MRI (DT-MRI). Fractional anisotropy (FA) mapping from DT-MRI has been routinely used, and changes in FA are often interpreted as a change in integrity and/or connectivity. There are many studies that correlate behavioural/cognitive tests with FA (e.g. Johansen-Berg et al. 2004; Madden et al. 2004; Bengtsson et al. 2005; Deutsch et al. 2005; Schulte et al. 2005; Tuch et al. 2005; Wolbers et al. 2006; Johansen-Berg et al. 2007; Flöel et al. 2009) and show that FA changes over years/months (Bengtsson et al. 2005; Scholz et al. 2009), sometimes being interpreted as showing changes in myelination. However, many of these studies have observed counter-intuitive results such as increased reaction time associated with an increase in FA (Tuch et al. 2005 and Chapter 6). As outlined elsewhere (Beaulieu and Allen 1994b; Beaulieu 2002) DT-MRI is sensitive

to both interesting properties of white matter (axon density, axon diameter, myelination), and less interesting properties (dispersion of axon orientation within the voxel). However, it is impossible to disentangle which property or properties of white matter are changing from the DT-MRI signal. Moreover, DT-MRI has differential sensitivities to these different properties. Furthermore, it has been shown that cerebrospinal fluid (CSF) contamination if not corrected for results in errors within diffusion parameters (Alexander et al. 2001; Metzler-Baddeley et al. 2012; Vos et al. 2011). Interestingly, in Chapter 5 we found a lateralization with the relative tissue volume fraction measured from diffusion-weighted images and in myelin water fraction. This spatial heterogeneity of partial volume effects can potentially confound interpretation of results in studies where contralateral hemispheres are used as internal control regions of interest by either exacerbating real tissue differences or possibly even negating them. It is important to stress that this effect was found in a young healthy control population and it is expected that this will be an exaggerated confound in an older population due to atrophy, and would be even more marked in diseased populations (Metzler-Baddeley et al. 2012). The full extent of the influence of this asymmetry in partial volume effects on ROI-based measurements within such studies should be further investigated.

To understand the role of white matter microstructure in mediating functional connections, it is important to access the electrical properties of a white matter pathway which are, in turn, mediated by myelination and axon diameter / density. An increased understanding of how these sub-components vary within white matter will allow us to understanding differences in functional connections, (such as differences in delay times arising from differences in conduction velocity).

Such knowledge could then be meaningfully integrated into models of functional/effective connectivity. Very little progress has been made in incorporating microstructural white matter metrics into functional connectivity models, the exception being limited to a few studies using DT-MRI based metrics. Thus, tractometry is an important step forward in increas-

ing our understanding of the role that different white matter sub-components has on the functional communication between grey matter regions (introduced in Chapter 4).

The results of this thesis showing only weak correlation between proxy indices of myelination and axonal morphology, suggests that additional complementary WM microstructural information is obtained with tractometry. Before translation to clinical applications, it would be prudent to compare these imaging metrics (from *in vivo* animal experiments) with histology, to really understand what drives differences in the signal contrast and the specificity to changes in a particular sub-component of the tissue microstructure. Moreover, before translation to the clinic, it would be important to assess further how these metrics are affected by changes in free water partial volume contamination within a voxel, such as may occur in inflammation.

In terms of ongoing work, there are a number of studies being carried out in Cardiff University that are exploiting our tractometry pipeline to probe differences within white matter structure across different patient sub-groups in a wide range of neurological and developmental disorders (autism, ADHD, epilepsy and multiple sclerosis), psychiatric disorders (depression, schizophrenia and psychosis), structural asymmetry of white matter metrics (Chapter 5), and explaining individual differences in cognitive performance in terms of microstructural differences.

With increasing popularity of conducting studies and determining differences between structure and function on a voxel-by-voxel basis using such methods like Tract Based Spatial Statistics (TBSS) (Smith et al. 2006) we conducted preliminary work on the reproducibility of such analyses in Chapter 6. Reproducibility of significant results was assessed using a bootstrapping approach (100 bootstraps with N=24-4 approach) and found the pattern of results highly variable and very sensitive to the exact membership to the cohort tested. Although, this variability was much less marked when assessing inter-hemispheric asymmetry in microstructural indices, the unstable results from structure-function correlations is a cause for concern. Thus, based on these findings, current application of this approach may be premature until a more robust analysis method is introduced. Or, alternatively, as

we suggest in Chapter 6, correlations should be reported alongside additional maps such as the frequency with which a given voxel contains a significant result or confidence interval for a given voxel. In addition, continued efforts are needed to estimate the exact number of participants required to produce stable results with performance-microstructure correlations. Based on our findings here, we encourage the adoption of more specific white matter markers (i.e. myelin or axon indices) as in tractometry, in such voxel-based studies, as it should help us understand more about some apparently anomalous relationships seen here, such as a positive correlation between FA and reaction time (Chapter 6).

A clear application for tractometry is to try to explain differences in functional connectivity, as assessed using fMRI, MEG or EEG, in terms of differences in specific properties of white matter microstructure. The integration of microstructural and functional MR imaging has been previously reported using Dynamic Causal Modelling (DCM) and probabilistic fibre tracking data (Stephan et al. 2009). While the finding that a high probabilistic tracking connectivity relates to a high functional connectivity is promising, this study has a few limitations: (1) tractography is not tractometry, by which we mean that tractography (probabilistic and deterministic) typical only uses the orientational information present in the diffusion-weighted signal, and does not utilize information about tissue microstructure; and (2) fMRI is a less direct measure of the brains electrical activity than techniques such as MEG and EEG, being coupled through the vasculature. Moreover, the temporal resolution of fMRI is far inferior due to the haemodynamic delay. We believe that greater insights into the relationship between functional connectivity and tissue microstructure will be had by combining more direct measures of brain function than fMRI, and more direct measures of microstructure than probabilistic tractography and DT-MRI. We will be combining tractometry with MEG and trying to address the question as to which microstructural measurement(s) best explain(s) differences in functional connectivity, as a natural extension of the work conducted in this thesis.

Bibliography

Ahmadi, M. E., Hagler, D. J., McDonald, C. R., Tecoma, E. S., Iragui, V. J., Dale, A. M., & Halgren, E. (2009, Oct). Side matters: diffusion tensor imaging tractography in left and right temporal lobe epilepsy. *AJNR Am J Neuroradiol*, 30, 1740–1747.

Alexander, A. L., Hasan, K. M., Lazar, M., Tsuruda, J. S., & Parker, D. L. (2001, May). Analysis of partial volume effects in diffusion-tensor MRI. *Magn Reson Med*, 45, 770–780.

Alexander, A. L., Tsuruda, J. S., & Parker, D. L. (1997, Dec). Elimination of eddy current artifacts in diffusion-weighted echo-planar images: the use of bipolar gradients. *Magn Reson Med*, 38, 1016–1021.

Alexander, D. C., Barker, G. J., & Arridge, S. R. (2002, Aug). Detection and modeling of non-gaussian apparent diffusion coefficient profiles in human brain data. *Magn Reson Med*, 48, 331–340.

Alexander, D. C., Hubbard, P. L., Hall, M. G., Moore, E. A., Ptito, M., Parker, G. J. M., & Dyrby, T. B. (2010, Oct). Orientationally invariant indices of axon diameter and density from diffusion MRI. *Neuroimage*, 52, 1374–1389.

Alexander, D. C., Pierpaoli, C., Basser, P. J., & Gee, J. C. (2001, Nov). Spatial transformations of diffusion tensor magnetic resonance images. *IEEE Trans Med Imaging*, 20, 1131–1139.

Andersen, R. A., Snyder, L. H., Bradley, D. C., & Xing, J. (1997). Multimodal representation of space in the posterior parietal cortex and its use in planning movements. *Annu Rev Neurosci*, 20, 303–330.

Anderson, A. W. (2005, Nov). Measurement of fiber orientation distributions using high angular resolution diffusion imaging. *Magn Reson Med*, 54, 1194–1206.

Andersson, J., Jenkinson, M., & Smith, S. (2007a). Non-linear optimisation. Technical Report TR07JA1, FMRIB, www.fmrib.ox.ac.uk/analysis/techrep.

Andersson, J., Jenkinson, M., & Smith, S. (2007b). Non-linear registration, aka spatial normalisation. Technical Report TR07JA2, FMRIB, www.fmrib.ox.ac.uk/analysis/techrep.

Andreasen, N. C., Flaum, M., Swayze, V., O'Leary, D. S., Alliger, R., Cohen, G., Ehrhardt, J., & Yuh, W. T. (1993, Jan). Intelligence and brain structure in normal individuals. *Am J Psychiatry*, 150, 130–134.

Andrews, T. J., Osborne, M. T., & Does, M. D. (2006, Aug). Diffusion of myelin water. *Magn Reson Med*, 56, 381–385.

Armspach, J. P., Gounot, D., Rumbach, L., & Chambron, J. (1991). In vivo determination of multiexponential T2 relaxation in the brain of patients with multiple sclerosis. *Magn Reson Imaging*, 9, 107–113.

Ashburner, J. & Friston, K. J. (2000, Jun). Voxel-based morphometry–the methods. *Neuroimage*, 11, 805–821.

Ashburner, J. & Friston, K. J. (2001, Dec). Why voxel-based morphometry should be used. *Neuroimage*, 14, 1238–1243.

Assaf, Y. & Basser, P. J. (2005, Aug). Composite hindered and restricted model of diffusion (CHARMED) mr imaging of the human brain. *Neuroimage*, 27, 48–58.

Assaf, Y., Ben-Bashat, D., Chapman, J., Peled, S., Biton, I. E., Kafri, M., Segev, Y., Hendler, T., Korczyn, A. D., Graif, M., & Cohen, Y. (2002, Jan). High b-value q-space analyzed diffusion-weighted MRI: application to multiple sclerosis. *Magn Reson Med*, 47, 115–126.

Assaf, Y., Blumenfeld-Katzir, T., Yovel, Y., & Basser, P. J. (2008, Jun). AxCaliber: a method for measuring axon diameter distribution from diffusion MRI. *Magn Reson Med*, 59, 1347–1354.

Assaf, Y., Freidlin, R. Z., Rohde, G. K., & Basser, P. J. (2004, Nov). New modeling and experimental framework to characterize hindered and restricted water diffusion in brain white matter. *Magn Reson Med*, 52, 965–978.

Assaf, Y. & Pasternak, O. (2008). Diffusion tensor imaging (DTI)-based white matter mapping in brain research: a review. *J Mol Neurosci*, 34, 51–61.

Barazany, D., Basser, P. J., & Assaf, Y. (2009, May). In vivo measurement of axon diameter distribution in the corpus callosum of rat brain. *Brain*, 132, 1210–1220.

Barker, G. J., Simmons, A., Arridge, S. R., & Tofts, P. S. (1998, Jan). A simple method for investigating the effects of non-uniformity of radiofrequency transmission and radiofrequency reception in MRI. *Br J Radiol*, 71, 59–67.

Barkhof, F., Bruck, W., Groot, C. J. A. D., Bergers, E., Hulshof, S., Geurts, J., Polman, C. H., & van der Valk, P. (2003, Aug). Remyelinated lesions in multiple sclerosis: magnetic resonance image appearance. *Arch Neurol*, 60, 1073–1081.

Barnard, S. T., Pothen, A., & Simon, H. D. (1993). A spectral algorithm for envelope reduction of sparse matrices. *ACM/IEEE CONFERENCE ON SUPERCOMPUTING*, 493–502.

Barnea-Goraly, N., Menon, V., Eckert, M., Tamm, L., Bammer, R., Karchemskiy, A., Dant, C. C., & Reiss, A. L. (2005, Dec). White matter development during childhood and adolescence: a cross-sectional diffusion tensor imaging study. *Cereb Cortex*, 15, 1848–1854.

Basser, P. J. & Jones, D. K. (2002). Diffusion-tensor MRI: theory, experimental design and data analysis - a technical review. *NMR Biomed*, 15, 456–467.

Basser, P. J., Mattiello, J., & LeBihan, D. (1994a, Mar). Estimation of the effective self-diffusion tensor from the NMR spin echo. *J Magn Reson B*, 103, 247–254.

Basser, P. J., Mattiello, J., & LeBihan, D. (1994b, Jan). MR diffusion tensor spectroscopy and imaging. *Biophys J*, 66, 259–267.

Basser, P. J. & Pajevic, S. (2000, Jul). Statistical artifacts in diffusion tensor mri (DT-MRI) caused by background noise. *Magn Reson Med*, 44, 41–50.

Basser, P. J., Pajevic, S., Pierpaoli, C., Duda, J., & Aldroubi, A. (2000, Oct). In vivo fiber tractography using DT-MRI data. *Magn Reson Med*, 44, 625–632.

Basser, P. J. & Pierpaoli, C. (1996, Jun). Microstructural and physiological features of tissues elucidated by quantitative-diffusion-tensor MRI. *J Magn Reson B*, 111, 209–219.

Baudrexel, S., Nürnberger, L., Rüb, U., Seifried, C., Klein, J. C., Deller, T., Steinmetz, H., Deichmann, R., & Hilker, R. (2010, Jun). Quantitative mapping of T1 and T2* discloses nigral and brainstem pathology in early Parkinson's disease. *Neuroimage*, 51, 512–520.

Beaulieu, C. (2002). The basis of anisotropic water diffusion in the nervous system - a technical review. *NMR Biomed*, 15, 435–455.

Beaulieu, C. & Allen, P. S. (1994a, Apr). Determinants of anisotropic water diffusion in nerves. *Magn Reson Med*, 31, 394–400.

Beaulieu, C. & Allen, P. S. (1994b, Nov). Water diffusion in the giant axon of the squid: implications for diffusion-weighted MRI of the nervous system. *Magn Reson Med*, 32, 579–583.

Beaulieu, C. & Allen, P. S. (1996, Jul). An in vitro evaluation of the effects of local magnetic-susceptibility-induced gradients on anisotropic water diffusion in nerve. *Magn Reson Med*, 36, 39–44.

Behrens, T. E. J., Berg, H. J., Jbabdi, S., Rushworth, M. F. S., & Woolrich, M. W. (2007, Jan). Probabilistic diffusion tractography with multiple fibre orientations: What can we gain? *Neuroimage*, 34, 144–155.

Behrens, T. E. J., Woolrich, M. W., Jenkinson, M., Johansen-Berg, H., Nunes, R. G., Clare, S., Matthews, P. M., Brady, J. M., & Smith, S. M. (2003, Nov). Characterization and propagation of uncertainty in diffusion-weighted MR imaging. *Magn Reson Med*, 50, 1077–1088.

Bells, S., Deoni, S., Pasternak, O., & Jones, D. (2011), Partial volume corrections of myelin water fraction values, In *Proc ISMRM 19th Annual Meeting, Montreal*.

Bells, S., Morris, D., & Vidarsson, L. (2007), Comparison of linear combination filtering to DTI and MTR in whole brain myeln-water imaging, In *Proc ISMRM 15th Annual Meeting, Berlin*, pp. 1606.

Bengtsson, S. L., Nagy, Z., Skare, S., Forsman, L., Forssberg, H., & Ullén, F. (2005, Sep). Extensive piano practicing has regionally specific effects on white matter development. *Nat Neurosci*, 8, 1148–1150.

Benjamini, Y. & Hochberg, Y. (1995, January). Controlling the false discovery rate: A practical and powerful approach to multiple testing. *Journal of the Royal Statistical Society. Series B (Methodological)*, 57, 289–300.

Bernal, B. & Ardila, A. (2009, Sep). The role of the arcuate fasciculus in conduction aphasia. *Brain*, 132, 2309–2316.

Bieri, O. & Scheffler, K. (2007, Feb). Effect of diffusion in inhomogeneous magnetic fields on balanced steady-state free precession. *NMR Biomed*, 20, 1–10.

Bookstein, F. L. (2001, Dec). "Voxel-based morphometry" should not be used with imperfectly registered images. *Neuroimage*, 14, 1454–1462.

Bot, J. C. J., Blezer, E. L. A., Kamphorst, W., Nijeholt, G. J. L. A., Ader, H. J., Castelijns, J. A., Ig, K. N., Bergers, E., Ravid, R., Polman, C., & Barkhof,

F. (2004, Nov). The spinal cord in multiple sclerosis: relationship of high-spatial-resolution quantitative mr imaging findings to histopathologic results. *Radiology*, 233, 531–540.

Boujraf, S., Luypaert, R., & Osteaux, M. (2001). b matrix errors in echo planar diffusion tensor imaging. *J Appl Clin Med Phys*, 2, 178–183.

Broca, P. (1861). Remarques sur le siége de la faculté du langage articulé, suivies d'une observation d'aphémie (perte de la parole). *Bull Soc Anatomique Paris 6*, 330–3357.

Brochet, B. & Dousset, V. (1999). Pathological correlates of magnetization transfer imaging abnormalities in animal models and humans with multiple sclerosis. *Neurology*, 53, S12–S17.

Brown, R. (1828). A brief account of microscopical observations made in the months of June, July and August 1827 on the particles contained in the pollen of plants; and on the general existence of active molecules in organic and inorganic bodies. *Philosophical Magazine*, 4, 161.

Büchel, C., Raedler, T., Sommer, M., Sach, M., Weiller, C., & Koch, M. A. (2004, Sep). White matter asymmetry in the human brain: a diffusion tensor MRI study. *Cereb Cortex*, 14, 945–951.

Bürgel, U., Schormann, T., Schleicher, A., & Zilles, K. (1999, Nov). Mapping of histologically identified long fiber tracts in human cerebral hemispheres to the MRI volume of a reference brain: position and spatial variability of the optic radiation. *Neuroimage*, 10, 489–499.

Carr, H. Y. (1958, Dec). Steady-state free precession in nuclear magnetic resonance. *Phys. Rev.*, 5, 1693–1701.

Carr, H. Y. & Purcell, E. M. (1954, May). Effects of diffusion on free precession in nuclear magnetic resonance experiments. *Phys. Rev.*, 94, 630–638.

Catani, M., Allin, M. P. G., Husain, M., Pugliese, L., Mesulam, M. M., Murray, R. M., & Jones, D. K. (2007, Oct). Symmetries in human brain language pathways correlate with verbal recall. *Proc Natl Acad Sci U S A*, 104, 17163–17168.

Catani, M., Howard, R. J., Pajevic, S., & Jones, D. K. (2002, Sep). Virtual in vivo interactive dissection of white matter fasciculi in the human brain. *Neuroimage*, 17, 77–94.

Catani, M. & Mesulam, M. (2008, Sep). The arcuate fasciculus and the disconnection theme in language and aphasia: history and current state. *Cortex*, 44, 953–961.

Catani, M. & Thiebaut de Schotten, M. (2008). A diffusion tensor imaging tractography atlas for virtual in vivo dissections. *Cortex*, 44, 1105 – 1132. Special Issue on Brain Hodology-Revisiting disconnection approaches to disorders of cognitive function.

Catani, M. & Thiebaut de Schotten, M. (2012). *Atlas of Human Brain Connections*. Oxford University Press.

Cattell, R. (1973). *Personality and mood by questionnaire*. San Francisco: Jossey-Bass.

Cattell, R. B. (1963). Theory of fluid and crystallized intelligence: A critical experiment. *Journal of Educational Psychology*, 54, 1 – 22.

Ceckler, T., Maneval, J., & Melkowits, B. (2001, Jul). Modeling magnetization transfer using a three-pool model and physically meaningful constraints on the fitting parameters. *J Magn Reson*, 151, 9–27.

Ceckler, T. L., Karino, K., Kador, P. F., & Balaban, R. S. (1991, Nov). Magnetic resonance imaging of the rabbit eye. Improved anatomical detail using magnetization transfer contrast. *Invest Ophthalmol Vis Sci*, 32, 3109–3113.

Cercignani, M. (2010). *Diffusion MRI: theory, methods and applications*, Chapter Strategies for Patient-Control Comparison of Diffuison MR Data, pp. 485. New York: Oxford University Press.

Cercignani, M. & Alexander, D. C. (2006, Oct). Optimal acquisition schemes for in vivo quantitative magnetization transfer mri. *Magn Reson Med*, 56, 803–810.

Cercignani, M. & Barker, G. J. (2008, Apr). A comparison between equations describing in vivo MT: the effects of noise and sequence parameters. *J Magn Reson*, 191, 171–183.

Cercignani, M., Basile, B., Span, B., Comanducci, G., Fasano, F., Caltagirone, C., Nocentini, U., & Bozzali, M. (2009). Investigation of quantitative magnetisation transfer parameters of lesions and normal appearing white matter in multiple sclerosis. *NMR in Biomedicine*, 22, 646–653.

Cercignani, M., Symms, M. R., Schmierer, K., Boulby, P. A., Tozer, D. J., Ron, M., Tofts, P. S., & Barker, G. J. (2005, Aug). Three-dimensional quantitative magnetisation transfer imaging of the human brain. *Neuroimage*, 27, 436–441.

Chenevert, T. L. & Pipe, J. G. (1991, Jun). Effect of bulk tissue motion on quantitative perfusion and diffusion magnetic resonance imaging. *Magn Reson Med*, 19, 261–265. ivim.

Chiang, M.-C., Barysheva, M., Shattuck, D. W., Lee, A. D., Madsen, S. K., Avedissian, C., Klunder, A. D., Toga, A. W., McMahon, K. L., de Zubicaray, G. I., Wright, M. J., Srivastava, A., Balov, N., & Thompson, P. M. (2009, Feb). Genetics of brain fiber architecture and intellectual performance. *J Neurosci*, 29, 2212–2224.

Chiang, M.-C., McMahon, K. L., de Zubicaray, G. I., Martin, N. G., Hickie, I., Toga, A. W., Wright, M. J., & Thompson, P. M. (2011, Feb). Genetics of white

matter development: a DTI study of 705 twins and their siblings aged 12 to 29. *Neuroimage*, 54, 2308–2317.

Christensen, K. A., Grant, D. M., Schulman, E. M., & Walling, C. (1974). Optimal determination of relaxation times of fourier transform nuclear magnetic resonance. determination of spin-lattice relaxation times in chemically polarized species. *The Journal of Physical Chemistry*, 78, 1971–1977.

Clayden, J. D., Jentschke, S., noz, M. M., Cooper, J. M., Chadwick, M. J., Banks, T., Clark, C. A., & Vargha-Khadem, F. (2012, Aug). Normative development of white matter tracts: similarities and differences in relation to age, gender, and intelligence. *Cereb Cortex*, 22, 1738–1747.

Cohen, K. (1988). *Statistical Power Analysis for the Behavioural Sciences* (2 ed.). Hillsdale, N.J.: Lawrence Erlbaum Associates.

Colom, R., Jung, R. E., & Haier, R. J. (2006, Jul). Distributed brain sites for the g-factor of intelligence. *Neuroimage*, 31, 1359–1365.

Concha, L., Gross, D. W., & Beaulieu, C. (2005, Oct). Diffusion tensor tractography of the limbic system. *AJNR Am J Neuroradiol*, 26, 2267–2274.

Conturo, T. E., Lori, N. F., Cull, T. S., Akbudak, E., Snyder, A. Z., Shimony, J. S., McKinstry, R. C., Burton, H., & Raichle, M. E. (1999, Aug). Tracking neuronal fiber pathways in the living human brain. *Proc Natl Acad Sci U S A*, 96, 10422–10427.

Corballis, M. C. (1997, Mar). Mental rotation and the right hemisphere. *Brain Lang*, 57, 100–121.

Crooijmans, H. J. A., Gloor, M., Bieri, O., & Scheffler, K. (2011). Influence of MT effects on T2 quantification with 3D balanced steady-state free precession imaging. *Magn. Reson. Med.*, 65, 195–201.

Cunningham, C. H., Pauly, J. M., & Nayak, K. S. (2006, Jun). Saturated double-angle method for rapid B1+ mapping. *Magn Reson Med*, 55, 1326–1333.

Damadian, R. (1971, Mar). Tumor detection by nuclear magnetic resonance. *Science*, 171, 1151–1153.

Davatzikos, C. (2004, Sep). Why voxel-based morphometric analysis should be used with great caution when characterizing group differences. *Neuroimage*, 23, 17–20.

Davies, G. R., Altmann, D. R., Hadjiprocopis, A., Rashid, W., Chard, D. T., Griffin, C. M., Tofts, P. S., Barker, G. J., Kapoor, R., Thompson, A. J., & Miller, D. H. (2005, Sep). Increasing normal-appearing grey and white matter magnetisation transfer ratio abnormality in early relapsing-remitting multiple sclerosis. *J Neurol*, 252, 1037–1044.

Davies, G. R., Tozer, D. J., Cercignani, M., Ramani, A., Dalton, C. M., Thompson, A. J., Barker, G. J., Tofts, P. S., & Miller, D. H. (2004, Dec). Estimation of the macromolecular proton fraction and bound pool T2 in multiple sclerosis. *Mult Scler*, 10, 607–613.

Dejerine, J. (1895). *Anatomie des Centres Nerveux*. Rueff et Cie.

Dell'Acqua, F., Rizzo, G., Scifo, P., Clarke, R. A., Scotti, G., & Fazio, F. (2007, Mar). A model-based deconvolution approach to solve fiber crossing in diffusion-weighted MR imaging. *IEEE Trans Biomed Eng*, 54, 462–472.

Dell'acqua, F., Scifo, P., Rizzo, G., Catani, M., Simmons, A., Scotti, G., & Fazio, F. (2010, Jan). A modified damped Richardson-Lucy algorithm to reduce isotropic background effects in spherical deconvolution. *Neuroimage*, 49, 1446–1458.

Deloire-Grassin, M. S., Brochet, B., Quesson, B., Delalande, C., Dousset, V., Canioni, P., & Petry, K. G. (2000, Sep). In vivo evaluation of remyelination in rat brain by magnetization transfer imaging. *J Neurol Sci*, 178, 10–16.

Deoni, S. C. L. (2007, Oct). High-resolution T1 mapping of the brain at 3T with driven equilibrium single pulse observation of T1 with high-speed incorporation of RF field inhomogeneities (DESPOT1-HIFI). *J Magn Reson Imaging*, 26, 1106–1111.

Deoni, S. C. L. (2009, Aug). Transverse relaxation time (T2) mapping in the brain with off-resonance correction using phase-cycled steady-state free precession imaging. *J Magn Reson Imaging*, 30, 411–417.

Deoni, S. C. L., Peters, T. M., & Rutt, B. K. (2004, Jan). Determination of optimal angles for variable nutation proton magnetic spin-lattice, T1, and spin-spin, T2, relaxation times measurement. *Magn Reson Med*, 51, 194–199.

Deoni, S. C. L., Peters, T. M., & Rutt, B. K. (2005, Jan). High-resolution T1 and T2 mapping of the brain in a clinically acceptable time with DESPOT1 and DESPOT2. *Magn Reson Med*, 53, 237–241.

Deoni, S. C. L., Rutt, B. K., Arun, T., Pierpaoli, C., & Jones, D. K. (2008, Dec). Gleaning multicomponent T1 and T2 information from steady-state imaging data. *Magn Reson Med*, 60, 1372–1387.

Deoni, S. C. L., Rutt, B. K., & Jones, D. K. (2007, Mar). Investigating the effect of exchange and multicomponent T(1) relaxation on the short repetition time spoiled steady-state signal and the DESPOT1 T(1) quantification method. *J Magn Reson Imaging*, 25, 570–578.

Deoni, S. C. L., Rutt, B. K., & Jones, D. K. (2008, Jun). Investigating exchange and multicomponent relaxation in fully-balanced steady-state free precession imaging. *J Magn Reson Imaging*, 27, 1421–1429.

Deoni, S. C. L., Rutt, B. K., & Peters, T. M. (2003, Mar). Rapid combined T1 and T2 mapping using gradient recalled acquisition in the steady state. *Magn Reson Med*, 49, 515–526.

Deoni, S. C. L., Rutt, B. K., & Peters, T. M. (2006, Nov). Synthetic T1-weighted brain image generation with incorporated coil intensity correction using DESPOT1. *Magn Reson Imaging*, 24, 1241–1248.

Deoni, S. C. L., Ward, H. A., Peters, T. M., & Rutt, B. K. (2004, Aug). Rapid T2 estimation with phase-cycled variable nutation steady-state free precession. *Magn Reson Med*, 52, 435–439.

Deutsch, G. K., Dougherty, R. F., Bammer, R., Siok, W. T., Gabrieli, J. D. E., & Wandell, B. (2005, Jun). Children's reading performance is correlated with white matter structure measured by diffusion tensor imaging. *Cortex*, 41, 354–363.

Does, M. D., Beaulieu, C., Allen, P. S., & Snyder, R. E. (1998, Nov). Multi-component T1 relaxation and magnetisation transfer in peripheral nerve. *Magn Reson Imaging*, 16, 1033–1041.

Doricchi, F., Thiebaut de Schotten, M., Tomaiuolo, F., & Bartolomeo, P. (2008, Sep). White matter (dis)connections and gray matter (dys)functions in visual neglect: gaining insights into the brain networks of spatial awareness. *Cortex*, 44, 983–995.

Douaud, G., Jbabdi, S., Behrens, T. E. J., Menke, R. A., Gass, A., Monsch, A. U., Rao, A., Whitcher, B., Kindlmann, G., Matthews, P. M., & Smith, S. (2011, Apr). DTI measures in crossing-fibre areas: increased diffusion anisotropy reveals early white matter alteration in MCI and mild Alzheimer's disease. *Neuroimage*, 55, 880–890.

Dousset, V., Brochet, B., Vital, A., Gross, C., Benazzouz, A., Boullerne, A., Bidabe, A. M., Gin, A. M., & Caille, J. M. (1995, Feb). Lysolecithin-induced demyelination in primates: preliminary in vivo study with MR and magnetization transfer. *AJNR Am J Neuroradiol*, 16, 225–231.

Dousset, V., Grossman, R. I., Ramer, K. N., Schnall, M. D., Young, L. H., Gonzalez-Scarano, F., Lavi, E., & Cohen, J. A. (1992, Feb). Experimental allergic encephalomyelitis and multiple sclerosis: lesion characterization with magnetization transfer imaging. *Radiology*, 182, 483–491.

Dowell, N. G. & Tofts, P. S. (2007, Sep). Fast, accurate, and precise mapping of the RF field in vivo using the 180 degrees signal null. *Magn Reson Med*, 58, 622–630.

Dronkers, N. F., Plaisant, O., Iba-Zizen, M. T., & Cabanis, E. A. (2007, May). Paul broca's historic cases: high resolution MR imaging of the brains of leborgne and lelong. *Brain*, 130, 1432–1441.

Edden, R. A. & Jones, D. K. (2011, September). Spatial and orientational heterogeneity in the statistical sensitivity of skeleton-based analyses of diffusion tensor mr imaging data. *Journal of Neuroscience Methods*, 201, 213–219.

Einstein, A. (1905). Über einen die erzeugung und verwandlung des lichtes betreffenden heuristischen gesichtspunkt. *Annalen der Physik*, 322, 132–148.

Ellmore, T. M., Beauchamp, M. S., Breier, J. I., Slater, J. D., Kalamangalam, G. P., O'Neill, T. J., Disano, M. A., & Tandon, N. (2010, Feb). Temporal lobe white matter asymmetry and language laterality in epilepsy patients. *Neuroimage*, 49, 2033–2044.

Eluvathingal, T. J., Hasan, K. M., Kramer, L., Fletcher, J. M., & Ewing-Cobbs, L. (2007, Dec). Quantitative diffusion tensor tractography of association and projection fibers in normally developing children and adolescents. *Cereb Cortex*, 17, 2760–2768.

Ennis, D. B. & Kindlmann, G. (2006, Jan). Orthogonal tensor invariants and the analysis of diffusion tensor magnetic resonance images. *Magn Reson Med*, 55, 136–146.

Enzmann, D. R. & Pelc, N. J. (1992, Dec). Brain motion: measurement with phase-contrast MR imaging. *Radiology*, 185, 653–660.

Epelbaum, S., Pinel, P., Gaillard, R., Delmaire, C., Perrin, M., Dupont, S., Dehaene, S., & Cohen, L. (2008, Sep). Pure alexia as a disconnection syndrome: new diffusion imaging evidence for an old concept. *Cortex*, 44, 962–974.

Farrell, J. A. D., Zhang, J., Jones, M. V., Deboy, C. A., Hoffman, P. N., Landman, B. A., Smith, S. A., Reich, D. S., Calabresi, P. A., & van Zijl, P. C. M. (2010, May). q-space and conventional diffusion imaging of axon and myelin damage in the rat spinal cord after axotomy. *Magn Reson Med*, 63, 1323–1335.

Fields, R. D. (2008, Jul). White matter in learning, cognition and psychiatric disorders. *Trends Neurosci*, 31, 361–370.

Flöel, A., de Vries, M. H., Scholz, J., Breitenstein, C., & Johansen-Berg, H. (2009, Oct). White matter integrity in the vicinity of Broca's area predicts grammar learning success. *Neuroimage*, 47, 1974–1981.

Flynn, S. W., Lang, D. J., Mackay, A. L., Goghari, V., Vavasour, I. M., Whittall, K. P., Smith, G. N., Arango, V., Mann, J. J., Dwork, A. J., Falkai, P., & Honer, W. G. (2003, Sep). Abnormalities of myelination in schizophrenia detected in vivo with mri, and post-mortem with analysis of oligodendrocyte proteins. *Mol Psychiatry*, 8, 811–820.

Forsen, S. & Hoffman, R. A. (1963). Study of moderately rapid chemical exchange reactions by means of nuclear magnetic double resonance. *The Journal of Chemical Physics*, 39, 2892–2901.

Fram, E. K., Herfkens, R. J., Johnson, G. A., Glover, G. H., Karis, J. P., Shimakawa, A., Perkins, T. G., & Pelc, N. J. (1987). Rapid calculation of T1 using variable flip angle gradient refocused imaging. *Magn Reson Imaging*, 5, 201–208.

Frank, L. R. (2001, Jun). Anisotropy in high angular resolution diffusion-weighted MRI. *Magn Reson Med*, 45, 935–939.

Friston, K. J. (1995, May). Commentary and opinion: II. Statistical parametric mapping: ontology and current issues. *J Cereb Blood Flow Metab*, 15, 361–370.

Friston, K. J. & Penny, W. (2003, Jul). Posterior probability maps and spms. *Neuroimage*, 19, 1240–1249.

Gareau, P. J., Rutt, B. K., Karlik, S. J., & Mitchell, J. R. (2000, Jun). Magnetization transfer and multicomponent T2 relaxation measurements with histopathologic correlation in an experimental model of MS. *J Magn Reson Imaging*, 11, 586–595.

Gass, A., Barker, G. J., Kidd, D., Thorpe, J. W., MacManus, D., Brennan, A., Tofts, P. S., Thompson, A. J., McDonald, W. I., & Miller, D. H. (1994, Jul). Correlation of magnetization transfer ratio with clinical disability in multiple sclerosis. *Ann Neurol*, 36, 62–67.

Ge, Y., Grossman, R. I., Udupa, J. K., Babb, J. S., Kolson, D. L., & McGowan, J. C. (2001, Mar). Magnetization transfer ratio histogram analysis of gray matter in relapsing-remitting multiple sclerosis. *AJNR Am J Neuroradiol*, 22, 470–475.

Gelman, A. & Weakllem, D. (2009). Of beauty, sex and power: Too little attention has been paid to the statistical challenges in estimating small effects. *American Scientist*, 97, 310–316.

Geschwind, N. & Galaburda, A. M. (1985, May). Cerebral lateralization. Biological mechanisms, associations, and pathology: I. A hypothesis and a program for research. *Arch Neurol*, 42, 428–459.

Geschwind, N. & Levitsky, W. (1968, Jul). Human brain: left-right asymmetries in temporal speech region. *Science*, 161, 186–187.

Gloor, M., Scheffler, K., & Bieri, O. (2008, Sep). Quantitative magnetization transfer imaging using balanced SSFP. *Magn Reson Med*, 60, 691–700.

Gochberg, D. F. & Gore, J. C. (2007, Feb). Quantitative magnetization transfer imaging via selective inversion recovery with short repetition times. *Magn Reson Med*, 57, 437–441.

Gong, G., Jiang, T., Zhu, C., Zang, Y., Wang, F., Xie, S., Xiao, J., & Guo, X. (2005, Feb). Asymmetry analysis of cingulum based on scale-invariant parameterization by diffusion tensor imaging. *Hum Brain Mapp*, 24, 92–98.

Good, C. D., Johnsrude, I., Ashburner, J., Henson, R. N., Friston, K. J., & Frackowiak, R. S. (2001, Sep). Cerebral asymmetry and the effects of sex and handedness on brain structure: a voxel-based morphometric analysis of 465 normal adult human brains. *Neuroimage*, 14, 685–700.

Govindan, R. M., Makki, M. I., Sundaram, S. K., Juhsz, C., & Chugani, H. T. (2008, Jul). Diffusion tensor analysis of temporal and extra-temporal lobe tracts in temporal lobe epilepsy. *Epilepsy Res*, 80, 30–41.

Graham, S. J. & Henkelman, R. M. (1997). Understanding pulsed magnetization transfer. *J Magn Reson Imaging*, 7, 903–912.

Grefkes, C. & Fink, G. R. (2005, Jul). The functional organization of the intraparietal sulcus in humans and monkeys. *J Anat*, 207, 3–17.

Hagmann, P., Cammoun, L., Martuzzi, R., Maeder, P., Clarke, S., Thiran, J.-P., & Meuli, R. (2006, Oct). Hand preference and sex shape the architecture of language networks. *Hum Brain Mapp*, 27, 828–835.

Hahn, E. L. (1950, Nov). Spin echoes. *Phys. Rev.*, 80, 580–594.

Haier, R. J., Jung, R. E., Yeo, R. A., Head, K., & Alkire, M. T. (2004, Sep). Structural brain variation and general intelligence. *Neuroimage*, 23, 425–433.

Harris, A. D., Pereira, R. S., Mitchell, J. R., Hill, M. D., Sevick, R. J., & Frayne, R. (2004, Aug). A comparison of images generated from diffusion-weighted and diffusion-tensor imaging data in hyper-acute stroke. *J Magn Reson Imaging*, 20, 193–200.

Haselgrove, J. C. & Moore, J. R. (1996, Dec). Correction for distortion of echo-planar images used to calculate the apparent diffusion coefficient. *Magn Reson Med*, 36, 960–964.

Henkelman, R. M., Huang, X., Xiang, Q. S., Stanisz, G. J., Swanson, S. D., & Bronskill, M. J. (1993, Jun). Quantitative interpretation of magnetization transfer. *Magn Reson Med*, 29, 759–766.

Henkelman, R. M., Stanisz, G. J., & Graham, S. J. (2001, Apr). Magnetization transfer in mri: a review. *NMR Biomed*, 14, 57–64.

Herrera, J. J., Chacko, T., & Narayana, P. A. (2008, Feb). Histological correlation of diffusion tensor imaging metrics in experimental spinal cord injury. *J Neurosci Res*, 86, 443–447.

Highley, J. R., Walker, M. A., Esiri, M. M., Crow, T. J., & Harrison, P. J. (2002, Nov). Asymmetry of the uncinate fasciculus: a post-mortem study of normal subjects and patients with schizophrenia. *Cereb Cortex*, 12, 1218–1224.

Homer, J. & Beevers, M. S. (1985). Driven-equilibrium single-pulse observation of T1 relaxation. A reevaluation of a rapid new method for determining NMR spin-lattice relaxation times. *Journal of Magnetic Resonance (1969)*, 63, 287 – 297.

Homer, J. & Roberts, J. K. (1987). Conditions for the driven equilibrium single pulse observation of spin-lattice relaxation times. *Journal of Magnetic Resonance (1969)*, 74, 424 – 432.

Homer, J. & Roberts, J. K. (1990). Routine evaluation of M0 ratios and T1 values from driven-equilibrium NMR spectra. *Journal of Magnetic Resonance (1969)*, 89, 265 – 272.

Jahanshad, N., Lee, A. D., Barysheva, M., McMahon, K. L., de Zubicaray, G. I., Martin, N. G., Wright, M. J., Toga, A. W., & Thompson, P. M. (2010). Genetic influences on brain asymmetry: A DTI study of 374 twins and siblings. *NeuroImage*, 52, 455 – 469.

Janke, A., Zhao, H., Cowin, G. J., Galloway, G. J., & Doddrell, D. M. (2004, Jul). Use of spherical harmonic deconvolution methods to compensate for nonlinear gradient effects on MRI images. *Magn Reson Med*, 52, 115–122.

Jenkinson, M. & Smith, S. (2001, Jun). A global optimisation method for robust affine registration of brain images. *Med Image Anal*, 5, 143–156.

Jeurissen, B., Leemans, A., Jones, D. K., Tournier, J.-D., & Sijbers, J. (2011, Mar). Probabilistic fiber tracking using the residual bootstrap with constrained spherical deconvolution. *Hum Brain Mapp*, 32, 461–479.

Jezzard, P. & Balaban, R. S. (1995, Jul). Correction for geometric distortion in echo planar images from B0 field variations. *Magn Reson Med*, 34, 65–73.

Jiang, H., Golay, X., van Zijl, P. C. M., & Mori, S. (2002, Apr). Origin and minimization of residual motion-related artifacts in navigator-corrected segmented diffusion-weighted epi of the human brain. *Magn Reson Med*, 47, 818–822.

Johansen-Berg, H. (2007, Feb). Structural plasticity: rewiring the brain. *Curr Biol*, 17, R141–R144.

Johansen-Berg, H. (2010, Aug). Behavioural relevance of variation in white matter microstructure. *Curr Opin Neurol*, 23, 351–358.

Johansen-Berg, H., Behrens, T. E. J., Robson, M. D., Drobnjak, I., Rushworth, M. F. S., Brady, J. M., Smith, S. M., Higham, D. J., & Matthews, P. M. (2004,

Sep). Changes in connectivity profiles define functionally distinct regions in human medial frontal cortex. *Proc Natl Acad Sci U S A*, 101, 13335–13340.

Johansen-Berg, H., Della-Maggiore, V., Behrens, T. E. J., Smith, S. M., & Paus, T. (2007). Integrity of white matter in the corpus callosum correlates with bimanual co-ordination skills. *Neuroimage*, 36 Suppl 2, T16–T21.

Johansen-Berg, H. & Rushworth, M. F. S. (2009). Using diffusion imaging to study human connectional anatomy. *Annu Rev Neurosci*, 32, 75–94.

Jones, C. K., Xiang, Q.-S., Whittall, K. P., & MacKay, A. L. (2004, Mar). Linear combination of multiecho data: short T2 component selection. *Magn Reson Med*, 51, 495–502.

Jones, D. K. (2003, Jan). Determining and visualizing uncertainty in estimates of fiber orientation from diffusion tensor MRI. *Magn Reson Med*, 49, 7–12.

Jones, D. K. (2008a, Sep). Studying connections in the living human brain with diffusion MRI. *Cortex*, 44, 936–952.

Jones, D. K. (2008b, Sep). Tractography gone wild: probabilistic fibre tracking using the wild bootstrap with diffusion tensor MRI. *IEEE Trans Med Imaging*, 27, 1268–1274.

Jones, D. K. (2010). Challenges and limitations of quantifying brain connectivity in vivo with diffusion mri. *Imaging in Medicine*, 2, 341–355.

Jones, D. K. & Cercignani, M. (2010, Aug). Twenty-five pitfalls in the analysis of diffusion MRI data. *NMR Biomed*, 23, 803–820.

Jones, D. K., Christiansen, K., Chapman, R., & Aggleton, J. (2012), Distinct components of the cingulum bundle revealed by diffusion MRI, In *In International Society for Magnetic Resonance in Medicine*, Volume 20th Scientific Meeting.

Jones, D. K., Horsfield, M. A., & Simmons, A. (1999, Sep). Optimal strategies for measuring diffusion in anisotropic systems by magnetic resonance imaging. *Magn Reson Med*, 42, 515–525.

Jones, D. K. & Leemans, A. (2011). Diffusion tensor imaging. *Methods Mol Biol*, 711, 127–144.

Jones, D. K. & Pierpaoli, C. (2005, May). Confidence mapping in diffusion tensor magnetic resonance imaging tractography using a bootstrap approach. *Magn Reson Med*, 53, 1143–1149.

Jones, D. K., Simmons, A., Williams, S. C., & Horsfield, M. A. (1999, Jul). Non-invasive assessment of axonal fiber connectivity in the human brain via diffusion tensor mri. *Magn Reson Med*, 42, 37–41.

Jones, D. K., Symms, M. R., Cercignani, M., & Howard, R. J. (2005, Jun). The effect of filter size on VBM analyses of DT-MRI data. *Neuroimage*, 26, 546–554.

Jones, D. K., Travis, A. R., Eden, G., Pierpaoli, C., & Basser, P. J. (2005, Jun). PASTA: pointwise assessment of streamline tractography attributes. *Magn Reson Med*, 53, 1462–1467.

Kaden, E., Anwander, A., & Knösche, T. R. (2008, Oct). Variational inference of the fiber orientation density using diffusion MR imaging. *Neuroimage*, 42, 1366–1380.

Kaden, E., Knösche, T. R., & Anwander, A. (2007, Aug). Parametric spherical deconvolution: inferring anatomical connectivity using diffusion MR imaging. *Neuroimage*, 37, 474–488.

Kanaan, R. A., Shergill, S. S., Barker, G. J., Catani, M., Ng, V. W., Howard, R., McGuire, P. K., & Jones, D. K. (2006, Jan). Tract-specific anisotropy measurements in diffusion tensor imaging. *Psychiatry Res*, 146, 73–82.

Kaplan, E., Naeser, M. A., Martin, P. I., Ho, M., Wang, Y., Baker, E., & Pascual-Leone, A. (2010, Aug). Horizontal portion of arcuate fasciculus fibers track to pars opercularis, not pars triangularis, in right and left hemispheres: a DTI study. *Neuroimage*, 52, 436–444.

Kennedy, K. M. & Raz, N. (2009, Feb). Aging white matter and cognition: differential effects of regional variations in diffusion properties on memory, executive functions, and speed. *Neuropsychologia*, 47, 916–927.

Kennedy, S. D. & Zhong, J. (2004, Jul). Diffusion measurements free of motion artifacts using intermolecular dipole-dipole interactions. *Magn Reson Med*, 52, 1–6.

Klawiter, E. C., Schmidt, R. E., Trinkaus, K., Liang, H.-F., Budde, M. D., Naismith, R. T., Song, S.-K., Cross, A. H., & Benzinger, T. L. (2011, Apr). Radial diffusivity predicts demyelination in ex vivo multiple sclerosis spinal cords. *Neuroimage*, 55, 1454–1460.

Klistorner, A., Chaganti, J., Garrick, R., Moffat, K., & Yiannikas, C. (2011, May). Magnetisation transfer ratio in optic neuritis is associated with axonal loss, but not with demyelination. *Neuroimage*, 56, 21–26.

Kolind, S. H. & Deoni, S. C. (2011, Feb). Rapid three-dimensional multicomponent relaxation imaging of the cervical spinal cord. *Magn Reson Med*, 65, 551–556.

Kucharczyk, W., Macdonald, P. M., Stanisz, G. J., & Henkelman, R. M. (1994, Aug). Relaxivity and magnetization transfer of white matter lipids at MR imaging: importance of cerebrosides and pH. *Radiology*, 192, 521–529.

Kwong, K. K., Belliveau, J. W., Chesler, D. A., Goldberg, I. E., Weisskoff, R. M., Poncelet, B. P., Kennedy, D. N., Hoppel, B. E., Cohen, M. S., & Turner, R. (1992, Jun). Dynamic magnetic resonance imaging of human brain activity during primary sensory stimulation. *Proc Natl Acad Sci U S A*, 89, 5675–5679.

Lange, N., Dubray, M. B., Lee, J. E., Froimowitz, M. P., Froehlich, A., Adluru, N., Wright, B., Ravichandran, C., Fletcher, P. T., Bigler, E. D., Alexander, A. L., & Lainhart, J. E. (2010, Dec). Atypical diffusion tensor hemispheric asymmetry in autism. *Autism Res*, 3, 350–358.

Laule, C., Kozlowski, P., Leung, E., Li, D. K. B., Mackay, A. L., & Moore, G. R. W. (2008, May). Myelin water imaging of multiple sclerosis at 7 T: correlations with histopathology. *Neuroimage*, 40, 1575–1580.

Laule, C., Leung, E., Lis, D. K. B., Traboulsee, A. L., Paty, D. W., MacKay, A. L., & Moore, G. R. W. (2006, Dec). Myelin water imaging in multiple sclerosis: quantitative correlations with histopathology. *Mult Scler*, 12, 747–753.

Laule, C., Vavasour, I. M., Moore, G. R. W., Oger, J., Li, D. K. B., Paty, D. W., & MacKay, A. L. (2004, Mar). Water content and myelin water fraction in multiple sclerosis. a T2 relaxation study. *J Neurol*, 251, 284–293.

Lazar, M. & Alexander, A. L. (2003, Oct). An error analysis of white matter tractography methods: synthetic diffusion tensor field simulations. *Neuroimage*, 20, 1140–1153.

Lazar, M. & Alexander, A. L. (2005, Jan). Bootstrap white matter tractography (BOOT-TRAC). *Neuroimage*, 24, 524–532.

Le Bihan, D. & Breton, E. (1985). Imagerie de diffusion in vivo par résonance magnétique nucléaire. *CR de lAcadémie des Sciences*, 301, 1109–1112.

Le Bihan, D., Breton, E., Lallemand, D., Aubin, M. L., Vignaud, J., & Laval-Jeantet, M. (1988, Aug). Separation of diffusion and perfusion in intravoxel incoherent motion mr imaging. *Radiology*, 168, 497–505.

Le Bihan, D., Breton, E., Lallemand, D., Grenier, P., Cabanis, E., & Laval-Jeantet, M. (1986, Nov). MR imaging of intravoxel incoherent motions: application to diffusion and perfusion in neurologic disorders. *Radiology*, 161, 401–407.

Le Bihan, D. & Turner, R. (1991, Jun). Intravoxel incoherent motion imaging using spin echoes. *Magn Reson Med*, 19, 221–227.

Lebel, C. & Beaulieu, C. (2009, Nov). Lateralization of the arcuate fasciculus from childhood to adulthood and its relation to cognitive abilities in children. *Hum Brain Mapp*, 30, 3563–3573.

Lebel, C., Walker, L., Leemans, A., Phillips, L., & Beaulieu, C. (2008, Apr). Microstructural maturation of the human brain from childhood to adulthood. *Neuroimage*, 40, 1044–1055.

Leemans, A., Jeurissen, B., Sijbers, J., & Jones, D. K. (2009), ExploreDTI: A graphical toolbox for processing, analyzing, and visualizing diffusion MR data, In *Proc. ISMRM 17th Annual Meeting, Honolulu*, pp. 3536.

Levesque, I., Sled, J. G., Narayanan, S., Santos, A. C., Brass, S. D., Francis, S. J., Arnold, D. L., & Pike, G. B. (2005, Feb). The role of edema and demyelination in chronic T1 black holes: a quantitative magnetization transfer study. *J Magn Reson Imaging*, 21, 103–110.

Levesque, I. R., Giacomini, P. S., Narayanan, S., Ribeiro, L. T., Sled, J. G., Arnold, D. L., & Pike, G. B. (2010, Mar). Quantitative magnetization transfer and myelin water imaging of the evolution of acute multiple sclerosis lesions. *Magn Reson Med*, 63, 633–640.

Lewis, E. B. & Fox, N. C. (2004, Sep). Correction of differential intensity inhomogeneity in longitudinal MR images. *Neuroimage*, 23, 75–83.

Li, H., Xue, Z., Cui, K., & Wong, S. T. C. (2011, Apr). Diffusion tensor-based fast marching for modeling human brain connectivity network. *Comput Med Imaging Graph*, 35, 167–178.

Liepinsh, E. & Otting, G. (1996, Jan). Proton exchange rates from amino acid side chains–implications for image contrast. *Magn Reson Med*, 35, 30–42.

Lori, N. F., Akbudak, E., Shimony, J. S., Cull, T. S., Snyder, A. Z., Guillory, R. K., & Conturo, T. E. (2002). Diffusion tensor fiber tracking of human brain connectivity: aquisition methods, reliability analysis and biological results. *NMR Biomed*, 15, 494–515.

Lu, L. H., Crosson, B., Nadeau, S. E., Heilman, K. M., Gonzalez-Rothi, L. J., Raymer, A., Gilmore, R. L., Bauer, R. M., & Roper, S. N. (2002). Category-specific naming deficits for objects and actions: semantic attribute and grammatical role hypotheses. *Neuropsychologia*, 40, 1608–1621.

Luce, R. (1986). *Response Times: Their Role in Inferring Elementary Mental Organization*. New York: Oxford Univsersity Press.

MacKay, A., Laule, C., Vavasour, I., Bjarnason, T., Kolind, S., & Mädler, B. (2006, May). Insights into brain microstructure from the T2 distribution. *Magn Reson Imaging*, 24, 515–525.

MacKay, A., Whittall, K., Adler, J., Li, D., Paty, D., & Graeb, D. (1994, Jun). In vivo visualization of myelin water in brain by magnetic resonance. *Magn Reson Med*, 31, 673–677.

Madden, D. J., Whiting, W. L., Huettel, S. A., White, L. E., MacFall, J. R., & Provenzale, J. M. (2004, Mar). Diffusion tensor imaging of adult age differences in cerebral white matter: relation to response time. *Neuroimage*, 21, 1174–1181.

Mädler, B., Drabycz, S. A., Kolind, S. H., Whittall, K. P., & MacKay, A. L. (2008, Sep). Is diffusion anisotropy an accurate monitor of myelination? correlation of multicomponent T2 relaxation and diffusion tensor anisotropy in human brain. *Magn Reson Imaging*, 26, 874–888.

Mädler, B. & MacKay, A. L. (2006), In-vivo 3D multi-component T2-relaxation measurements for quantitative myelin imaging at 3T, In *Proc ISMRM 14th Annual Meeting, Seattle*, pp. 1894.

Mädler, B., Whittall, K. P., & MacKay, A. L. (2002), Correlation of multicomponent T2-relaxation data with diffusion tensor anisotropy measures in human brains, In *Proc ISMRM*, pp. 9.

Mandonnet, E., Nouet, A., Gatignol, P., Capelle, L., & Duffau, H. (2007, Mar). Does the left inferior longitudinal fasciculus play a role in language? a brain stimulation study. *Brain*, 130, 623–629.

Mangin, J.-F., Poupon, C., Cointepas, Y., Rivire, D., Papadopoulos-Orfanos, D., Clark, C. A., Régis, J., & Bihan, D. L. (2002). A framework based on spin glass models for the inference of anatomical connectivity from diffusion-weighted mr data - a technical review. *NMR Biomed*, 15, 481–492.

Masutani, Y., Aoki, S., Abe, O., Hayashi, N., & Otomo, K. (2003, Apr). MR diffusion tensor imaging: recent advance and new techniques for diffusion tensor visualization. *Eur J Radiol*, 46, 53–66. Masutani03.

McDonald, C. R., Ahmadi, M. E., Hagler, D. J., Tecoma, E. S., Iragui, V. J., Gharapetian, L., Dale, A. M., & Halgren, E. (2008, Dec). Diffusion tensor imaging correlates of memory and language impairments in temporal lobe epilepsy. *Neurology*, 71, 1869–1876.

Metzler-Baddeley, C., O'Sullivan, M. J., Bells, S., Pasternak, O., & Jones, D. K. (2012, Jan). How and how not to correct for CSF-contamination in diffusion MRI. *Neuroimage*, 59, 1394–1403.

Moore, G. R., Leung, E., MacKay, A. L., Vavasour, I. M., Whittall, K. P., Cover, K. S., Li, D. K., Hashimoto, S. A., Oger, J., Sprinkle, T. J., & Paty, D. W. (2000, Nov). A pathology-MRI study of the short-T2 component in formalin-fixed multiple sclerosis brain. *Neurology*, 55, 1506–1510.

Mori, S., Crain, B. J., Chacko, V. P., & van Zijl, P. C. (1999, Feb). Three-dimensional tracking of axonal projections in the brain by magnetic resonance imaging. *Ann Neurol*, 45, 265–269.

Mori, S. & van Zijl, P. C. M. (2002). Fiber tracking: principles and strategies - a technical review. *NMR Biomed*, 15, 468–480.

Mori, S. & Zhang, J. (2006, Sep). Principles of diffusion tensor imaging and its applications to basic neuroscience research. *Neuron*, 51, 527–539.

Morrell, G. R. (2008, Oct). A phase-sensitive method of flip angle mapping. *Magn Reson Med*, 60, 889–894.

Morrison, C. & Henkelman, R. M. (1995, Apr). A model for magnetization transfer in tissues. *Magn Reson Med*, 33, 475–482.

Moseley, M. (2002). Diffusion tensor imaging and aging - a review. *NMR Biomed*, 15, 553–560.

Moseley, M. E., Cohen, Y., Kucharczyk, J., Mintorovitch, J., Asgari, H. S., Wendland, M. F., Tsuruda, J., & Norman, D. (1990, Aug). Diffusion-weighted MR imaging of anisotropic water diffusion in cat central nervous system. *Radiology*, 176, 439–445.

Moseley, M. E., Cohen, Y., Mintorovitch, J., Chileuitt, L., Shimizu, H., Kucharczyk, J., Wendland, M. F., & Weinstein, P. R. (1990, May). Early detection of regional cerebral ischemia in cats: comparison of diffusion- and T2-weighted MRI and spectroscopy. *Magn Reson Med*, 14, 330–346.

Mottershead, J. P., Schmierer, K., Clemence, M., Thornton, J. S., Scaravilli, F., Barker, G. J., Tofts, P. S., Newcombe, J., Cuzner, M. L., Ordidge, R. J., McDonald, W. I., & Miller, D. H. (2003, Nov). High field MRI correlates of myelin content and axonal density in multiple sclerosis–a post-mortem study of the spinal cord. *J Neurol*, 250, 1293–1301.

Murphy, K. & Garavan, H. (2004, Jun). An empirical investigation into the number of subjects required for an event-related fmri study. *Neuroimage*, 22, 879–885.

Nagarajan, N. & Stevens, C. F. (2008, Sep). How does the speed of thought compare for brains and digital computers? *Curr Biol*, 18, R756–R758.

Nichols, T. E. & Holmes, A. P. (2002, Jan). Nonparametric permutation tests for functional neuroimaging: a primer with examples. *Hum Brain Mapp*, 15, 1–25.

Nucifora, P. G. P., Verma, R., Melhem, E. R., Gur, R. E., & Gur, R. C. (2005, May). Leftward asymmetry in relative fiber density of the arcuate fasciculus. *Neuroreport*, 16, 791–794.

Nunes, R. G., Jezzard, P., & Clare, S. (2005, Nov). Investigations on the efficiency of cardiac-gated methods for the acquisition of diffusion-weighted images. *J Magn Reson*, 177, 102–110.

Odrobina, E. E., Lam, T. Y. J., Pun, T., Midha, R., & Stanisz, G. J. (2005, Aug). MR properties of excised neural tissue following experimentally induced demyelination. *NMR Biomed*, 18, 277–284.

Ogawa, S., Tank, D. W., Menon, R., Ellermann, J. M., Kim, S. G., Merkle, H., & Ugurbil, K. (1992, Jul). Intrinsic signal changes accompanying sensory stimulation: functional brain mapping with magnetic resonance imaging. *Proc Natl Acad Sci U S A*, 89, 5951–5955.

O'Gorman, R. L. & Jones, D. K. (2006, Oct). Just how much data need to be collected for reliable bootstrap DT-MRI? *Magn Reson Med*, 56, 884–890.

Oh, J., Han, E. T., Pelletier, D., & Nelson, S. J. (2006, Jan). Measurement of in vivo multi-component T2 relaxation times for brain tissue using multi-slice T2 prep at 1.5 and 3 T. *Magn Reson Imaging*, 24, 33–43.

Oouchi, H., Yamada, K., Sakai, K., Kizu, O., Kubota, T., Ito, H., & Nishimura, T. (2007). Diffusion anisotropy measurement of brain white matter is affected

by voxel size: underestimation occurs in areas with crossing fibers. *AJNR Am J Neuroradiol*, 28, 1102–1106.

Pajevic, S. & Basser, P. J. (2003, Mar). Parametric and non-parametric statistical analysis of DT-MRI data. *J Magn Reson*, 161, 1–14.

Pajevic, S. & Pierpaoli, C. (1999, Sep). Color schemes to represent the orientation of anisotropic tissues from diffusion tensor data: application to white matter fiber tract mapping in the human brain. *Magn Reson Med*, 42, 526–540.

Papadakis, N. G., Martin, K. M., Mustafa, M. H., Wilkinson, I. D., Griffiths, P. D., Huang, C. L.-H., & Woodruff, P. W. R. (2002, Aug). Study of the effect of CSF suppression on white matter diffusion anisotropy mapping of healthy human brain. *Magn Reson Med*, 48, 394–398.

Papadakis, N. G., Xing, D., Huang, C. L., Hall, L. D., & Carpenter, T. A. (1999, Mar). A comparative study of acquisition schemes for diffusion tensor imaging using MRI. *J Magn Reson*, 137, 67–82.

Park, H.-J., Westin, C.-F., Kubicki, M., Maier, S. E., Niznikiewicz, M., Baer, A., Frumin, M., Kikinis, R., Jolesz, F. A., McCarley, R. W., & Shenton, M. E. (2004, Sep). White matter hemisphere asymmetries in healthy subjects and in schizophrenia: a diffusion tensor MRI study. *Neuroimage*, 23, 213–223.

Parker, G. J. M., Haroon, H. A., & Wheeler-Kingshott, C. A. M. (2003, Aug). A framework for a streamline-based probabilistic index of connectivity (PICo) using a structural interpretation of MRI diffusion measurements. *J Magn Reson Imaging*, 18, 242–254.

Pasternak, O., Sochen, N., Gur, Y., Intrator, N., & Assaf, Y. (2009, Sep). Free water elimination and mapping from diffusion MRI. *Magn Reson Med*, 62, 717–730.

Paus, T., Zijdenbos, A., Worsley, K., Collins, D. L., Blumenthal, J., Giedd, J. N., Rapoport, J. L., & Evans, A. C. (1999, Mar). Structural maturation of neural pathways in children and adolescents: in vivo study. *Science*, 283, 1908–1911.

Peled, S., Cory, D. G., Raymond, S. A., Kirschner, D. A., & Jolesz, F. A. (1999, Nov). Water diffusion, T(2), and compartmentation in frog sciatic nerve. *Magn Reson Med*, 42, 911–918.

Peters, M., Laeng, B., Latham, K., Jackson, M., Zaiyouna, R., & Richardson, C. (1995, Jun). A redrawn Vandenberg and Kuse mental rotations test: different versions and factors that affect performance. *Brain Cogn*, 28, 39–58.

Pfefferbaum, A. & Sullivan, E. V. (2003, May). Increased brain white matter diffusivity in normal adult aging: relationship to anisotropy and partial voluming. *Magn Reson Med*, 49, 953–961.

Pierpaoli, C. & Basser, P. J. (1996, Dec). Toward a quantitative assessment of diffusion anisotropy. *Magn Reson Med*, 36, 893–906.

Pierpaoli, C., Jezzard, P., Basser, P. J., Barnett, A., & Chiro, G. D. (1996, Dec). Diffusion tensor mr imaging of the human brain. *Radiology*, 201, 637–648.

Pierpaoli, C. & Jones, D. (2004), Removing CSF contamination in brain DT-MRIs by using a two-compartment tensor models, In *Proc ISMRM 12th Annual Meeting ISMRM, Kyoto*, pp. 1215.

Pike, G. B., Stefano, N. D., Narayanan, S., Worsley, K. J., Pelletier, D., Francis, G. S., Antel, J. P., & Arnold, D. L. (2000, Jun). Multiple sclerosis: magnetization transfer MR imaging of white matter before lesion appearance on T2-weighted images. *Radiology*, 215, 824–830.

Pitkänen, A., Laakso, M., Kälviäinen, R., Partanen, K., Vainio, P., Lehtovirta, M., Riekkinen, P., & Soininen, H. (1996, Jun). Severity of hippocampal atrophy

correlates with the prolongation of MRI T2 relaxation time in temporal lobe epilepsy but not in Alzheimer's disease. *Neurology*, 46, 1724–1730.

Poncelet, B. P., Wedeen, V. J., Weisskoff, R. M., & Cohen, M. S. (1992, Dec). Brain parenchyma motion: measurement with cine echo-planar MR imaging. *Radiology*, 185, 645–651.

Poon, C. S. & Henkelman, R. M. (1992). Practical T2 quantitation for clinical applications. *J Magn Reson Imaging*, 2, 541–553.

Portnoy, S. & Stanisz, G. J. (2007, Jul). Modeling pulsed magnetization transfer. *Magn Reson Med*, 58, 144–155.

Poupon, C., Clark, C. A., Frouin, V., Régis, J., Bloch, I., Bihan, D. L., & Mangin, J. (2000, Aug). Regularization of diffusion-based direction maps for the tracking of brain white matter fascicles. *Neuroimage*, 12, 184–195.

Powell, H. W. R., Parker, G. J. M., Alexander, D. C., Symms, M. R., Boulby, P. A., Wheeler-Kingshott, C. A. M., Barker, G. J., Noppeney, U., Koepp, M. J., & Duncan, J. S. (2006, Aug). Hemispheric asymmetries in language-related pathways: a combined functional MRI and tractography study. *Neuroimage*, 32, 388–399.

Provenzale, J. M. & Sorensen, A. G. (1999, Dec). Diffusion-weighted MR imaging in acute stroke: theoretic considerations and clinical applications. *AJR Am J Roentgenol*, 173, 1459–1467.

Pruessmann, K. P., Weiger, M., Scheidegger, M. B., & Boesiger, P. (1999, Nov). SENSE: sensitivity encoding for fast MRI. *Magn Reson Med*, 42, 952–962.

Putnam, M. C., Steven, M. S., Doron, K. W., Riggall, A. C., & Gazzaniga, M. S. (2010, Aug). Cortical projection topography of the human splenium: hemispheric asymmetry and individual differences. *J Cogn Neurosci*, 22, 1662–1669.

Ramani, A., Dalton, C., Miller, D. H., Tofts, P. S., & Barker, G. J. (2002, Dec). Precise estimate of fundamental in-vivo MT parameters in human brain in clinically feasible times. *Magn Reson Imaging*, 20, 721–731.

Reese, T. G., Heid, O., Weisskoff, R. M., & Wedeen, V. J. (2003, Jan). Reduction of eddy-current-induced distortion in diffusion MRI using a twice-refocused spin echo. *Magn Reson Med*, 49, 177–182.

Rodrigo, S., Naggara, O., Oppenheim, C., Golestani, N., Poupon, C., Cointepas, Y., Mangin, J. F., Bihan, D. L., & Meder, J. F. (2007, Sep). Human subinsular asymmetry studied by diffusion tensor imaging and fiber tracking. *AJNR Am J Neuroradiol*, 28, 1526–1531.

Romanski, L. M., Tian, B., Fritz, J., Mishkin, M., Goldman-Rakic, P. S., & Rauschecker, J. P. (1999, Dec). Dual streams of auditory afferents target multiple domains in the primate prefrontal cortex. *Nat Neurosci*, 2, 1131–1136.

Ropele, S., Filippi, M., Valsasina, P., Korteweg, T., Barkhof, F., Tofts, P. S., Samson, R., Miller, D. H., & Fazekas, F. (2005, Jan). Assessment and correction of B1-induced errors in magnetization transfer ratio measurements. *Magn Reson Med*, 53, 134–140.

Rosenfeld, A. & Kak, A. (1982). *Digital Picture Processing*. New York: Academic Press.

Rueckert, D., Sonoda, L. I., Hayes, C., Hill, D. L., Leach, M. O., & Hawkes, D. J. (1999, Aug). Nonrigid registration using free-form deformations: application to breast MR images. *IEEE Trans Med Imaging*, 18, 712–721.

Sacolick, L. I., Wiesinger, F., Hancu, I., & Vogel, M. W. (2010). B1 mapping by Bloch-Siegert shifts. *Magn. Reson. Med.*, 63, 1315–1322.

Samson, R. S., Wheeler-Kingshott, C. A. M., Symms, M. R., Tozer, D. J., & Tofts, P. S. (2006, Apr). A simple correction for B1 field errors in magnetization transfer ratio measurements. *Magn Reson Imaging*, 24, 255–263.

Schmierer, K., Scaravilli, F., Altmann, D. R., Barker, G. J., & Miller, D. H. (2004, Sep). Magnetization transfer ratio and myelin in postmortem multiple sclerosis brain. *Ann Neurol*, 56, 407–415.

Schmierer, K., Tozer, D. J., Scaravilli, F., Altmann, D. R., Barker, G. J., Tofts, P. S., & Miller, D. H. (2007, Jul). Quantitative magnetization transfer imaging in postmortem multiple sclerosis brain. *J Magn Reson Imaging*, 26, 41–51.

Schmierer, K., Wheeler-Kingshott, C. A. M., Tozer, D. J., Boulby, P. A., Parkes, H. G., Yousry, T. A., Scaravilli, F., Barker, G. J., Tofts, P. S., & Miller, D. H. (2008, Feb). Quantitative magnetic resonance of postmortem multiple sclerosis brain before and after fixation. *Magn Reson Med*, 59, 268–277.

Schmithorst, V. J., Wilke, M., Dardzinski, B. J., & Holland, S. K. (2002, Jan). Correlation of white matter diffusivity and anisotropy with age during childhood and adolescence: a cross-sectional diffusion-tensor MR imaging study. *Radiology*, 222, 212–218.

Schmithorst, V. J., Wilke, M., Dardzinski, B. J., & Holland, S. K. (2005, Oct). Cognitive functions correlate with white matter architecture in a normal pediatric population: a diffusion tensor MRI study. *Hum Brain Mapp*, 26, 139–147.

Scholz, J., Klein, M. C., Behrens, T. E. J., & Johansen-Berg, H. (2009, Nov). Training induces changes in white-matter architecture. *Nat Neurosci*, 12, 1370–1371.

Schonberg, T., Pianka, P., Hendler, T., Pasternak, O., & Assaf, Y. (2006, May). Characterization of displaced white matter by brain tumors using combined DTI and fMRI. *Neuroimage*, 30, 1100–1111.

Schulte, T., Sullivan, E. V., Müller-Oehring, E. M., Adalsteinsson, E., & Pfefferbaum, A. (2005, Sep). Corpus callosal microstructural integrity influences interhemispheric processing: a diffusion tensor imaging study. *Cereb Cortex*, 15, 1384–1392.

Shimony, J. S., Snyder, A. Z., Conturo, T. E., & Corbetta, M. (2004, Feb). The study of neural connectivity using diffusion tensor tracking. *Cortex*, 40, 213–215.

Siger-Zajdel, M. & Selmaj, K. (2001, Dec). Magnetisation transfer ratio analysis of normal appearing white matter in patients with familial and sporadic multiple sclerosis. *J Neurol Neurosurg Psychiatry*, 71, 752–756.

Sinclair, C. D. J., Samson, R. S., Thomas, D. L., Weiskopf, N., Lutti, A., Thornton, J. S., & Golay, X. (2010). Quantitative magnetization transfer in in vivo healthy human skeletal muscle at 3 T. *Magn. Reson. Med.*, 64, 1739–1748.

Skare, S. & Andersson, J. L. (2001, Oct). On the effects of gating in diffusion imaging of the brain using single shot EPI. *Magn Reson Imaging*, 19, 1125–1128.

Skare, S., Hedehus, M., Moseley, M. E., & Li, T. Q. (2000, Dec). Condition number as a measure of noise performance of diffusion tensor data acquisition schemes with MRI. *J Magn Reson*, 147, 340–352. Skare00.

Sled, J. G., Levesque, I., Santos, A. C., Francis, S. J., Narayanan, S., Brass, S. D., Arnold, D. L., & Pike, G. B. (2004, Feb). Regional variations in normal brain shown by quantitative magnetization transfer imaging. *Magn Reson Med*, 51, 299–303.

Sled, J. G. & Pike, G. B. (2000a, Apr). Correction for B(1) and B(0) variations in quantitative T(2) measurements using MRI. *Magn Reson Med*, 43, 589–593.

Sled, J. G. & Pike, G. B. (2000b, Jul). Quantitative interpretation of magnetization transfer in spoiled gradient echo MRI sequences. *J Magn Reson*, 145, 24–36.

Sled, J. G. & Pike, G. B. (2001, Nov). Quantitative imaging of magnetization transfer exchange and relaxation properties in vivo using MRI. *Magn Reson Med*, 46, 923–931.

Smith, S. M., Jenkinson, M., Johansen-Berg, H., Rueckert, D., Nichols, T. E., Mackay, C. E., Watkins, K. E., Ciccarelli, O., Cader, M. Z., Matthews, P. M., & Behrens, T. E. J. (2006, Jul). Tract-based spatial statistics: voxelwise analysis of multi-subject diffusion data. *Neuroimage*, 31, 1487–1505.

Smith, S. M., Johansen-Berg, H., Jenkinson, M., Rueckert, D., Nichols, T. E., Miller, K. L., Robson, M. D., Jones, D. K., Klein, J. C., Bartsch, A. J., & Behrens, T. E. J. (2007). Acquisition and voxelwise analysis of multi-subject diffusion data with tract-based spatial statistics. *Nat Protoc*, 2, 499–503.

Smith, S. M. & Nichols, T. E. (2009, Jan). Threshold-free cluster enhancement: addressing problems of smoothing, threshold dependence and localisation in cluster inference. *Neuroimage*, 44, 83–98.

Song, S.-K., Sun, S.-W., Ju, W.-K., Lin, S.-J., Cross, A. H., & Neufeld, A. H. (2003, Nov). Diffusion tensor imaging detects and differentiates axon and myelin degeneration in mouse optic nerve after retinal ischemia. *Neuroimage*, 20, 1714–1722.

Song, S.-K., Sun, S.-W., Ramsbottom, M. J., Chang, C., Russell, J., & Cross, A. H. (2002, Nov). Dysmyelination revealed through MRI as increased radial (but unchanged axial) diffusion of water. *Neuroimage*, 17, 1429–1436.

Stanisz, G. J. & Henkelman, R. M. (1998, Sep). Diffusional anisotropy of T2 components in bovine optic nerve. *Magn Reson Med*, 40, 405–410.

Stanisz, G. J., Kecojevic, A., Bronskill, M. J., & Henkelman, R. M. (1999, Dec). Characterizing white matter with magnetization transfer and T(2). *Magn Reson Med*, 42, 1128–1136.

Stanisz, G. J., Webb, S., Munro, C. A., Pun, T., & Midha, R. (2004, Mar). MR properties of excised neural tissue following experimentally induced inflammation. *Magn Reson Med*, 51, 473–479.

Stejskal, E. O. & Tanner, J. E. (1965). Spin diffusion measurements: Spin echoes in the presence of a time-dependent field gradient. *The Journal of Chemical Physics*, 42, 288–292.

Stephan, K. E., Marshall, J. C., Friston, K. J., Rowe, J. B., Ritzl, A., Zilles, K., & Fink, G. R. (2003, Jul). Lateralized cognitive processes and lateralized task control in the human brain. *Science*, 301, 384–386.

Stephan, K. E., Marshall, J. C., Penny, W. D., Friston, K. J., & Fink, G. R. (2007, Mar). Interhemispheric integration of visual processing during task-driven lateralization. *J Neurosci*, 27, 3512–3522.

Stephan, K. E., Tittgemeyer, M., Knsche, T. R., Moran, R. J., & Friston, K. J. (2009, Oct). Tractography-based priors for dynamic causal models. *Neuroimage*, 47, 1628–1638.

Stollberger, R. & Wach, P. (1996, Feb). Imaging of the active B1 field in vivo. *Magn Reson Med*, 35, 246–251.

Takao, H., Abe, O., Yamasue, H., Aoki, S., Kasai, K., & Ohtomo, K. (2010, Jan). Cerebral asymmetry in patients with schizophrenia: a voxel-based morphometry (VBM) and diffusion tensor imaging (DTI) study. *J Magn Reson Imaging*, 31, 221–226.

Tavor, I., Hofstetter, S., Ben-Amitay, S., & Assaf, Y. (2011), Investigation tissue micro-structure changes in short term neuro-plasticity with diffusion MRI, In *Proc ISMRM 19th Annual Meeting, Montréal*.

Thiebaut de Schotten, M., Dell'Acqua, F., Forkel, S. J., Simmons, A., Vergani, F., Murphy, D. G. M., & Catani, M. (2011, Oct). A lateralized brain network for visuospatial attention. *Nat Neurosci*, 14, 1245–1246.

Thiebaut de Schotten, M., Ffytche, D. H., Bizzi, A., Dell'Acqua, F., Allin, M., Walshe, M., Murray, R., Williams, S. C., Murphy, D. G. M., & Catani, M. (2011, Jan). Atlasing location, asymmetry and inter-subject variability of white matter tracts in the human brain with MR diffusion tractography. *Neuroimage*, 54, 49–59.

Thornton, T. L. & Gilden, D. L. (2005, Jun). Provenance of correlations in psychological data. *Psychon Bull Rev*, 12, 409–441.

Toga, A. W. & Thompson, P. M. (2003, Jan). Mapping brain asymmetry. *Nat Rev Neurosci*, 4, 37–48.

Tournier, J.-D., Calamante, F., & Connelly, A. (2007, May). Robust determination of the fibre orientation distribution in diffusion MRI: non-negativity constrained super-resolved spherical deconvolution. *Neuroimage*, 35, 1459–1472.

Tournier, J.-D., Calamante, F., Gadian, D. G., & Connelly, A. (2003, Sep). Diffusion-weighted magnetic resonance imaging fibre tracking using a front evolution algorithm. *Neuroimage*, 20, 276–288.

Tournier, J.-D., Calamante, F., Gadian, D. G., & Connelly, A. (2004, Nov). Direct estimation of the fiber orientation density function from diffusion-weighted MRI data using spherical deconvolution. *Neuroimage*, 23, 1176–1185.

Tournier, J.-D., Calamante, F., King, M. D., Gadian, D. G., & Connelly, A. (2002, Apr). Limitations and requirements of diffusion tensor fiber tracking: an assessment using simulations. *Magn Reson Med*, 47, 701–708.

Tournier, J.-D., Yeh, C.-H., Calamante, F., Cho, K.-H., Connelly, A., & Lin, C.-P. (2008, Aug). Resolving crossing fibres using constrained spherical deconvolution: validation using diffusion-weighted imaging phantom data. *Neuroimage*, 42, 617–625.

Tozer, D. J., Davies, G. R., Altmann, D. R., Miller, D. H., & Tofts, P. S. (2005, Jun). Correlation of apparent myelin measures obtained in multiple sclerosis patients and controls from magnetization transfer and multicompartmental T2 analysis. *Magn Reson Med*, 53, 1415–1422.

Tozer, D. J., Rees, J. H., Benton, C. E., Waldman, A. D., Jger, H. R., & Tofts, P. S. (2011). Quantitative magnetisation transfer imaging in glioma: preliminary results. *NMR in Biomedicine*, 24, 492–498.

Tuch, D. S. (2004, Dec). Q-ball imaging. *Magn Reson Med*, 52, 1358–1372.

Tuch, D. S., Reese, T. G., Wiegell, M. R., Makris, N., Belliveau, J. W., & Wedeen, V. J. (2002, Oct). High angular resolution diffusion imaging reveals intravoxel white matter fiber heterogeneity. *Magn Reson Med*, 48, 577–582.

Tuch, D. S., Reese, T. G., Wiegell, M. R., & Wedeen, V. J. (2003, Dec). Diffusion MRI of complex neural architecture. *Neuron*, 40, 885–895.

Tuch, D. S., Salat, D. H., Wisco, J. J., Zaleta, A. K., Hevelone, N. D., & Rosas, H. D. (2005, Aug). Choice reaction time performance correlates with diffusion anisotropy in white matter pathways supporting visuospatial attention. *Proc Natl Acad Sci U S A*, 102, 12212–12217.

Turner, R., Bihan, D. L., Maier, J., Vavrek, R., Hedges, L. K., & Pekar, J. (1990, Nov). Echo-planar imaging of intravoxel incoherent motion. *Radiology*, 177, 407–414.

Underhill, H. R., Yuan, C., & Yarnykh, V. L. (2009, Oct). Direct quantitative comparison between cross-relaxation imaging and diffusion tensor imaging of the human brain at 3.0 T. *Neuroimage*, 47, 1568–1578.

Vallar, G. & Perani, D. (1986). The anatomy of unilateral neglect after right-hemisphere stroke lesions. a clinical/CT-scan correlation study in man. *Neuropsychologia*, 24, 609–622.

van Waesberghe, J. H. & Barkhof, F. (1999). Magnetization transfer imaging of the spinal cord and the optic nerve in patients with multiple sclerosis. *Neurology*, 53, S46–S48.

van Waesberghe, J. H., Kamphorst, W., Groot, C. J. D., van Walderveen, M. A., Castelijns, J. A., Ravid, R., Nijeholt, G. J. L. a., van der Valk, P., Polman, C. H., Thompson, A. J., & Barkhof, F. (1999, Nov). Axonal loss in multiple sclerosis lesions: magnetic resonance imaging insights into substrates of disability. *Ann Neurol*, 46, 747–754.

Vasanawala, S. S., Pauly, J. M., & Nishimura, D. G. (2000, Jan). Linear combination steady-state free precession MRI. *Magn Reson Med*, 43, 82–90.

Vavasour, I. M., Laule, C., Li, D. K., Traboulsee, A. L., & MacKay, A. L. (2011). Is the magnetization transfer ratio a marker for myelin in multiple sclerosis? *J. Magn. Reson. Imaging*, n/a–n/a.

Vavasour, I. M., Whittall, K. P., MacKay, A. L., Li, D. K., Vorobeychik, G., & Paty, D. W. (1998, Nov). A comparison between magnetization transfer ratios and myelin water percentages in normals and multiple sclerosis patients. *Magn Reson Med*, 40, 763–768.

Vernooij, M. W., Smits, M., Wielopolski, P. A., Houston, G. C., Krestin, G. P., & van der Lugt, A. (2007, Apr). Fiber density asymmetry of the arcuate fasciculus in relation to functional hemispheric language lateralization in both right- and left-handed healthy subjects: a combined fMRI and DTI study. *Neuroimage*, 35, 1064–1076.

Vidarsson, L., Conolly, S. M., Lim, K. O., Gold, G. E., & Pauly, J. M. (2005, Feb). Echo time optimization for linear combination myelin imaging. *Magn Reson Med*, 53, 398–407.

Vogel, J. J., Bowers, C. A., & Vogel, D. S. (2003, Jul). Cerebral lateralization of spatial abilities: a meta-analysis. *Brain Cogn*, 52, 197–204.

Volz, S., Nöth, U., Rotarska-Jagiela, A., & Deichmann, R. (2010, Feb). A fast B1-mapping method for the correction and normalization of magnetization transfer ratio maps at 3 T. *Neuroimage*, 49, 3015–3026.

Vos, S. B., Jones, D. K., Jeurissen, B., Viergever, M. A., & Leemans, A. (2012, Feb). The influence of complex white matter architecture on the mean diffusivity in diffusion tensor MRI of the human brain. *Neuroimage*, 59, 2208–2216.

Vos, S. B., Jones, D. K., Viergever, M. A., & Leemans, A. (2011, Apr). Partial volume effect as a hidden covariate in dti analyses. *Neuroimage*, 55, 1566–1576.

Vul, E., Harris, C., Winkielman, P., & Pashler, H. (2009). Puzzlingly high correlations in fMRI studies of emotion, personality, and social cognition. *Perspectives on Psychological Science*, 4, 274–290.

Wahl, M., Li, Y.-O., Ng, J., Lahue, S. C., Cooper, S. R., Sherr, E. H., & Mukherjee, P. (2010, Jun). Microstructural correlations of white matter tracts in the human brain. *Neuroimage*, 51, 531–541.

Wang, H. Z., Riederer, S. J., & Lee, J. N. (1987, Nov). Optimizing the precision in T1 relaxation estimation using limited flip angles. *Magn Reson Med*, 5, 399–416.

Wang, J., Lin, Y., Wai, Y., Liu, H., Lin, C., & Huang, Y. (2008, Apr). Visualization of the coherence of the principal diffusion orientation: an eigenvector-based approach. *Magn Reson Med*, 59, 764–770.

Wang, J., Qiu, M., Kim, H., & Constable, R. T. (2006, Oct). T1 measurements incorporating flip angle calibration and correction in vivo. *J Magn Reson*, 182, 283–292.

Watkins, K. E., Vargha-Khadem, F., Ashburner, J., Passingham, R. E., Connelly, A., Friston, K. J., Frackowiak, R. S. J., Mishkin, M., & Gadian, D. G. (2002, Mar). MRI analysis of an inherited speech and language disorder: structural brain abnormalities. *Brain*, 125, 465–478.

Weber, O. M., Speier, P., Scheffler, K., & Bieri, O. (2009). Assessment of magnetization transfer effects in myocardial tissue using balanced steady-state free precession (bSSFP) cine MRI. *Magn. Reson. Med.*, 62, 699–705.

Wedeen, V. J., Hagmann, P., Tseng, W.-Y. I., Reese, T. G., & Weisskoff, R. M. (2005, Dec). Mapping complex tissue architecture with diffusion spectrum magnetic resonance imaging. *Magn Reson Med*, 54, 1377–1386.

Westin, C.-F., Maier, S. E., Mamata, H., Nabavi, A., Jolesz, F. A., & Kikinis, R. (2002, Jun). Processing and visualization for diffusion tensor mri. *Med Image Anal*, 6, 93–108.

Wheeler-Kingshott, C. A. M. & Cercignani, M. (2009, May). About "axial" and "radial" diffusivities. *Magn Reson Med*, 61, 1255–1260.

Whittall, K. P. & MacKay, A. L. (1989). Quantitative interpretation of NMR relaxation data. *Journal of Magnetic Resonance (1969)*, 84, 134 – 152.

Whittall, K. P., MacKay, A. L., Graeb, D. A., Nugent, R. A., Li, D. K., & Paty, D. W. (1997, Jan). In vivo measurement of T2 distributions and water contents in normal human brain. *Magn Reson Med*, 37, 34–43.

Whittall, K. P., MacKay, A. L., Li, D. K. B., Vavasour, I. M., Jones, C. K., & Paty, D. W. (2002, Feb). Normal-appearing white matter in multiple sclerosis has heterogeneous, diffusely prolonged t(2). *Magn Reson Med*, 47, 403–408.

Wilke, M. (2012, 04). An iterative jackknife approach for assessing reliability and power of fMRI group analyses. *PLoS ONE*, 7, e35578.

Wimberger, D. M., Roberts, T. P., Barkovich, A. J., Prayer, L. M., Moseley, M. E., & Kucharczyk, J. (1995). Identification of "premyelination" by diffusion-weighted MRI. *J Comput Assist Tomogr*, 19, 28–33.

Wirestam, R., Greitz, D., Thomsen, C., Brockstedt, S., Olsson, M. B., & Stahlberg, F. (1996). Theoretical and experimental evaluation of phase-dispersion effects caused by brain motion in diffusion and perfusion MR imaging. *J Magn Reson Imaging*, 6, 348–355.

Witelson, S. F., Beresh, H., & Kigar, D. L. (2006, Feb). Intelligence and brain size in 100 postmortem brains: sex, lateralization and age factors. *Brain*, 129, 386–398.

Wolbers, T., Schoell, E. D., & Büchel, C. (2006, Sep). The predictive value of white matter organization in posterior parietal cortex for spatial visualization ability. *Neuroimage*, 32, 1450–1455.

Wolff, S. D. & Balaban, R. S. (1989, Apr). Magnetization transfer contrast (MTC) and tissue water proton relaxation in vivo. *Magn Reson Med*, 10, 135–144.

Wolff, S. D., Eng, J., & Balaban, R. S. (1991, Apr). Magnetization transfer contrast: method for improving contrast in gradient-recalled-echo images. *Radiology*, 179, 133–137.

Wu, Y., Alexander, A. L., Fleming, J. O., Duncan, I. D., & Field, A. S. (2006). Myelin water fraction in human cervical spinal cord in vivo. *J Comput Assist Tomogr*, 30, 304–306.

Yarnykh, V. L. (2002, May). Pulsed Z-spectroscopic imaging of cross-relaxation parameters in tissues for human MRI: theory and clinical applications. *Magn Reson Med*, 47, 929–939.

Yarnykh, V. L. (2007, Jan). Actual flip-angle imaging in the pulsed steady state: a method for rapid three-dimensional mapping of the transmitted radiofrequency field. *Magn Reson Med*, 57, 192–200.

Yu, C., Li, J., Liu, Y., Qin, W., Li, Y., Shu, N., Jiang, T., & Li, K. (2008, May). White matter tract integrity and intelligence in patients with mental retardation and healthy adults. *Neuroimage*, 40, 1533–1541.

Zaaraoui, W., Deloire, M., Merle, M., Girard, C., Raffard, G., Biran, M., Inglese, M., Petry, K. G., Gonen, O., Brochet, B., Franconi, J.-M., & Dousset, V. (2008, Sep). Monitoring demyelination and remyelination by magnetization transfer imaging in the mouse brain at 9.4 T. *MAGMA*, 21, 357–362.

Zalesky, A., Cocchi, L., Fornito, A., Murray, M. M., & Bullmore, E. (2012). Connectivity differences in brain networks. *NeuroImage*, 60, 1055 – 1062.

Zhu, T., Liu, X., Connelly, P. R., & Zhong, J. (2008, Apr). An optimized wild bootstrap method for evaluation of measurement uncertainties of DTI-derived parameters in human brain. *Neuroimage*, 40, 1144–1156.